Fast and Efficient Calibration for Phased Arrays and Beamforming Circuits using Novel Constellation Characterization Method and Channel Transformation Technique

by

Yuxuan Chen

A thesis
presented to the University of Waterloo
in fulfillment of the
thesis requirement for the degree of
Master of Applied Science
in
Electrical and Computer Engineering

Waterloo, Ontario, Canada, 2024

© Yuxuan Chen 2024

Author's Declaration

I hereby declare that I am the sole author of this thesis. This is a true copy of the thesis, including any required final revisions, as accepted by my examiners.

I understand that my thesis may be made electronically available to the public.

Abstract

Traditional phased array calibration methods, like exhaustive search, are time-consuming. This thesis proposes a novel, efficient technique that significantly reduces calibration time without sacrificing performance.

The proposed approach utilizes a constellation characterization method. It extracts and describes element responses using a set of mapping functions based on a strategically chosen data subset. A custom solver then generates control codes for desired beam patterns. For robustness, a closed-loop calibration routine is introduced to verify the solutions. Additionally, a taper awareness scheme is incorporated to optimize the output power by accounting for element variations and the desired tapering profile. The proposed method demonstrates significant speed-up compared to the exhaustive search method. On two beamforming integrated circuits (BFICs) and two test arrays, it achieves improvements of up to 1100 times while maintaining performance.

Furthermore, a channel transformation technique is proposed to leverage similarities between array elements. This technique reduces measurements by transferring mapping functions between array elements, avoiding full characterization for each element. A sequencing technique is also introduced to optimize the transformation route, maximizing success rates and further minimizing measurements. Experimental validation shows significant reductions in addition to the savings achieved via the proposed characterization method. Compared to the exhaustive search method, reductions of up to 3000 times are achieved.

This thesis presents significant advancements to phased array calibration, paving the way for efficient and scalable solutions in future high-resolution massive multiple input and multiple output (MIMO) systems.

Acknowledgments

I would like to express my deepest gratitude to Professor Slim Boumaiza for his invaluable guidance throughout this research journey and for providing me with the opportunity to participate in the research activities of the Emerging Radio System Group (EmRG).

My heartfelt thanks go to all my EmRG colleagues for their patience during my extensive presentations and for engaging in stimulating discussions with me, day and night. In particular, I am deeply grateful to Dr. Ahmed Ben Ayed and Mohammad Abdollah Chalaki for their assistance and measurement expertise, which were crucial to the success of this work. I also extend my gratitude to my colleagues on the IC team, especially Mehran Hazer Sahlabadi, for their contribution to the initiation of this project.

Finally, I extend my profound appreciation to my family and my girlfriend for their unwavering support and love throughout my master's program and as I embark on future endeavors.

Table of Contents

Author's Declaration ii

Abstract iii

Acknowledgments iv

List of Figures ix

List of Tables xvi

1 Introduction 1

1.1 Motivation 1

1.2 Problem Statement 4

1.3 Thesis Organization 7

2 Background and Literature Review 8

2.1 Background on Beamforming and Phased Array 8

2.2 Literature Review on Antenna Array Measurement Methods 11

2.2.1 Element-by-Element Direct Measurement Method 11

2.2.2 Mutual Coupling Method 11

2.2.3 Rotating-Element Electric-field Vector (REV) Method 14

2.2.4 Orthogonal Coding Method 16

2.3 Literature Review on Control-Error Compensation Methods 18
2.3.1 Constant Error Compensation Method 18
2.3.2 Exhaustive Search Method 18
2.3.3 Pseudo-Exhaustive Search Method 19
2.3.4 Control Sampling Method 20
2.4 Calibration Performance Matrices 21
2.4.1 Root Mean Square Errors (RMSE) 21
2.4.2 Error Vector Magnitude (EVM) 21

3 Rapid Calibration of BFICs/Phased Arrays using Novel Constellation Characterization Method 23
3.1 Calibration Routine Overview 23
3.1.1 Unsupervised Calibration Routine 25
3.1.2 Supervised Calibration Routine 25
3.2 Fast Constellation Characterization Method 27
3.2.1 Strategy 27
3.2.2 Overview 29
3.2.3 Characterization Dataset Acquisition 32
3.2.4 Mapping Functions Generation 34
3.2.5 Control Code Iterative Solver 43
3.2.6 Optimum Sampling Indexes Selection 48
3.2.7 Optimum Sampling Size 49
3.2.8 Targeting Gain Allocation with Tapering Awareness 50
3.3 Adaptive Kernel Search Algorithm 51
3.3.1 Overview 51
3.3.2 Kernel Definition 53
3.3.3 Validation Criteria 54
3.3.4 Position Compensation 56

3.4 Experimental Validation . . . 59
3.4.1 BFIC1 Calibration . . . 59
3.4.2 BFIC2 Calibration . . . 67
3.4.3 4×4 BFIC1 Array Calibration . . . 74
3.4.4 4×4 BFIC2 Array Calibration . . . 78
3.5 Remarks . . . 82

4 Channel Transformation and Similarity Sequencing Techniques for Intelligent Phased Array Calibration 84
4.1 Overview . . . 86
4.2 Channel Transformation Routine . . . 91
4.3 Channel Transformation Method . . . 93
4.3.1 Transformation Dataset Acquisition . . . 93
4.3.2 Mapping Functions Synthesis . . . 94
4.3.3 Synthesis Sequence Walk-through . . . 107
4.3.4 Transformation Validation . . . 111
4.4 Array Elements Similarity Sequencing . . . 113
4.4.1 Overview . . . 113
4.4.2 Distance Definition . . . 115
4.4.3 Reference Channel Identification . . . 117
4.4.4 Similarity Tree Navigation and Management . . . 119
4.5 Dynamic Outline Sampling . . . 120
4.5.1 Dynamic Sampling Size . . . 121
4.5.2 Outline Data Reconstruction . . . 121
4.6 Experimental Validation . . . 122
4.6.1 4×4 BFIC1 Array Calibration . . . 122
4.6.2 4×4 BFIC2 Array Calibration . . . 127
4.7 Remarks . . . 130

5 Conclusion **132**

References **134**

List of Figures

1.1 Internet users as a share of population, global and by country income group, 1990-2022. Note: HIC = high-income countries; LIC = low-income countries; LMIC = lower-middle-income countries; UMIC = upper-middle-income countries. [1] 2

1.2 Illustration of beamforming by applying more antenna elements and phase shifts. [2] 3

1.3 Radiated power from a 4G direction antenna vs. 5G beam-based antennas. [2] 4

1.4 RF beamforming system illustrating the radiation pattern distortion due to hardware nonidealities. 5

1.5 Raw and calibrated constellation corresponding to the 8-bit phase and 8-bit gain states of the VGPS and the calibrated 6-bit phase and 12 gain states with 1dB gain tuning resolution, respectively. 6

2.1 Demonstration of a linear array with N elements. 9

2.2 Normalized Array factor for a linear array of 12 elements: (a) Beam steering; (b) Gain tapering using different tapering profiles. 9

2.3 Block diagram of different beamforming architectures: (a) Digital beamforming; (b) Analog beamforming; (c) Hybrid beamforming. 10

2.4 Quad-based self-calibrating multi-beam TRX phased-array using antenna mutual coupling. [3] 12

2.5 Exploiting antenna coupling symmetry to calibrate the array rows: (a) pivoting at $b_{1,2}$, (b) pivoting at $b_{1,3}$ and (c) pivoting at an extra passive probe antenna. [3] 13

2.6 REV principle: (a) The array field is the vector sum of the electric fields of individual elements; (b) Sinusoidal array power variation measured. [4] . . 14

2.7 Block diagram of RF beamforming array with embedded NF probes for array calibration and DPD training. [5] 17

3.1 Response definition of VGPS/Array Elements. 24

3.2 Top-level flow diagram of the novel VGPS characterization process. 24

3.3 Flow diagram of the proposed unsupervised calibration routine. 25

3.4 Flow diagram of the proposed supervised calibration routine. 26

3.5 BFIC1 measurement. 27

3.6 Example calibration method demonstrating the regionality of the characterization dataset. Calibrated on the BFIC1 targeting 6-bit phase and 8 gain states: (a) example characterization dataset; (b) corresponding calibration result. 28

3.7 Example gain and phase profiles of the BFIC1 (incomplete set): (a) gain profiles; (b) phase profiles. 29

3.8 Characterization Dataset for BFIC1. Sampled with outline data sampling size of 23 and gain data sampling size of 8. 31

3.9 Flow diagram of the proposed VGPS constellation characterization process. 32

3.10 Characterization Dataset: (a) main and auxiliary outline data; (b) main and auxiliary gain data. 33

3.11 Main and auxiliary gain profile sampled from BFIC1 using a gain data sampling size of 8. Solid dots represent discrete measurement data points. Interpolated for the entire gain index range using the shape-preserving piecewise cubic interpolation method: (a) gain profile, $I_{\theta,main} = 175$; (b) auxiliary gain profile, $I_{\theta,aux} = 71$. 35

3.12 Main and auxiliary phase profile sampled from BFIC1 using an outline data sampling size of 23. Solid dots represent discrete measurement data points. Interpolated for the entire phase index range using the modified Akima piecewise cubic Hermite interpolation method: (a) phase profile, $I_{G,main} = 256$; (b) auxiliary phase profile, $I_{G,aux} = 147$. 36

3.13 Main and auxiliary gain envelope sampled from BFIC1 using an outline data sampling size of 23. Solid dots represent discrete measurement data points. Interpolated for the entire phase index range using the cubic spline interpolation method: (a) gain envelope, $I_{G,main} = 256$; (b) auxiliary gain envelope, $I_{G,aux} = 147$. 37

3.14 Main and auxiliary gain-to-phase variation sampled from BFIC1 using a gain data sampling size of 8. Solid dots represent discrete measurement data points. Interpolated for the entire gain index range using the modified Akima piecewise cubic Hermite interpolation method: (a) gain-to-phase variation, $I_{\theta,main} = 175$; (b) auxiliary gain-to-phase variation, $I_{\theta,aux} = 71$. . 38

3.15 Gain Envelope Scaling Profile sampled from BFIC1 using a gain data sampling size of 8, $I_{G,main} = 256$, $I_{G,aux} = 147$. Solid dots represent discrete measurement data points. Interpolated for the entire gain index range using the cubic spline interpolation method. 39

3.16 Normalized gain profiles sampled from BFIC1 at phase indexes 47 and 175 to demonstrate the shape change. 39

3.17 Gain Profile Scaling Profile sampled from BFIC1 using a gain data sampling size of 8, $I_{\theta,main} = 175$, $I_{\theta,aux} = 71$. Solid dots represent discrete measurement data points. Interpolated for the entire gain index range using the modified Akima piecewise cubic Hermite interpolation method. 40

3.18 General Gain Profile Scaling Profile for different auxiliary phase indexes. Sampled from BFIC1 using a gain data sampling size of 8. Solid dots represent discrete measurement data points. Interpolated for the entire gain index range using the modified Akima piecewise cubic Hermite interpolation method. 41

3.19 Phase Profile Shifting Profile sampled from BFIC1 using an outline data sampling size of 23, $I_{G,main} = 256$, $I_{G,aux} = 147$. Solid dots represent discrete data points. Interpolated for the entire phase index range using the cubic spline interpolation method. 42

3.20 General Phase Profile Shifting Profile for different auxiliary gain indexes. Sampled from BFIC1 using an outline data sampling size of 23. Solid dots are discrete data points. Interpolated for the entire phase index range using the cubic spline method. 43

3.21 Example adjustment of Gain Profile Scaling Profile using an observation at the auxiliary gain index of 147. 45

3.22 Example adjustment of Phase Profile Shifting Profile using an observation at the auxiliary phase index of 71. 46
3.23 Calibration result over the two channels of the BFIC1 with varying characterization sampling size. Targeting 64 phase states, 8 gain states with 1dB gain tunning resolution. (a) FOM; (b) EVM levels. 49
3.24 Demonstration of the setting of targeting gain states for a 4x4 array with Taylor window gain tapering profile: (a) typical; (b) with taper awareness. 51
3.25 Adaptive Kernel Search flow charts: (a) Validation criteria; (b) Position compensation and kernel size expansion. 52
3.26 Kernel demonstration for: (a) Kernel size N=1; (b) Kernel size N=3. . . . 53
3.27 Validation criteria: (a) Distance criterion; (b) Encirclement criterion. . . . 54
3.28 Validation region for a target point. Figure showing half-distance validation region (dotted line) and quarter-distance validation region (dashed line). . 55
3.29 Position Compensation demonstration for a kernel of size 3. 57
3.30 Measurement setup for BFIC1: (a) Setup block diagram; (b) Setup picture. 60
3.31 BFIC1 single-channel full measurement. 61
3.32 Calibrated targeting constellation on BFIC1 using different calibration methods. Targeting 64 phase states, 8 gain states with 1dB gain tuning resolution. Proposed characterization method using outline data sampling size of 23 and gain data sampling size of 8. (a) Exhaustive search; (b) No calibration; (c) Proposed supervised calibration; (d) Proposed unsupervised calibration. . . 63
3.33 Measurement setup for BFIC2: (a) Setup block diagram; (b) Setup picture. 67
3.34 BFIC2 single-channel full measurement. 69
3.35 Calibrated targeting constellation on BFIC2 using different calibration methods. Targeting 64 phase states, 8 gain states with 1dB gain tuning resolution. Proposed characterization method using outline data sampling size of 10 and gain data sampling size of 4. (a) Exhaustive search; (b) No calibration; (c) Proposed supervised calibration; (d) Proposed unsupervised calibration. . . 71
3.36 Measurement setup for 4×4 BFIC1 array: (a) Array close up; (b) Setup picture. 75
3.37 Measured radiation pattern of the 4x4 BFIC1 array: (a) No taper; (b) Gain tapering with taper awareness; (c) Unsupervised calibration comparing taper solutions; (d) Beam steering. 77

3.38 Measurement setup for 4×4 BFIC2 array: (a) Array close up; (b) Setup picture. 79

3.39 Measured radiation pattern of the 4x4 BFIC2 array: (a) No taper; (b) Gain tapering with taper awareness; (c) Unsupervised calibration comparing taper solutions; (d) Beam steering. 81

4.1 Full 16 channels far-field measurements for 4×4 BFIC1 array. Measurement for a specific element is done in the far-field with the other elements turned "OFF". Plots are scaled preserving the received power level and the x-axis and y-axis show the real and imaginary parts of the transmission coefficient, respectively. 85

4.2 Top-level flow chart of the channel transformation process. 86

4.3 Demonstration showing the subset of the characterization dataset used for channel transformation. 87

4.4 Mapping functions synthesis demonstration for the 4×4 BFIC1 array. Demonstrating the synthesis of the four main mapping functions from channel 5 to channel 7. 89

4.5 Mapping functions synthesis demonstration for the 4×4 BFIC1 array. Demonstrating the synthesis of the three composite mapping functions from channel 5 to channel 7. 90

4.6 Adaptive Channel Transformation flow diagram. 92

4.7 Transformation Dataset illustration. 93

4.8 Transformation Dataset Acquisition and Mapping Functions Synthesis flow chart. 95

4.9 Gain profile synthesis illustration: (a) gain profile synthesis; (b) auxiliary gain profile synthesis. 97

4.10 Phase profile synthesis illustration: (a) Phase profile synthesis; (b) Auxiliary phase profile synthesis. 98

4.11 Gain envelope synthesis illustration: (a) Gain envelope synthesis; (b) Auxiliary gain envelope synthesis. 99

4.12 Gain-to-phase variation synthesis illustration: (a) Gain-to-phase variation synthesis; (b) Auxiliary gain-to-phase variation synthesis. 101

4.13 Preliminary GESP synthesis illustration: (a) Detect fundamental gain envelope phase shift; (b) Preliminary GESP synthesis. 103
4.14 Final gain envelope scaling profile synthesis illustration. 104
4.15 Gain profile scaling profile synthesis illustration. 105
4.16 Phase profile shifting profile synthesis illustration: (a) Preliminary PPSP synthesis; (b) Final PPSP synthesis. 106
4.17 Transformation Dataset Acquisition and Mapping Functions Synthesis stages. 107
4.18 Example calibration method demonstrating the regionality of the characterization dataset. (a) Characterization dataset validity; (b) Corresponding calibration result. 111
4.19 Transformation validation test points. 112
4.20 Array Elements Similarity Sequencing flow diagram. 113
4.21 Illustration of the fully-connected graph and the generated minimum-spanning tree: (a) Fully-connected Graph; (b) Generated minimum-spanning tree (MST). 117
4.22 Illustration of the process of finding the reference node. 118
4.23 Illustration of the process of tree navigation and management. 119
4.24 Example of the calculation of the dynamic sampling size. 121
4.25 Measurement setup for 4×4 BFIC1 array: (a) Array close up; (b) Setup picture. 122
4.26 Channel transformation with AESS shortest-path trees for the 4×4 BFIC1 array showing transformation progressions. 124
4.27 Measured radiation pattern of the 4x4 BFIC1 array. The proposed methods are using the unsupervised calibration routine: (a) Electrically-steered radiation pattern with the beam pointed at the board side; (d) Mechanically-steered radiation pattern with the beam pointed at -30 degrees. 126
4.28 Measurement setup for 4×4 BFIC2 array: (a) Array close up; (b) Setup picture. 127
4.29 Channel transformation with AESS shortest-path trees for the 4×4 BFIC2 array showing transformation progressions. 129

4.30 Measured radiation pattern of the 4x4 BFIC2 array. The proposed methods are using the unsupervised calibration routine: (a) Electrically-steered radiation pattern with the beam pointed at the board side; (d) Mechanically-steered radiation pattern with the beam pointed at -30 degrees. 131

List of Tables

3.1 BFIC1 calibration results comparison. Characterized using outline data sampling size of 23 and gain data sampling size of 8. The supervised routine has the validation tolerance coefficient set to 10. 64

3.2 BFIC2 calibration results comparison. Characterized using an outline data sampling size of 10 and a gain data sampling size of 4. The supervised routine has the validation tolerance coefficient set to 2. 72

3.3 4x4 BFIC1 array calibration results comparison. 76

3.4 4x4 BFIC2 array calibration results comparison. 80

4.1 4x4 BFIC1 array calibration results comparison. The proposed methods are using the unsupervised routine with either full characterization or channel transformation. 124

4.2 4x4 BFIC2 array calibration results comparison. The proposed methods are using the unsupervised routine with either full characterization or channel transformation. 128

Chapter 1

Introduction

1.1 Motivation

As the number of internet users and internet demands continue to soar globally, especially in low-income to middle-income countries [1], tremendous research efforts are being made to improve the quality and coverage of service for such a trend to continue. According to the 2023 digital progress and trends report by the world bank group, the world gained 1.5 billion new internet users between 2018 and 2022 (Fig. 1.1), as the COVID-19 pandemic amplified and accelerated growth in low- and middle-income countries [1]. The number of internet users reached 5.3 billion in 2022 (66% of the world population) [1], which is a year earlier than the expected 2023 as projected by Cisco Annual Internet Report in 2020 [6], demonstrating the effect of the unforeseen pandemic. In 2020, the first year of the COVID-19 pandemic, the share of the global population using the internet increased by 6 percent (500 million people), the highest jump in history, as mobility restrictions drove many activities online [1].

Apart from internet users, the number of connected devices is projected to reach 500 billion by 2030 [7] thanks to the huge and growing demand for Internet of Things (IoT) devices and self-driving cars [8]. Leading tech companies like Samsung envision future mobile devices to take on various form factors, such as augmented reality (AR) glasses, virtual reality (VR) headsets, and hologram devices [8]. The wearable nature of many of those form factors means the processing often needs to be wirelessly offloaded to an external device or cloud server to keep the device weight reasonable [8], which means the wireless connection needs to offer low latency and high data rate [8]. Also, recent Artificial Intelligence (AI) development brings powerful but heavy cloud-based generative AI models

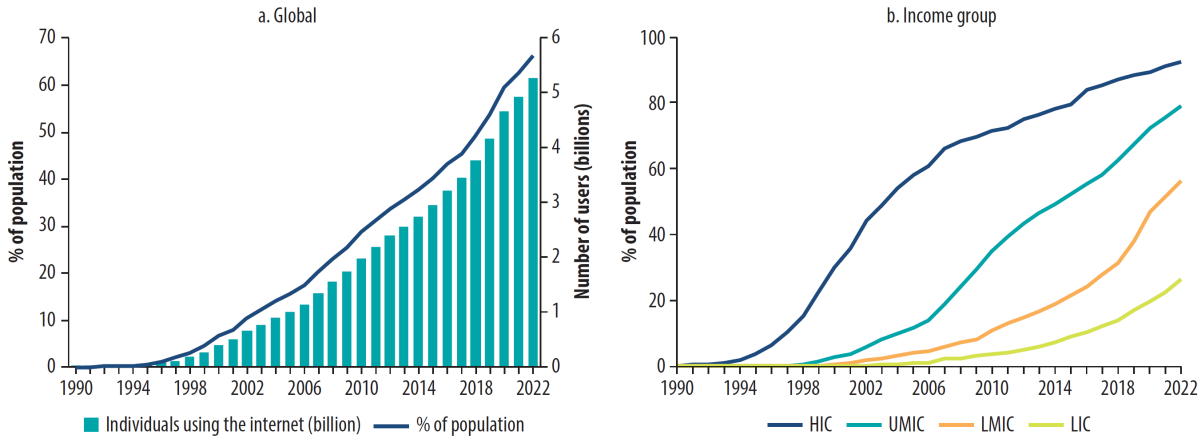


Figure 1.1: Internet users as a share of population, global and by country income group, 1990-2022. Note: HIC = high-income countries; LIC = low-income countries; LMIC = lower-middle-income countries; UMIC = upper-middle-income countries. [1]

to light (e.g. ChatGPT)[9]. A high wireless data rate is crucial for the efficient integration of cloud-based AI models into everyday tasks since without it, the high wait time will deteriorate the users' satisfaction towards the service. A recent example would be the disastrous launch of the Humane AI pin. The start-up company Humane, once valued at 850 million dollars [10], promised a wearable product that uses powerful AI models to assist people's lives [11]. However, since the Humane AI pin uses cloud-based AI models, each user's command needs to be uploaded to the cloud to be interpreted and processed and the result needs to be downloaded to the wearable device, which takes a bit too long to make this product to be considered "unusable" by many [11], highlighting the importance of a high data rate wireless link.

To enable millisecond latency and higher data rate wireless communication, the fifth-generation (5G) New Radio (NR) cellular network operates in millimeter-wave (mmWave) bands from 24.25GHz to 52.6GHz, in addition to the crowded sub-6GHz bands. This broad spectrum provides substantial bandwidth, achieving peak data rates of up to 20 gigabits per second (Gbps) [8]. The primary challenge with mmWave communication is the increased path loss due to severe atmospheric absorption at these frequencies [8, 2]. To mitigate high path loss and enhance spectral efficiency, technologies such as beamforming and multiple-input multiple-output (MIMO) are employed [8, 2].

Beamforming, a specific implementation of MIMO, utilizes multi-element antenna arrays to dynamically control the beam pattern by adjusting the spacing and phase/amplitude

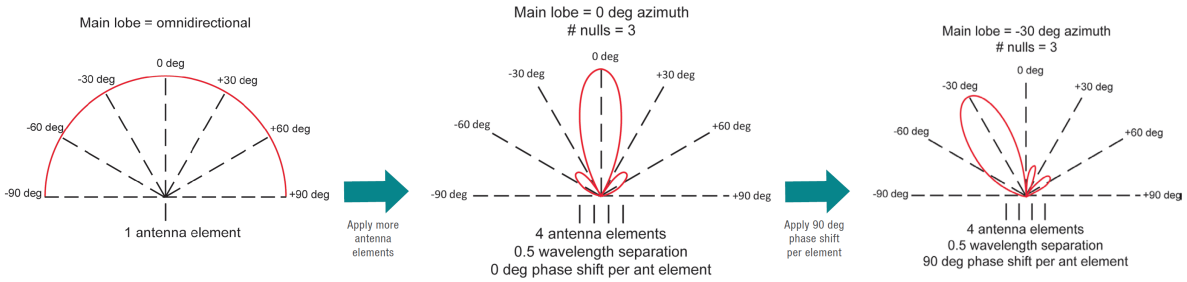


Figure 1.2: Illustration of beamforming by applying more antenna elements and phase shifts. [2]

shifts between antenna elements [2]. This configuration, known as a phased array, enables the constructive addition of radiated energy, thereby increasing power delivery and signal-to-noise ratio (SNR) to the user [2]. Each antenna element can electronically alter the magnitude and phase of the signal to shape the radiation pattern and rapidly steer the beam direction without mechanical movement [2]. Figure 1.2 illustrates the radiation pattern and electronic steering of beams. 5G technology will transition from cell-based to beam-based communications using multi-user MIMO, as demonstrated in Fig. 1.3.

The quality of service in beam-based radiation schemes depends on the pointing accuracy of the beams and power levels in each direction. For optimal phased array performance, the array must be calibrated, meaning the settings of each antenna element must produce the correct phase shift and amplitude modification (gain) for beamforming. In practical phased arrays, phase and gain errors arise from non-idealities and parasitics in the radio frequency (RF) circuit elements, fabrication variations, and non-negligible antenna couplings. If these errors are uncorrected, they can substantially deteriorate the radiation pattern as illustrated in Fig. 1.4. Further, it is expected that antenna arrays in the future, for both 5G or 6G cellular network and satellite communication, will be much larger to support more users and to use even higher frequency bands (THz) [8], which means the beams will be much sharper making the tolerable margin for the pointing error much lower in the future. Thus, phased array calibration is essential to ensure good beamforming performance now and even more so in the future.

Scaling up to phased arrays with thousands of antenna elements in the future, currently reported array calibration methods in the literature bring heavy trade-offs between the calibration accuracy and the calibration time. Falling into either extreme is unsuitable for the future development of the phased arrays. Thus, in this thesis, we propose a new phased array calibration method that strives to overcome those issues.

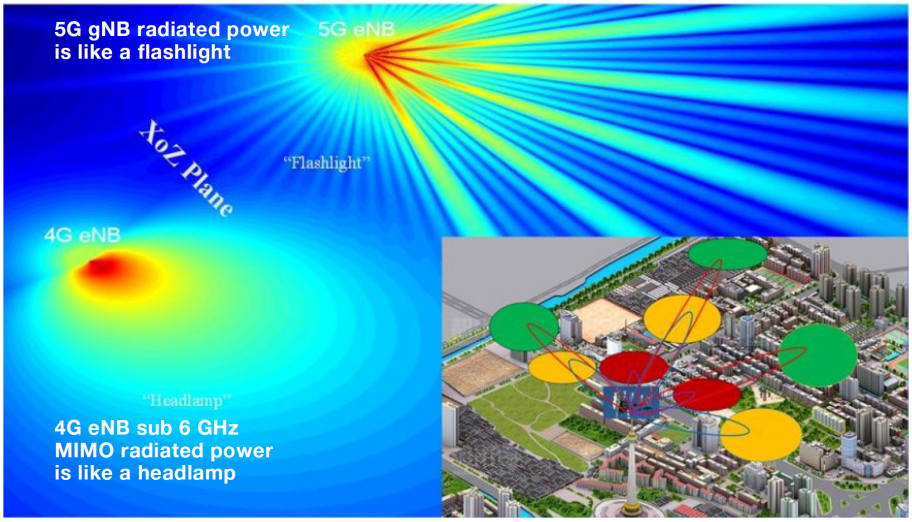


Figure 1.3: Radiated power from a 4G direction antenna vs. 5G beam-based antennas. [2]

1.2 Problem Statement

To fully control the radiation pattern, a myriad of radio-frequency (RF) beamforming architectures, documented in the literature [12, 13, 14, 15, 16, 17, 18], incorporates variable-gain phase-shifters (VGPS) on each RF branch, before the power amplifier (PA) in the transmitter (TX) and after the low noise amplifier (LNA) in the receiver (RX), to adjust the signals' amplitude and phase for beamforming, as depicted in Fig. 1.4. Since the VGPS is used for beamforming, it is categorized as a beamforming integrated circuit (BFIC). These VGPS shape the radiation pattern and steer it in the desired direction, facilitated by a digital control unit that transmits control code words based on the intended beam direction [12, 15, 16, 19, 18, 20, 21, 22]. However, in a practical implementation of a phased array, phase and gain tunning errors occur due to non-ideal signal division prior to the VGPS, non-ideal VGPS response versus its control codes, parasitic and fabrication variations and non-negligible antenna couplings. If phase and gain tuning errors are unaccounted for, the resulting radiation pattern will exhibit a lower main lobe (the region with the highest power), higher side lobes (other lobes that are not the main lobe), shallower nulls (regions with local minimum power), and pointing errors compared to an ideal radiation pattern. Thus, post-fabrication calibration is needed to ensure the array's beamforming performance.

The process of array calibration involves antenna measurement and error compensation. Various antenna measurement methods have been introduced in the literature, including

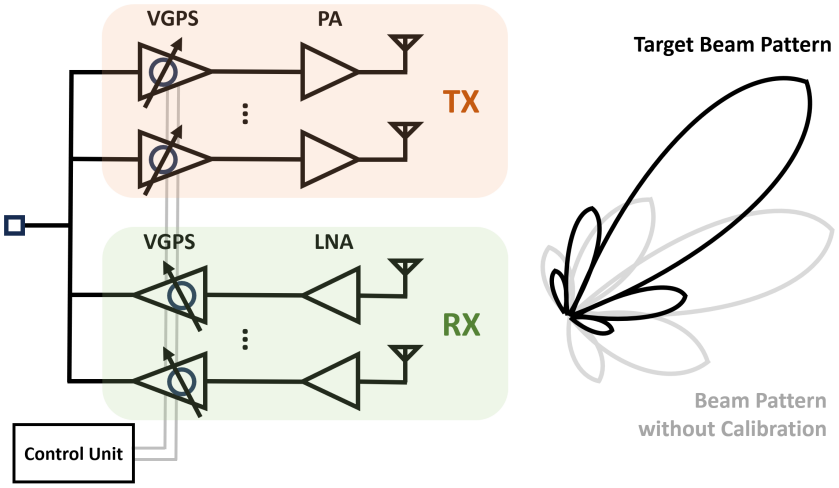


Figure 1.4: RF beamforming system illustrating the radiation pattern distortion due to hardware nonidealities.

mutual-coupling method [23, 3, 24], rotating-element electric field vector (REV) method [4, 25, 26], orthogonal coding method [5, 27, 28] and complex excitation method [29, 30, 31]. To compensate for the measured errors, two primary models are considered in the calibration of phased arrays.

The first is the constant error model, which assumes that phase and gain errors remain constant across all control states. Calibration processes using this model conduct measurement(s) for each element and apply a constant excitation offset for correction [4, 25, 26, 27, 28, 29, 30, 31]. This model allows array calibration to be achieved with as few measurements as there are elements in the array. However, as demonstrated in Fig. 1.5, the error often varies with both gain and phase, which limits the effectiveness of the constant error model [32, 33].

The other error model acknowledges that errors vary with both gain and phase control indices. In the literature, calibrations using this varying error model perform measurements for every combination of control states. Then, as shown in 1.5, those corresponding to the desired constellation are picked[34, 35, 19, 22, 36]. This method, termed exhaustive search, assumes no prior knowledge of the array elements' response, necessitating the full measurements of the array. The major drawback of this method is its extensive measurement time, which poses a significant challenge for large and/or high-resolution arrays. Methods such as the pseudo-exhaustive search [33] utilize interpolation to reduce the required number of measurements for the full constellation. However, this method results in a heavy trade-off

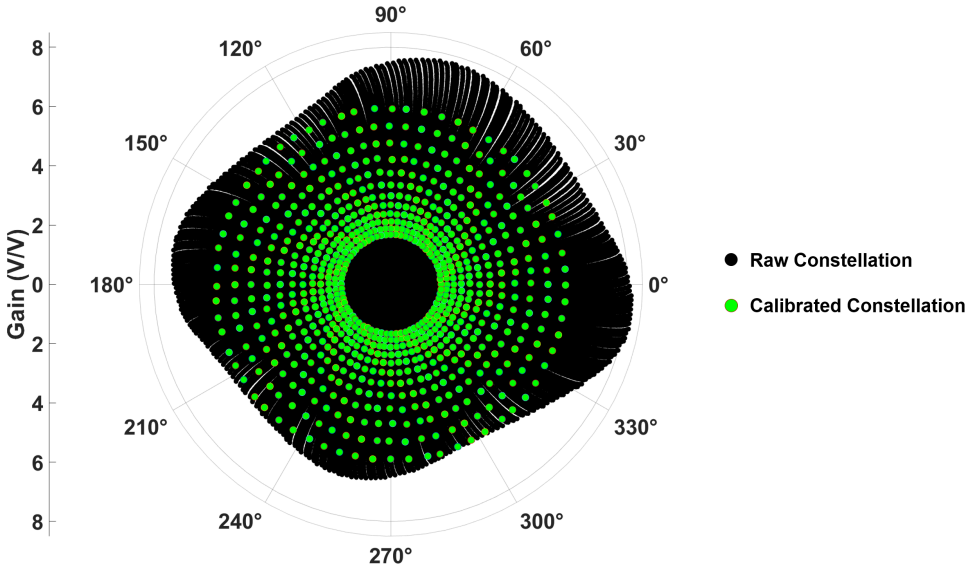


Figure 1.5: Raw and calibrated constellation corresponding to the 8-bit phase and 8-bit gain states of the VGPS and the calibrated 6-bit phase and 12 gain states with 1dB gain tuning resolution, respectively.

between sampling size and accuracy.

Simplifications of the varying error model exist in the literature. Methods employing these partial varying error models assume gain and phase control errors are decoupled. For example, the control sampling method [32] quantifies the control relationships by measuring a constant gain series and a constant phase series. The captured control relationships are then interpolated for the gain and phase control codes corresponding to the targeting gain and phase. However, because gain and phase responses are not isolated from each other in practice, the captured control relationships are not static and do not accurately apply to the entire constellation.

In this work, we incorporate the varying error model to achieve the highest accuracy. However, instead of measuring every state and assuming no prior knowledge of the array elements' response, we model the elements' constellations, characterizing them using sub-sampled measurements. Figure 1.5 shows an example of a calibrated constellation for an array element. We propose a novel characterization method for the array elements, enabling rapid calibration of phased arrays. This approach achieves calibration performance comparable to the Exhaustive Search method while significantly reducing the number of measurements required. We introduce two calibration routines utilizing this characteriza-

tion method, each offering a different balance between calibration speed and robustness. To further expedite phased array calibration, a channel transformation technique has been developed that leverages the inherent similarities between array elements, facilitating a more intelligent and efficient calibration process.

In this thesis, we propose a new phased array calibration algorithm that aims to achieve the following:

1. The proposed method characterizes an array element using a small set of measurements and calibrates it to a comparable accuracy as to the exhaustive search method.
2. For verified performance, the proposed method efficiently searches for the optimal codes that meet the specified performance requirements.
3. For large arrays, the proposed method efficiently transforms the characterized model from element to element further reducing the number of measurements needed.

The objective of this work is not necessarily to develop a universal calibration algorithm for all types of arrays implemented with all types of BFICs, but rather to demonstrate the feasibility and high performance of such kind of calibration algorithm. The goal is to achieve such significant performance improvements that the industry will be motivated to design more arrays suited for this algorithm. These arrays would prioritize elements that exhibit a largely continuous constellation with natural patterns, rather than elements with corrected phase and gain responses. Additionally, this algorithm encourages the development of high-resolution arrays, facilitating the future calibration of massive high-resolution arrays.

1.3 Thesis Organization

This thesis is organized as follows.

Chapter 2 provides background information on beamforming and phased arrays, along with a literature review of relevant array calibration methods. Chapter 3 discusses the development and implementation of the proposed characterization method, detailing its components and experimental validation. Chapter 4 introduces the channel transformation technique, describing its components and experimental validation. Chapter 5 concludes the thesis, summarizing the findings and contributions.

Chapter 2

Background and Literature Review

2.1 Background on Beamforming and Phased Array

Beamforming is a signal processing technique used to direct the transmission or reception of signals in specific directions, rather than broadcasting them uniformly in all directions. This directional control is achieved through the constructive and destructive interference of signals from the array's elements. By appropriately adjusting the phase and amplitude of the signal at each element, beamforming enhances signal strength in desired directions and mitigates interference from unwanted directions. This process significantly improves the signal-to-noise ratio (SNR), equivalent isotropic radiated power (EIRP) and overall system performance.

A key concept in the analysis and design of phased arrays is the Array Factor (AF) which describes the spatial array gain compared to the isotropic radiators as the result of the grouping of the antennas. Figure 2.1 illustrates a linear array with N antennas and with antenna spacing of d. The array factor of this linear array is calculated as:

$$AF(\theta) = \sum_{n=0}^{N-1} \alpha_n e^{j(\phi_n - nkd\,cos(\theta))} \tag{2.1}$$

and the normalized array factor $\overline{AF}$ is calculated as:

$$|\overline{AF}(\theta)| = \frac{1}{N}\left|\sum_{n=0}^{N-1} \alpha_n e^{j(\phi_n - nkd\,cos(\theta))}\right| \tag{2.2}$$

where θ is the observing angle of the array (demonstrated in Figure 2.1), $k = 2\pi/\lambda$ is the wave-number, and α_n and ϕ_n are the magnitude and phase of the complex excitation coefficient of the n-th antenna element.

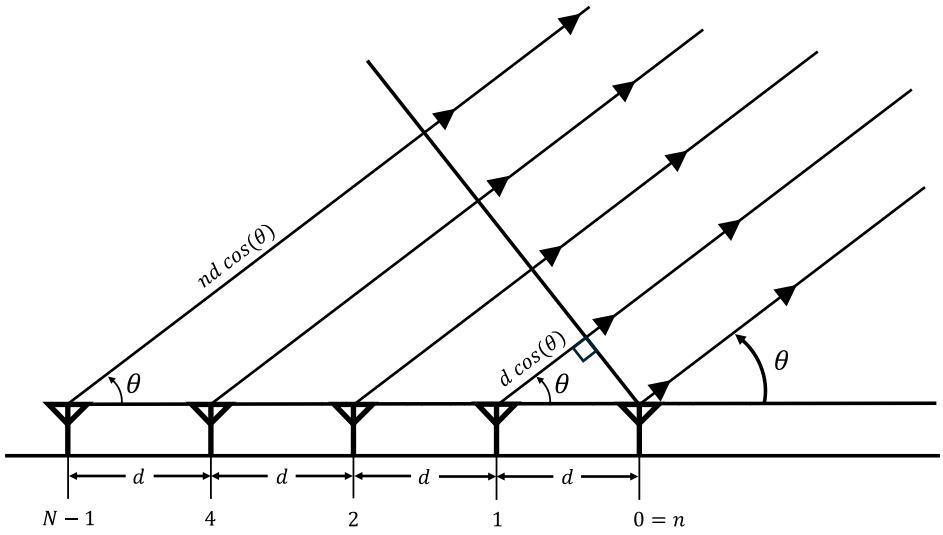


Figure 2.1: Demonstration of a linear array with N elements.

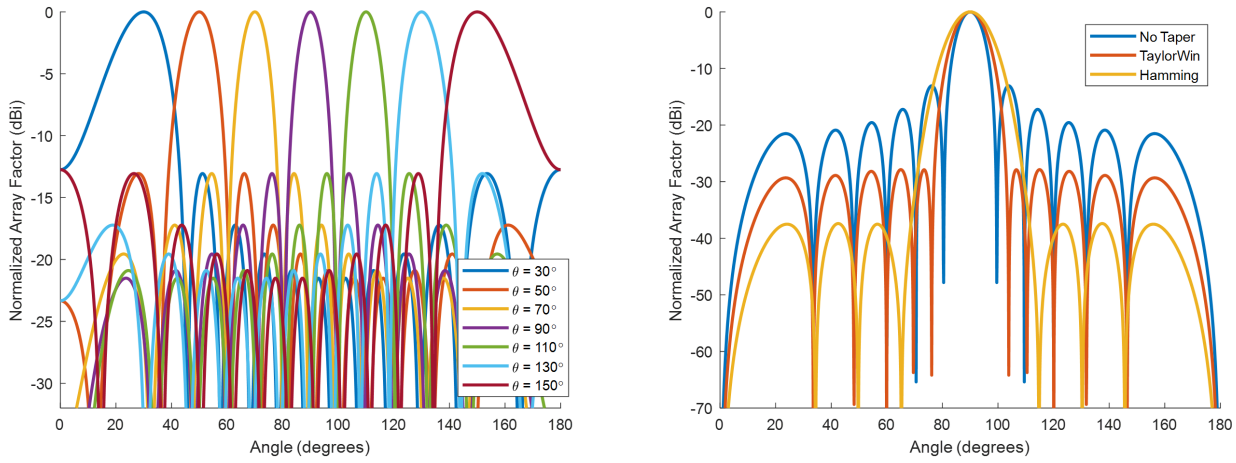


Figure 2.2: Normalized Array factor for a linear array of 12 elements: (a) Beam steering; (b) Gain tapering using different tapering profiles.

As indicated by Equation (2.1), a set of phase excitations ϕ_n can be selected for the array factor to reach the maximum at the desired angle, thereby steering the beam, as demonstrated in Figure 2.2a. Additionally, the magnitude excitations α_n can be selected to alter the shape of the radiation pattern, achieving a narrower beam and lower side-lobes. This change in antenna magnitude excitation is referred to as "Gain Tapering" and its effects are demonstrated in Figure 2.2b.

The array factor in (2.1) can be extended to a 2D array with antenna elements tiled with spacing d_x and d_y. The array factor (AF) of a $N \times M$ array is expresses as:

$$AF(\theta, \phi) = \sum_{n=0}^{N-1} \sum_{m=0}^{M-1} \alpha_{n,m} e^{j(\phi_{n,m} - k\, sin(\theta)(n d_x cos\,(\phi) - m d_y sin\,(\phi))} \tag{2.3}$$

where θ and ϕ are the polar and azimuthal spherical coordinates of the observer in far-field.

To realize the complex excitations for the array to achieve the desired array factor, and consequently the radiation pattern, various beamforming architectures are proposed in the literature. Digital beamformers, as demonstrated in Figure 2.3a, encode the desired excitations in the digital domain via digital signal processor (DSP) in the signal baseband. Analog beamformers, as demonstrated in Figure 2.3b, encode the desired excitations in the analog domain via circuit elements such as the variable-gain phase-shifters (VGPS). Depending on where the encoding is implemented, analog beamforming can be further categorized into radio-frequency (RF) beamforming, local oscillator (LO) beamforming and intermediate-frequency (IF) beamforming. Finally, the hybrid beamformer, as demonstrated in Figure 2.3c, uses both digital and analog means for encoding the desired excitations.

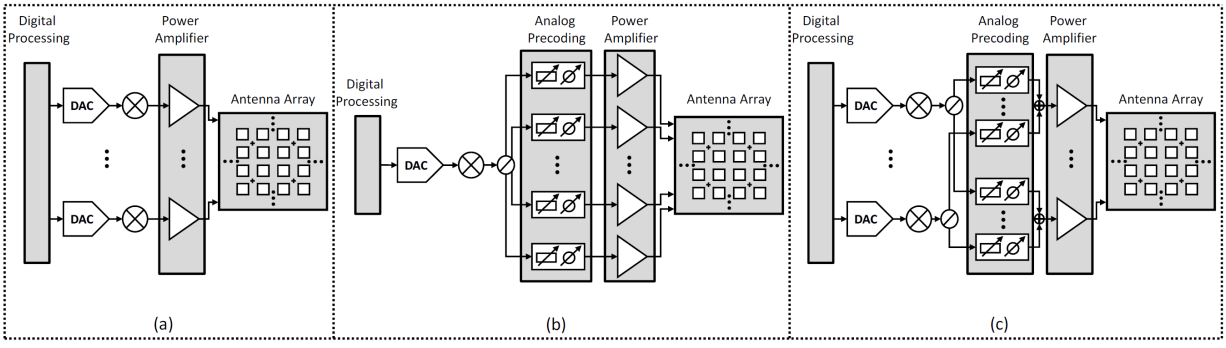


Figure 2.3: Block diagram of different beamforming architectures: (a) Digital beamforming; (b) Analog beamforming; (c) Hybrid beamforming.

2.2 Literature Review on Antenna Array Measurement Methods

2.2.1 Element-by-Element Direct Measurement Method

The Element-by-Element Direct Measurement Method is a traditional and fundamental approach used for the calibration and characterization of phased array antennas. This method involves individually measuring the response of each antenna element to obtain precise amplitude and phase information. Despite being time-consuming, this method is known for its high accuracy and is often used as a benchmark for other calibration techniques.

The principle of this method is straightforward: each element in the array is measured independently while the other elements are turned off or set to a known state. This isolation ensures that the measured response of each element is not influenced by the others, providing accurate amplitude and phase data. This method is primarily used in scenarios where high accuracy is essential and where the number of elements in the array is manageable.

While the Element-by-Element Direct Measurement Method is not suitable for all situations due to its time and resource requirements, its accuracy makes it an invaluable tool for certain calibration tasks in the development and maintenance of phased array antennas.

2.2.2 Mutual Coupling Method

Mutual coupling in antenna arrays refers to the interaction between nearby antenna elements, significantly influencing the array's performance. This phenomenon, traditionally seen as a challenge, has been harnessed for array calibration and optimization in various studies. The mutual coupling method offers a robust solution for in-situ calibration of phased arrays, particularly in modern communication systems like 5G.

The concept of using mutual coupling for antenna calibration was pioneered by Aumann et al. in 1989. They demonstrated that a phased-array radar could self-calibrate using coupling symmetries with its nearest neighbors [23]. Shipley and Woods extended this concept to slot elements on an isosceles grid, highlighting its versatility across different antenna configurations [37].

Recent advancements have focused on enhancing these techniques. Nafe et al. developed the Quad-BIST (Built-In Self-Test) method, which utilizes mutual coupling in 5G

phased arrays for self-test and calibration. This method arranges antenna elements in a quad formation and uses coupling symmetries to extract calibration coefficients, enabling precise gain and phase characterization [3].

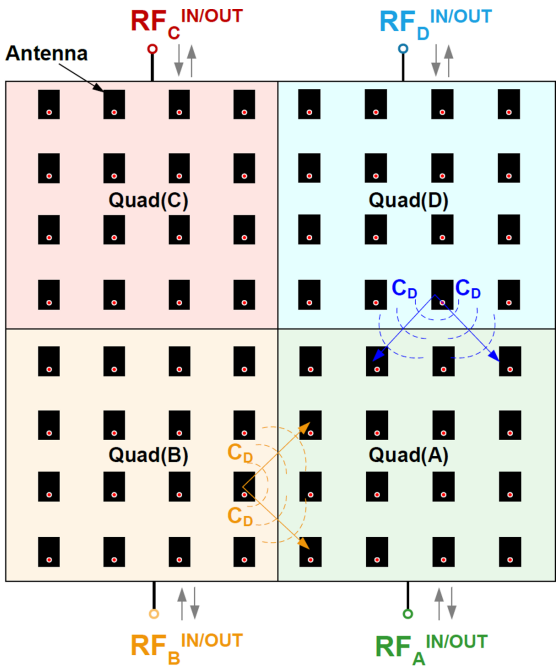


Figure 2.4: Quad-based self-calibrating multi-beam TRX phased-array using antenna mutual coupling. [3]

The mutual coupling calibration process involves several key steps and equations. Consider a set of antenna arrays arranged in a quad formation (Fig. 2.4). The calibration coefficient for a given antenna element is determined by measuring the coupling between neighboring elements. The steps for calibration can be summarized as follows:

1. Calibrating Rows: The coupling between two antenna elements is measured using an S-parameter measurement, typically S_{21}, which represents the transmission coefficient from one element to another. To calibrate the first row, we start by transmitting from antenna $b_{1,2}$ (Fig. 2.5) and receiving from antenna $a_{1,1}$ and then receiving from $a_{1,3}$. These two measurements can be expressed as:

$$M_1(b_{1,2} \rightarrow a_{1,1}) = \frac{S_{\text{out}}}{S_{\text{in}}} = b_{1,2} C_D^1 a_{1,1} \tag{2.4}$$

$$M_2(b_{1,2} \rightarrow a_{1,3}) = \frac{S_{\text{out}}}{S_{\text{in}}} = b_{1,2} C_D^1 a_{1,3} \tag{2.5}$$

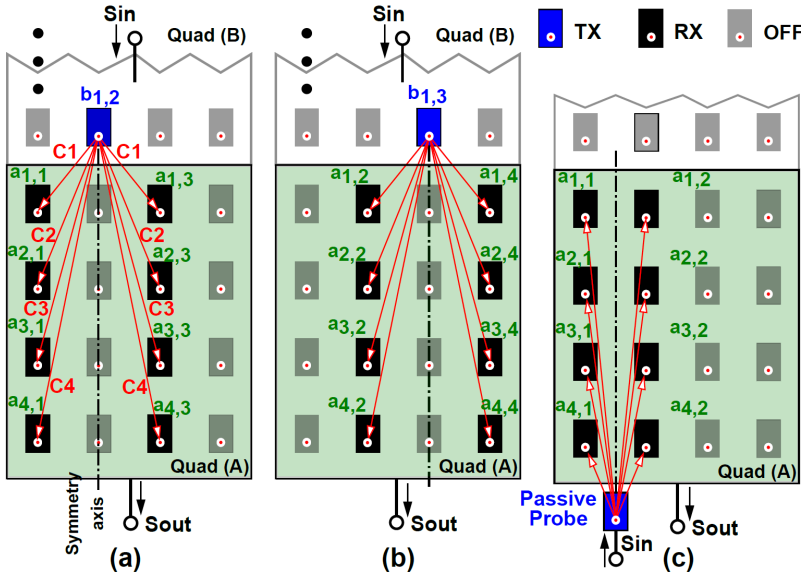


Figure 2.5: Exploiting antenna coupling symmetry to calibrate the array rows: (a) pivoting at $b_{1,2}$, (b) pivoting at $b_{1,3}$ and (c) pivoting at an extra passive probe antenna. [3]

The calibration coefficient κ for channel $a_{1,3}$ can be directly obtained by dividing the two measurements, as the coupling factor for the transmit channel is common for both paths:

$$\kappa_{1,3}^{1,1} = \frac{M_2}{M_1} = \frac{b_{1,2}C_D^1 a_{1,3}}{b_{1,2}C_D^1 a_{1,1}} = \frac{a_{1,3}}{a_{1,1}} \tag{2.6}$$

Using similar steps, $b_{1,3}$ can pivot channels $a_{1,2}$ and $a_{1,4}$ to obtain:

$$\kappa_{1,2}^{1,4} = \frac{a_{1,2}}{a_{1,4}} \tag{2.7}$$

and the external passive probe can pivot $a_{1,1}$ and $a_{1,2}$ to obtain:

$$\kappa_{1,2}^{1,1} = \frac{a_{1,2}}{a_{1,1}} \tag{2.8}$$

and we can also calculate $\kappa_{1,4}^{1,1}$ as:

$$\kappa_{1,4}^{1,1} = \kappa_{1,4}^{1,2} \times \kappa_{1,2}^{1,1} \tag{2.9}$$

With these steps, the calibration coefficients for the first row relative to $a_{1,1}$: $\kappa_{1,2}^{1,1}$, $\kappa_{1,3}^{1,1}$, $\kappa_{1,4}^{1,1}$) are all known. This process is repeated for rows 2, 3, and 4 to obtain all channels relative to the reference channels in the first column $a_{i,1}$.

2. Calibrating Columns: Once the rows are calibrated, the columns are calibrated similarly using neighboring quads. The entire array can thus be calibrated relative to a reference element, typically $a_{1,1}$.

The mutual coupling method offers a compact, efficient, and accurate means of calibrating phased arrays, particularly for in-situ applications in dynamic environments. This method is well-suited for modern 5G and MIMO systems, ensuring optimal performance through continuous self-calibration.

2.2.3 Rotating-Element Electric-field Vector (REV) Method

The Rotating-Element Electric-Field Vector (REV) method is a recognized technique for calibrating phased array antennas by measuring the active electric fields of individual antenna elements. Proposed by Yonezawa et al., it eliminates the need for phase measurements, making it convenient for initial calibration and in-situ diagnostics of phased arrays [38].

The classic REV method involves shifting the phase of a single antenna element while measuring array power variations. As shown in Figure 2.6, the principle is based on the oscillation of the combined electric field vector's magnitude as one vector's phase rotates.

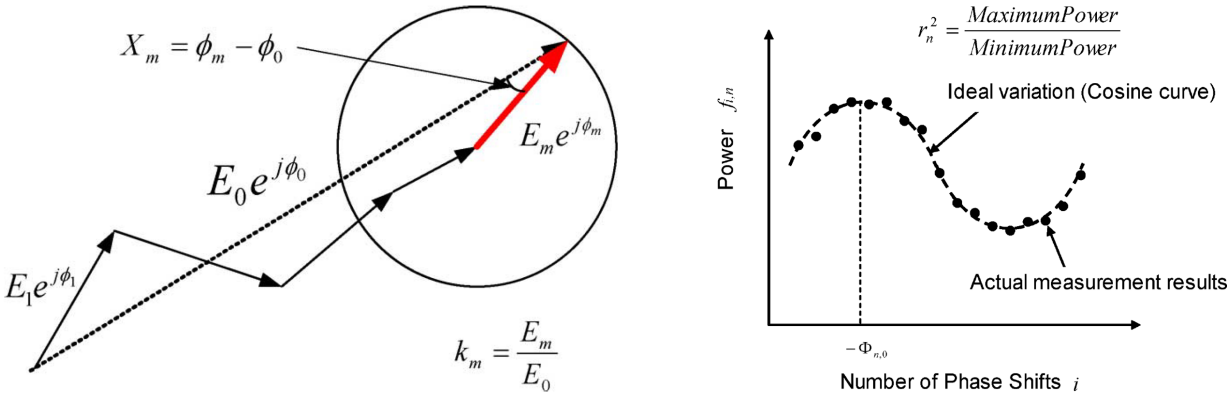


Figure 2.6: REV principle: (a) The array field is the vector sum of the electric fields of individual elements; (b) Sinusoidal array power variation measured. [4]

The REV method determines the complex electric field of an element based on three parameters: maximum power, minimum power, and the phase shift corresponding to maximum power. The fundamental steps include successively shifting the phase of antenna

elements from 0 to 360 degrees, determining the maximum and minimum power levels, and identifying the phase shift at maximum power. The complex electric field of each element is then calculated using these parameters.

When the phase of an antenna element is altered by its phase shifter, the composite vector varies as the element field vector rotates. By measuring the amplitude variation of the composite vector, the amplitude and phase of the element can be determined as follows [38]:

In Figure 2.6a, the amplitude and phase of the composite field vector in the initial state are denoted by E_0 and ϕ_0, and those of the m-th element by E_m and ϕ_m. When the phase of the m-th element is varied by Δ, the composite field can be expressed as

$$\dot{E} = (E_0 e^{j\phi_0} - E_m e^{j\phi_m}) + E_m e^{j\phi_m + \Delta} \tag{2.10}$$

Here, the relative amplitude K and relative phase X of the m-th element are defined as:

$$K = \frac{E_m}{E_0}, \quad X = \phi_m - \phi_0 \tag{2.11}$$

Figure 2.6b shows that the composite power varies sinusoidally as the phase of one element changes. The relative amplitude and phase of the element are determined by:

$$\Gamma = \frac{r-1}{r+1} \tag{2.12}$$

$$K = \frac{\Gamma}{\sqrt{1 + 2\Gamma \cos \Delta_0 + \Gamma^2}} \tag{2.13}$$

$$X = \tan^{-1}\left(\frac{\sin \Delta_0}{\cos \Delta_0 + \Gamma}\right) \tag{2.14}$$

where r is the ratio of the maximum and minimum of the composite power, and $-\Delta_0$ is the phase that gives the maximum composite power. The relative amplitude and phase distribution of the phased array are detected by changing the phase of each element one by one and measuring the change in composite power.

The REV method simplifies the calibration process by avoiding direct phase measurements, instead relying on power variations as the phase of a single element is altered. This is particularly advantageous for phased array antennas where precise phase control and measurement can be challenging.

Takahashi et al. proposed a fast measurement technique utilizing the REV method principles to measure the active electric fields of multiple elements simultaneously. This

method expands the measured power variation into a Fourier series and rearranges the terms to match the REV solution [4].

Liu and Feng introduced a combined REV method for near-field calibration of large-scale phased arrays. This method synchronously alters the phases of a group of elements by their phase shifters, improving the signal-to-noise ratio and limiting the dynamic range of the signal. The combined REV method achieves higher precision and efficiency, particularly for large arrays where traditional methods may be less effective [26].

The REV method and its improvements provide effective calibration techniques for phased array antennas. The combined REV method, in particular, offers enhanced accuracy and efficiency, making it suitable for modern large-scale phased arrays. These advancements ensure precise calibration necessary for high-performance applications in radar and communication systems.

2.2.4 Orthogonal Coding Method

The Orthogonal Coding Method is an advanced technique for calibrating phased array antennas using orthogonal codes to encode and decode signals from each array element. This method, part of the broader complex excitation method, solves systems of equations to determine the relative amplitudes and phases of each antenna element. By enabling simultaneous in-situ measurement of all elements, it significantly reduces calibration time compared to sequential methods.

Orthogonal coding utilizes codes like Walsh-Hadamard codes to uniquely encode signals from each antenna element. These encoded signals are transmitted and captured by a calibration probe, either in the near-field or far-field of the array (as shown in Fig. 2.7). The received signals are processed with a decoding algorithm to extract the relative amplitude and phase of each element.

Seth D. Silverstein's pioneering work in 1997 significantly advanced this method. He introduced algorithms that transmit time-multiplexed orthogonal encoded signals, which are coherently detected, accumulated in vector forms, and decoded using the inverse of the orthogonal encoding matrix [27]. His algorithms, Unitary Transform Encoding (UTE) and Control Circuit Encoding (CCE), were designed for remote calibration of active phased array antennas.

The CCE technique employs orthogonal coding to calibrate digitally controlled phased arrays. It sequentially applies orthogonal codes to the attenuators and phase shifters in the beamformer, allowing in-situ measurement of all elements. The key steps of the CCE technique include:

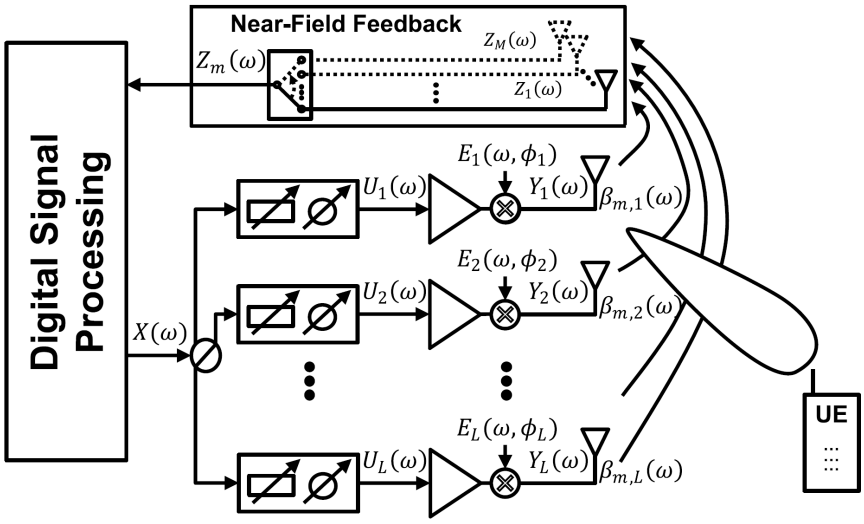


Figure 2.7: Block diagram of RF beamforming array with embedded NF probes for array calibration and DPD training. [5]

1. Encoding: Apply orthogonal codes to the beamformer, controlling the attenuators and phase shifters based on a Hadamard matrix.
2. Measurement: Perform measurements on the composite signal received by the calibration probe, containing information from all elements.
3. Decoding: Use the inverse of the Hadamard matrix to decode the measurements and extract the relative amplitude and phase of each element.

The mathematical formulation of the encoding and decoding process is given by:

$$H_n = \begin{bmatrix} H_{n/2} & H_{n/2} \\ H_{n/2} & -H_{n/2} \end{bmatrix} \tag{2.15}$$

where H_n is the Hadamard matrix of order n.

Decoding the measurement set $y(m)$ is performed using the inverse Hadamard matrix H^{-1}, which is equal to the Hadamard matrix H:

$$z(k) = \frac{1}{M} \sum_{m=1}^{M} H(m,k) y(m) \tag{2.16}$$

where $z(k)$ contains the extracted information from the k-th element.

The orthogonal coding method has proven effective in various phased array calibration scenarios. Lier et al. demonstrated its effectiveness on active phased array antennas, achieving fast and accurate calibration [28]. The method's ability to measure all elements simultaneously offers significant time savings and improved accuracy due to coherent integration.

Ben Ayed et al. [5] proposed an advanced calibration technique using embedded near-field feedback probes and orthogonal coding for millimeter-wave beamforming arrays. This method enhances RF beamforming array performance by characterizing linear and nonlinear errors without the need for far-field feedback. Experimental results on a 16-element array showed significant improvements in radiation pattern accuracy and effective isotropic radiated power (EIRP).

In summary, the orthogonal coding method is a highly efficient and accurate technique for phased array calibration. Its capability for simultaneous in-situ measurement of all elements, combined with the use of orthogonal codes, makes it an invaluable tool for modern phased array systems.

2.3 Literature Review on Control-Error Compensation Methods

2.3.1 Constant Error Compensation Method

The Constant Error Compensation Method offers a simple approach to calibrating phased array antennas by applying a fixed excitation offset derived from measured errors, assuming these errors remain consistent across different control states. This method enables calibration with minimal measurements, typically requiring only as many as the number of elements in the array.

However, its primary limitation lies in the assumption of constant errors. When errors vary significantly with control states, this method can lead to inaccuracies. Despite this drawback, it remains the fastest error compensation method available, making it ideal for scenarios where speed is prioritized over precision.

2.3.2 Exhaustive Search Method

The Exhaustive Search Method is a comprehensive approach used for the calibration and optimization of phased array antennas. This method involves measuring all possible states

of the array elements to identify the optimal settings that achieve the desired performance. While this method ensures the highest accuracy, it is often computationally intensive and time-consuming.

This method does not rely on any prior assumptions or models, making it a brute-force approach to finding the optimal solution. By exploring all possible settings, this method ensures that the optimal settings are identified without relying on approximations or assumptions. The thorough nature of this method provides highly accurate results, making it suitable for critical calibration tasks where precision is essential.

However, the Exhaustive Search Method also has significant limitations. This method requires a large number of evaluations, especially for high-resolution arrays with many elements, making it computationally demanding. The extensive number of measurements needed can result in long calibration times, making the method impractical for real-time or large-scale applications. Also, practical concerns include the potential response variation of the array during the long measurement which deteriorates the accuracy of the calibrated settings.

In conclusion, the Exhaustive Search Method, while not practical for all situations due to its high computational and time demands, provides a benchmarking approach for the calibration and optimization of phased array antennas.

2.3.3 Pseudo-Exhaustive Search Method

The Pseudo-Exhaustive Search Method is a streamlined approach to calibrating phased array antennas, specifically designed to address the extensive measurement demands of the exhaustive search method [33]. By selectively sampling a subset of the BFIC responses and then interpolating the full constellation, this method drastically reduces the number of measurements required.

A key aspect of this method is the trade-off between accuracy and the number of measurements. While it significantly lowers the measurement burden, making calibration faster and more efficient, this comes at the cost of potentially reduced accuracy compared to a full exhaustive search. The fewer measurements taken, the greater the reliance on estimation, which can lead to less precise calibration outcomes.

In summary, the pseudo-exhaustive search method offers a practical balance, prioritizing efficiency over the absolute accuracy of the exhaustive search, making it well-suited for applications where rapid calibration is necessary and slight compromises in precision are acceptable.

2.3.4 Control Sampling Method

The Control Sampling Method is a widely used technique in the industry as a fast alternative to the exhaustive search method for calibrating and testing phased array antennas [32].

The Control Sampling Method evolved to address the need for efficient and accurate calibration of increasingly complex phased array systems. Traditional calibration methods, which involved exhaustive sampling of all elements, were impractical for large arrays due to time and resource constraints. The Control Sampling Method reduces the number of measurements required by selecting key control points that accurately represent the array's overall behavior.

Let G and P be the sampled gain and phase control relationships, respectively. The complex transmission coefficient measured by setting the gain index I_G and phase index I_θ to the array elements is denoted as M_{I_G,I_θ}:

$$G(I_G) = \left|M_{I_G,I_{\theta,\text{fixed}}}\right|, \quad \text{for } I_G \in \{I_{G,\min}, \ldots, I_{G,\max}\} \tag{2.17}$$

$$P(I_\theta) = phase(M_{I_{G,\text{fixed}},I_\theta}), \quad \text{for } I_\theta \in \{I_{\theta,\min}, \ldots, I_{\theta,\max}\} \tag{2.18}$$

where $I_{G,\text{fixed}}$ and $I_{\theta,\text{fixed}}$ are the fixed gain and phase indexes when the other control is swept. $I_{G,\min}$, $I_{G,\max}$, and $I_{\theta,\min}$, $I_{\theta,\max}$ are the minimum and maximum of the respective gain and phase indexes of the array element.

From the sampled control relationships, the gain and phase indexes for a desired constellation point with magnitude G_t and phase θ_t are calculated via interpolation:

$$I_G = G^{-1}(G_t) \tag{2.19}$$

$$I_\theta = P^{-1}(\theta_t) \tag{2.20}$$

This method isolates gain control errors from phase control errors and, as a result, is not highly effective at accurately solving the indexes for the entire constellation. This limitation is evidenced by the fact that the gain and phase control relationships vary with different $I_{G,\text{fixed}}$ and $I_{\theta,\text{fixed}}$. To increase accuracy, multiple gain and phase control relationships can be sampled to describe a broader constellation region. The control sampling method presents a fundamental trade-off between accuracy and measurement time [32].

In conclusion, the Control Sampling Method offers an alternative to exhaustive search methods for applications requiring rapid phased array calibrations and are less sensitive to calibration accuracy.

2.4 Calibration Performance Matrices

We incorporate two important performance metrics to indicate the accuracy of array calibration. For an array element, the gain and phase root mean square errors (RMSE) indicate the deviation of the achieved gain and phase from the targeted ideal gain and phase in their respective units. The error vector magnitude (EVM) compares the measured constellation with the ideal constellation and measures the positional errors of the individual points.

Minimal RMSE and EVM are desired for the best array calibration performance. It should be noted that the RMSE and EVM by means of calibration alone cannot be minimized to zero, and the limit is set by the result of the exhaustive search method.

2.4.1 Root Mean Square Errors (RMSE)

The Root Mean Square Error (RMSE) is a standard way to measure the error of a model in predicting quantitative data. It represents the square root of the average of the squares of the errors—the differences between predicted and observed values. In the context of array calibration, RMSE is used to measure the deviations of the achieved gain and phase from their targeted values. The RMSE for gain ($RMSE_{G_{dB}}$) in decibels and phase ($RMSE_P$) in degrees can be defined as follows:

$$RMSE_{G_{dB}} = \sqrt{\frac{1}{N}\sum_{i=1}^{N}(20log_{10}(G_{\text{measured},i}) - 20log_{10}(G_{\text{target},i}))^2} \tag{2.21}$$

$$RMSE_P = \sqrt{\frac{1}{N}\sum_{i=1}^{N}(P_{\text{measured},i} - P_{\text{target},i})^2} \tag{2.22}$$

where N is the number of measurements, $G_{\text{measured},i}$ and $P_{\text{measured},i}$ are the measured gain and phase, and $G_{\text{target},i}$ and $P_{\text{target},i}$ are the target gain and phase values.

2.4.2 Error Vector Magnitude (EVM)

The Error Vector Magnitude (EVM) is a measure representing the difference between the ideal constellation points and the measured points, providing an indication of the positional

errors of the constellation points. EVM is expressed as a percentage, with lower values indicating better performance.

Representing the targeted and measured gain and phase as complex constellation points in space:

$$C_{target,i} = G_{target,i}\ e^{jP_{target,i}} \tag{2.23}$$

$$C_{measured,i} = G_{measured,i}\ e^{jP_{measured,i}} \tag{2.24}$$

where $C_{\text{measured},i}$ is the measured constellation point, and $C_{\text{target},i}$ is the targeted constellation point. The EVM is defined as follows:

$$EVM = \frac{\sqrt{\sum_{i=1}^{N} |C_{\text{measured},i} - C_{\text{target},i}|^2}}{\sqrt{\sum_{i=1}^{N} |C_{\text{target},i}|^2}} \times 100\% \tag{2.25}$$

where N is the number of constellation points.

Chapter 3

Rapid Calibration of BFICs/Phased Arrays using Novel Constellation Characterization Method

3.1 Calibration Routine Overview

In this section, we treat VGPS and array elements as a black box that takes in two control codes ("gain index" and "phase index") and outputs a point (complex transmission coefficient) with magnitude of "gain" and angle of "phase" as illustrated in Fig. 3.1. The gain index is mathematically denoted as I_G and the phase index is mathematically denoted as I_θ and the measurement result corresponding to the gain index of I_G and phase index of I_θ is mathematically denoted as M_{I_G,I_θ}. For simplification, we treat the black box model, which contains the combined response of the entire RF chain, as a single VGPS/Array Elements with some control state-dependent errors. The calibration of this black box is referred to as "VGPS calibration" in this thesis.

The outcome of our proposed characterization algorithm is the generation of "Mapping Functions", as illustrated in Fig. 3.2. These generated mapping functions are subsequently utilized in either the "unsupervised" calibration routine or the "supervised" calibration routine to generate the calibrated control codes for a requested constellation. In the "unsupervised" calibration routine, the generated mapping functions, along with an iterative control code solver, are used to solve for all the requested constellation points, as depicted in Fig. 3.3. For applications requiring enhanced calibration robustness, the "supervised" routine provides verified performance by employing a custom search algorithm, termed

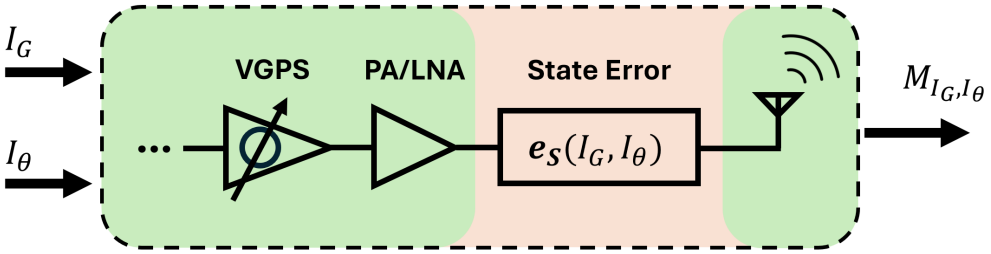


Figure 3.1: Response definition of VGPS/Array Elements.

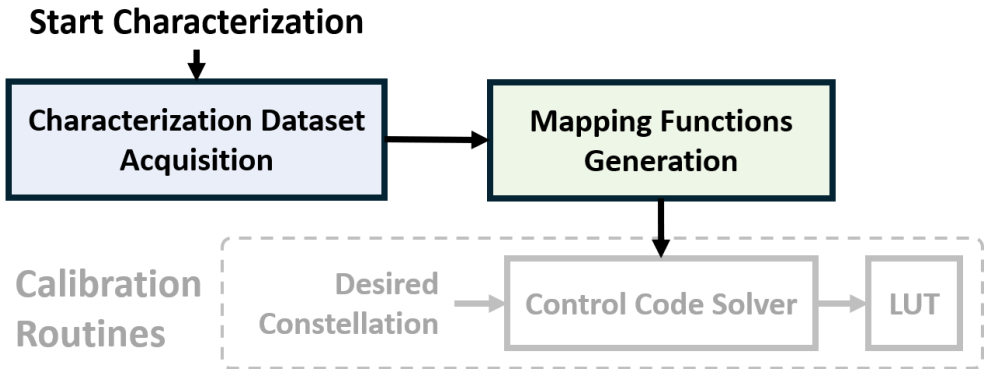


Figure 3.2: Top-level flow diagram of the novel VGPS characterization process.

"Adaptive Kernel Search", to validate the results obtained from the unsupervised routine, as shown in Fig. 3.4. Detailed descriptions of these two calibration routines are provided in the following sections.

The user can describe the targeting VGPS constellation in many ways. The typical scheme is to specify the needed phase resolution, the number of gain steps, as well as the gain tuning resolution. One important implementation detail for all calibration routines presented in this thesis is that every measurement is stored with its requested control codes ("gain index" and "phase index") and the channel index (for VGPS with multiple channels and arrays) as its access. This means that if the device is repeatedly requested with the same control codes, no redundant measurement will be taken, and the result is read directly from memory.

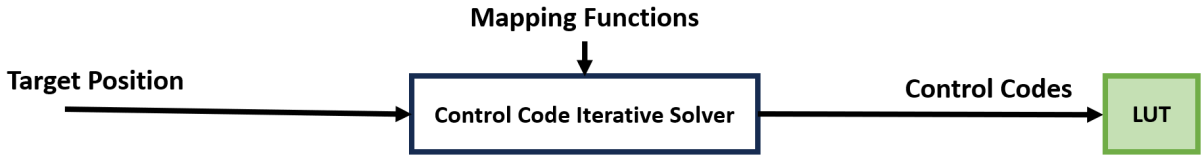


Figure 3.3: Flow diagram of the proposed unsupervised calibration routine.

3.1.1 Unsupervised Calibration Routine

The unsupervised calibration routine is an open-loop calibration solution, illustrated in Fig. 3.3, which only uses the generated mapping functions to solve for the LUT corresponding to the desired constellation.

The number of measurements needed for the "unsupervised" calibration is fixed and equal to the number of measurements for the proposed characterization. Thus, the measurement time will retain its minimum even for the largest number of targeted points.

3.1.2 Supervised Calibration Routine

For applications where the calibration accuracy is critical, the supervised calibration acts as a fail-safe for the unsupervised routine by actively verifying every solution. Using a closed-loop topology, it uses the "adaptive kernel search" algorithm to ensure each point meets specified validation criteria, as shown in Fig. 3.4.

Operating on a point-to-point basis, the supervised routine begins with initial gain and phase indexes from the control code solver, which are used as first guesses for the adaptive kernel search algorithm. These indexes are applied to the VGPS/array elements, and the resulting measurements are checked against validation criteria. Depending on the convergence progress, the batch of requested points can contain more than one position.

If the current batch meets the validation criteria, the point closest to the ideal target is selected and its code is stored. If the batch fails, new positions are calculated through "position compensation" and re-measured, aiming for higher validation success. If convergence fails, the batch size increases through "kernel size expansion" to search a larger area.

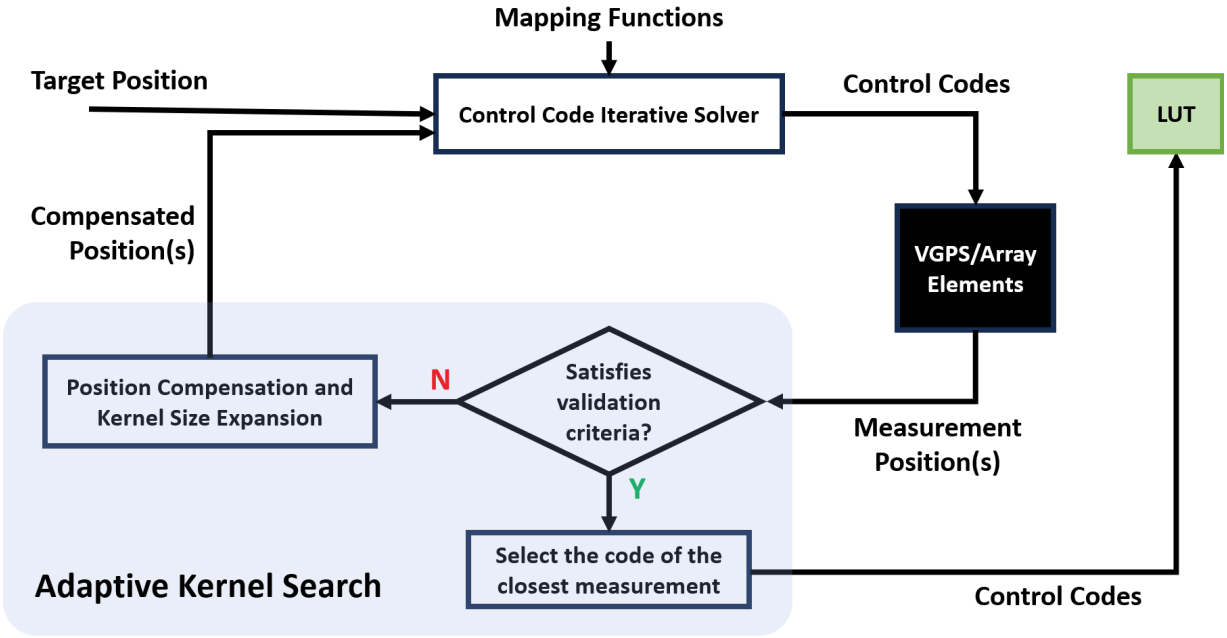


Figure 3.4: Flow diagram of the proposed supervised calibration routine.

This routine guarantees calibration performance despite imperfect VGPS characterization, reducing measurements compared to the exhaustive search by focusing on points near the targets. Accurate characterization minimizes searching iterations by producing measurements close to ideal positions.

For supervised calibration routine only, after calibration, the algorithm performs "Post-Calibration Optimization," using the exhaustive search method on the acquired data to find potentially better solutions for each target position. While rare, this optimization can improve the error vector magnitude (EVM) of the calibrated constellation, especially for larger numbers of target points.

3.2 Fast Constellation Characterization Method

3.2.1 Strategy

According to the varying error model, the error changes for different combinations of the control inputs. As shown in the figure 3.5 below, which shows the measurement of a commercially available BFIC, a typical VGPS response shows several control non-idealities. Namely, the gain and phase are not linearly proportional to their control codes and there are inter-dependencies between them.

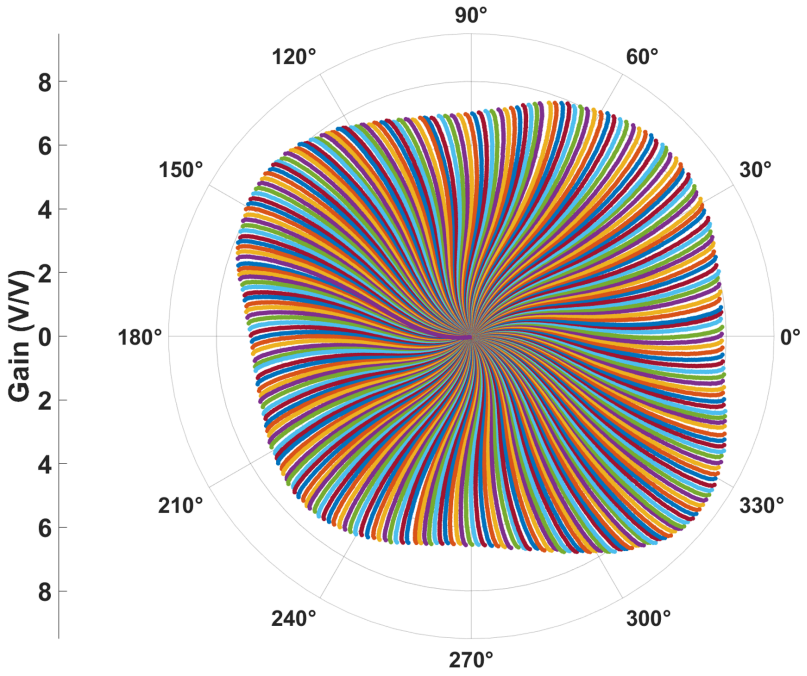


Figure 3.5: BFIC1 measurement.

The control sampling method used in the industry [32] isolates the gain and phase control errors and samples the gain and phase control relationships (referred to as "gain profile" and "phase profile" respectively). The control relationships are sampled by fixing one index while sweeping the other and are then statically applied for all regions of the constellation for solutions of the desired constellation. A solution can then be found by interpolating the sampled series.

This method, however, has huge limitations. Since the sampled gain and phase control relationships do not stay constant over the entire VGPS constellation (demonstrated in figure 3.7), the solved gain and phase indexes would be less accurate as the solver targets a point further away from where in the constellation the gain and phase profiles are measured.

This regionality of the accuracy of the characterization is demonstrated in the example calibration of the BFIC1 shown in figure 3.6. The example calibration result in figure 3.6b shows that, even with the gain-to-phase variation compensation technique proposed in later sections of the thesis, the calibration accuracy is highly regional and depends on where in the constellation the sampling is made. Since the gain and phase are coupled together, meaning changing the gain would also change the phase and vice versa, the solution is only accurate when solving the intersection of the gain profile and phase profile as demonstrated in figure 3.6b. As the solver targets areas of the constellation further away from this intersection, the calibration becomes less accurate. Improvement can be realized if the sampling is done for multiple sections of the constellation and using denser points. However, this would result in the number of measurements quickly approaching that of the exhaustive search method as the algorithm targets for lower phase and gain error across the entire VGPS constellation.

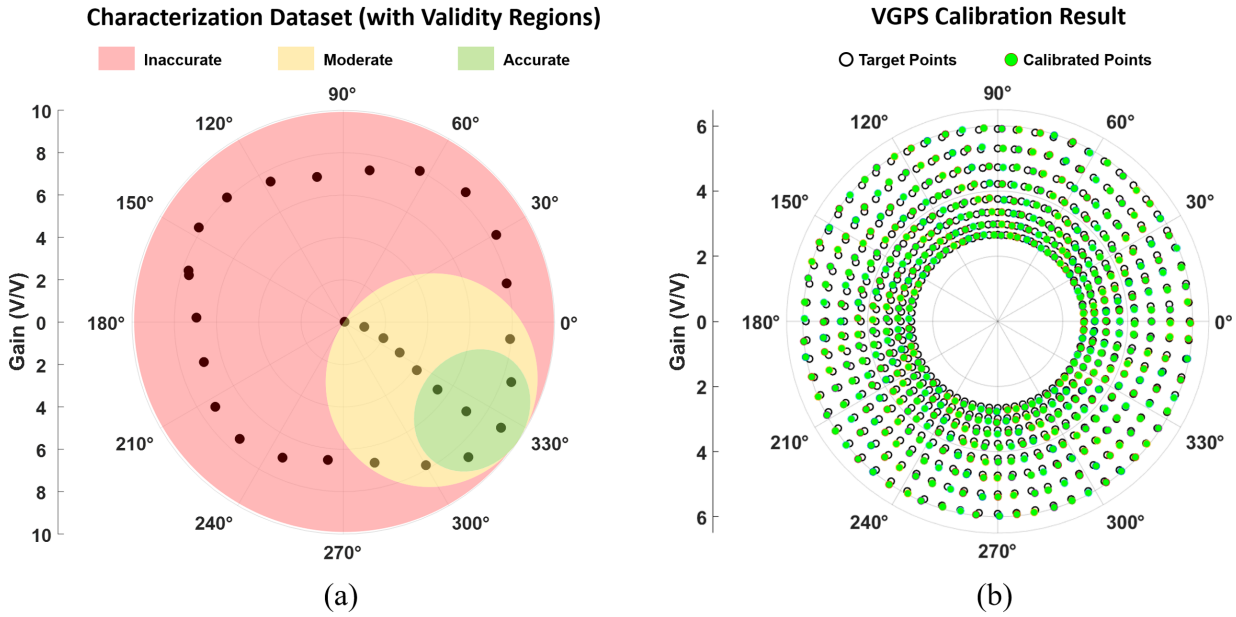
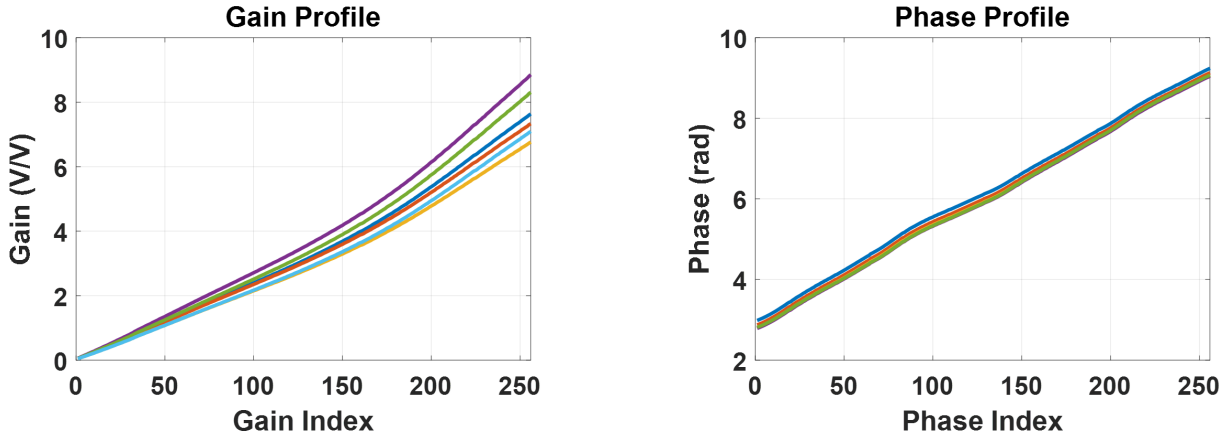


Figure 3.6: Example calibration method demonstrating the regionality of the characterization dataset. Calibrated on the BFIC1 targeting 6-bit phase and 8 gain states: (a) example characterization dataset; (b) corresponding calibration result.



(a) (b)

Figure 3.7: Example gain and phase profiles of the BFIC1 (incomplete set): (a) gain profiles; (b) phase profiles.

Our strategy is to explore the possibility that, as observed from our testing shown in figure 3.7, the variation of the gain and phase profile across different regions of the constellation could be modeled. To address the control relationship variations, a minimal and optimal set of sampling points, referred to as the "Characterization Dataset," is identified to capture necessary variations. Using the proposed sampling scheme along the gain and phase axes, as depicted in Fig. 3.8, the two parallel series along the two polar directions reveal how each series varies across the two directions. The comprehensive two-dimensional control relationship is extracted and described using eleven "Mapping Functions" which are solved in an iterative solver for the desired constellation. By adjusting the gain and phase control relationships according to the captured model, the manipulated gain and phase controls intersect at the constellation positions of interest, thus providing an accurate solution.

3.2.2 Overview

The proposed characterization is done through the acquisition of the "Characterization Dataset" and the generation of the "Mapping Functions" as described in the flow chart in Figure 3.9. The characterization dataset is acquired by measuring the VGPS on several series of control codes that enable the VGPS to show its response over its inputs. The "main" dataset captures the control relationship while the "auxiliary" dataset captures how

this control relationship translates across the constellation. The characterization dataset consists of four steams of data:

- Outline Data (OD)
- Auxiliary Outline Data (AOD)
- Gain Data (GD)
- Auxiliary Gain Data (AGD)

and they are demonstrated in figure 3.8 and figure 3.10 for the characterization of the BFIC1.

From the characterization dataset, eleven mapping functions are calculated which describe the effects of changing the VGPS gain and phase indexes on different characteristics of its response. The eleven mapping functions include four main mapping functions that describe the VGPS control relationships:

- Gain Profile (GP)
- Phase Profile (PP)
- Gain Envelope (GE)
- Gain-to-Phase Variation ($G2\Delta\theta$)

four auxiliary mapping functions that help to enhance the accuracy and general applicability of the main mapping functions across all regions of the constellation:

- Auxiliary Gain Profile (AGP)
- Auxiliary Phase Profile (APP)
- Auxiliary Gain Envelope (AGE)
- Auxiliary Gain-to-Phase Variation ($AG2\Delta\theta$)

and three composite mapping functions (derived from other mapping functions) to help with the decision-making of the algorithm and the smooth translation of function shapes across different regions of the constellation:

- Gain Envelope Scaling Profile ($GESP$)
- Gain Profile Scaling Profile ($GPSP$)
- Phase Profile Shifting Profile ($PPSP$)

Once the characterization finishes, the eleven mapping functions are used in an iterative solver which solves the gain and phase indexes for a given target gain and target phase, as illustrated in the unsupervised and supervised calibration routines in Fig. 3.3 and Fig. 3.4 respectively.

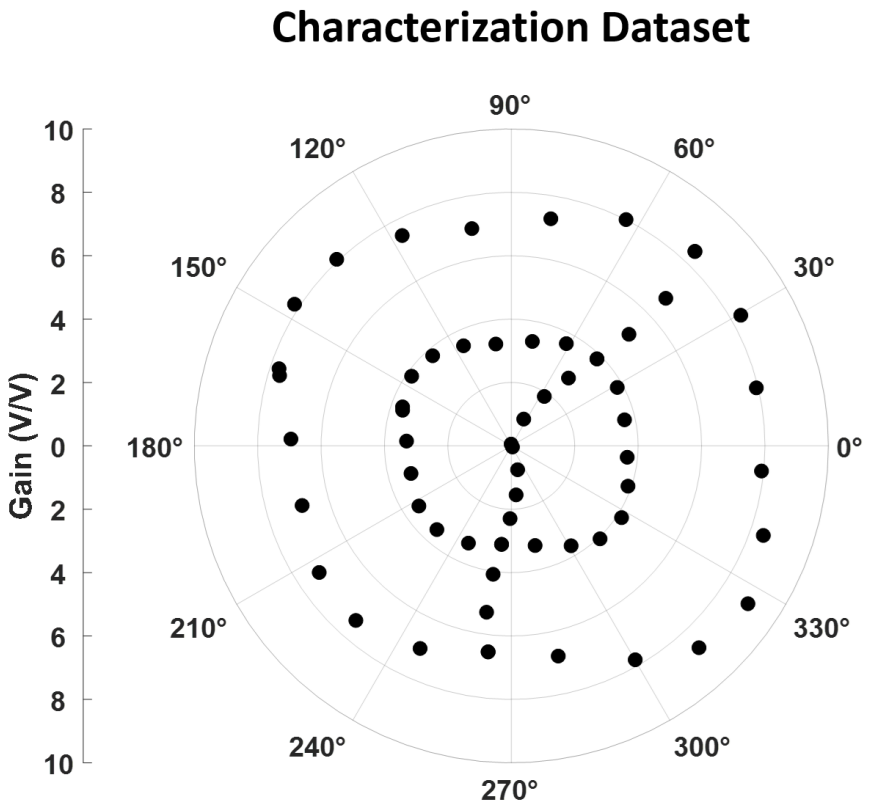


Figure 3.8: Characterization Dataset for BFIC1. Sampled with outline data sampling size of 23 and gain data sampling size of 8.

Figure 3.9 below shows the flow of the characterization process. Due to its progressive nature, the algorithm needs to receive the main and auxiliary outline data before it can decide where to measure the main and auxiliary gain data.

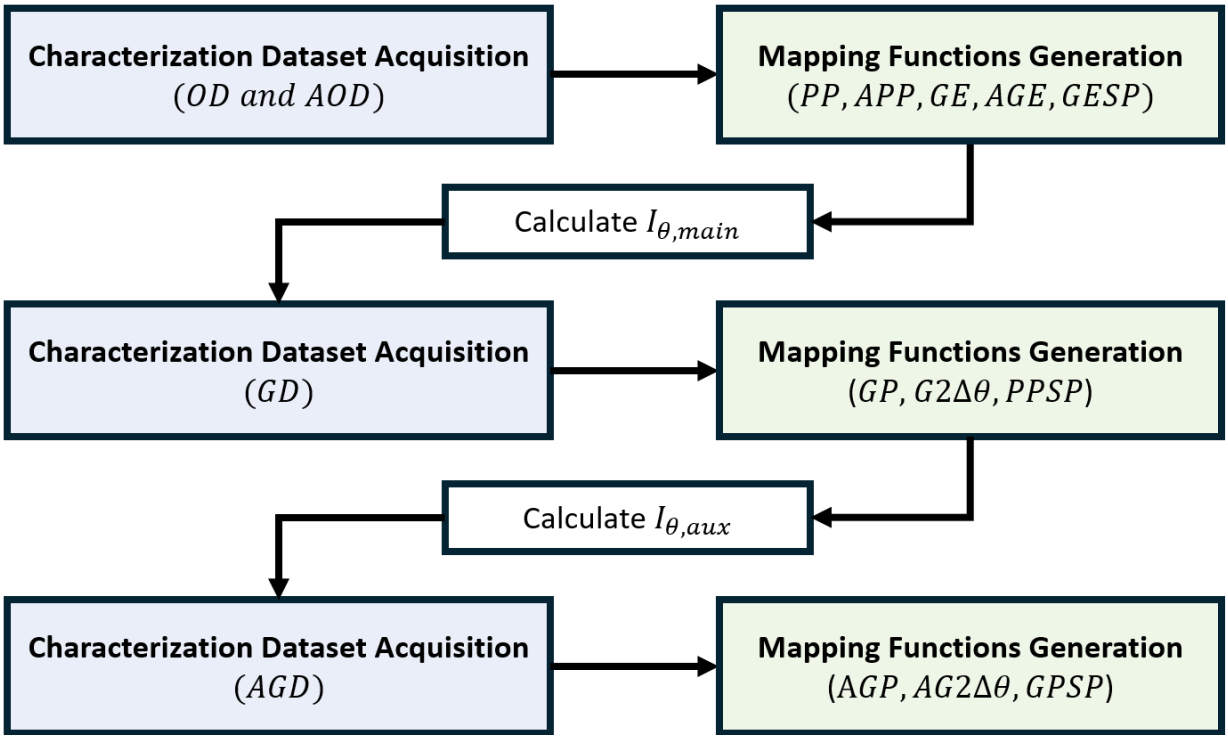


Figure 3.9: Flow diagram of the proposed VGPS constellation characterization process.

The acquisition of the characterization dataset, the generation of the mapping functions and the control code iterative solver are discussed in detail below. Additionally, notes on the selection of the optimum sampling indexes, optimum sampling size and the setting of targeting gains are also included.

3.2.3 Characterization Dataset Acquisition

The characterization dataset is acquired through selective measurements on the VGPS and the sampling size should be set for the best trade-off between the number of measurements and the accuracy of the characterization. We have defined a figure-of-merit (FOM) for identifying and choosing the optimum sampling size and it is shown in figure 3.23 in section 3.2.7 below.

The proposed characterization method does not make assumption on the sampling indexes. However, the selection of optimal sampling indexes is critical for the most accurate and consistent characterization performance. The process of selecting the optimal sampling

indexes will be discussed in detail later in the thesis. For the purposes of the following section, we assume that these sampling indexes have already been pre-selected and the characterization flow follows the top-level flow chart in figure 3.2.

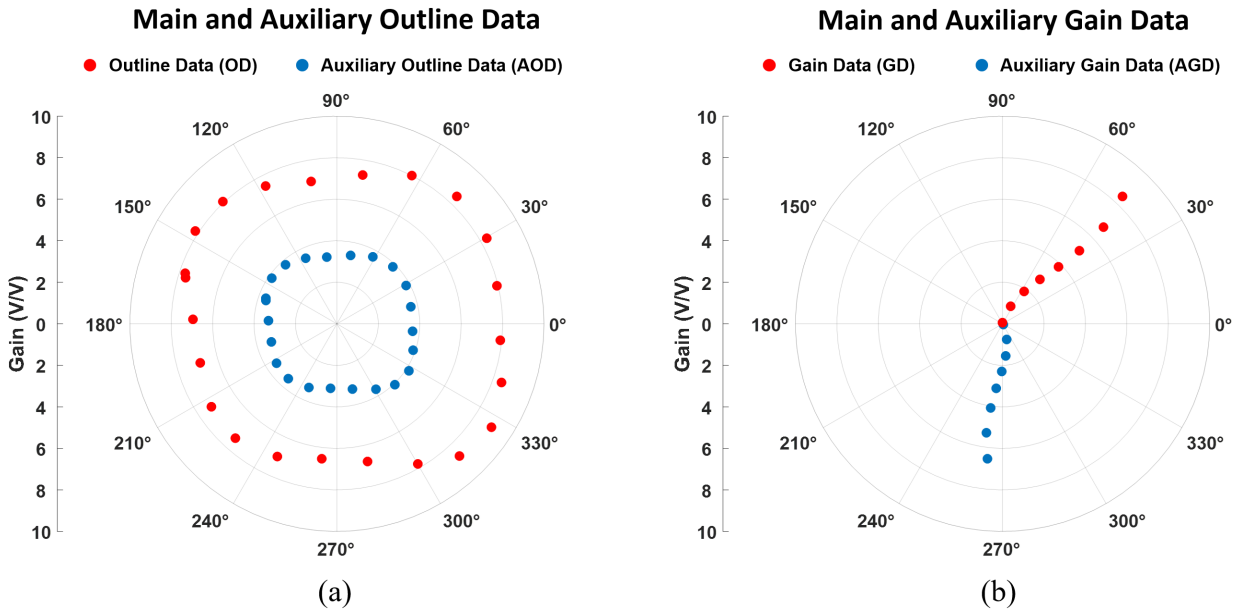


Figure 3.10: Characterization Dataset: (a) main and auxiliary outline data; (b) main and auxiliary gain data.

Outline Data Acquisition

The main and auxiliary outline data, illustrated in figure 3.10a above, are acquired from a series of measurements as described below:

$$OD(I_\theta) = M_{I_{G,main},I_\theta}, \quad for\ I_\theta \in \{I_{\theta,min}, ..., I_{\theta,max}\} \tag{3.1}$$

$$AOD(I_\theta) = M_{I_{G,aux},I_\theta}, \quad for\ I_\theta \in \{I_{\theta,min}, ..., I_{\theta,max}\} \tag{3.2}$$

where I_θ is the sweeping phase index, $I_{G,main}$ is the main gain index along which the main outline data are acquired, $I_{G,aux}$ is the auxiliary gain index along which the auxiliary outline data are acquired, M_{I_G,I_θ} denotes the complex transmission coefficient from measuring the gain index I_G and phase index I_θ, $I_{\theta,min}$ is the minimum phase index of the device and $I_{\theta,max}$ is the maximum phase index of the device.

For capturing maximum gain along each phase direction and to determine the targeting gain states of the device, $I_{G,main}$ is selected to be the maximum gain index of the device $I_{G,max}$:

$$I_{G,main} = I_{G,max} \tag{3.3}$$

Gain Data Acquisition

The main and auxiliary gain data, illustrated in figure 3.10b above, are acquired from a series of measurements as described below:

$$GD(I_G) = M_{I_G,I_{\theta,main}}, \quad for\ I_G \in \{I_{G,min}, ..., I_{G,max}\} \tag{3.4}$$

$$AGD(I_G) = M_{I_G,I_{\theta,aux}}, \quad for\ I_G \in \{I_{G,min}, ..., I_{G,max}\} \tag{3.5}$$

where I_G is the sweeping gain index, $I_{\theta,main}$ is the main phase index along which the main gain data are acquired, $I_{\theta,aux}$ is the auxiliary phase index along which the auxiliary gain data are acquired, $I_{G,min}$ is the minimum gain index of the device and $I_{G,max}$ is the maximum gain index of the device.

To achieve the highest characterization accuracy, it is essential to optimize $I_{G,aux}$, $I_{\theta,main}$ and $I_{\theta,aux}$ to extract maximum information from the constellation. The process of selecting the optimal sampling indexes will be discussed in detail later in the thesis.

3.2.4 Mapping Functions Generation

In this section, we will thoroughly define the eleven mapping functions and discuss the rationale behind their use by the solver.

Gain Profile

The gain profile captures the control relationship between the measured VGPS gain and the VGPS gain index. An auxiliary gain profile is defined to capture how the main gain profile changes its function shape across different phase indexes. The main and auxiliary gain profiles, demonstrated in figure 3.11, are defined as:

$$GP(I_G) = |GD(I_G)| \tag{3.6}$$

$$AGP(I_G) = |AGD(I_G)| \tag{3.7}$$

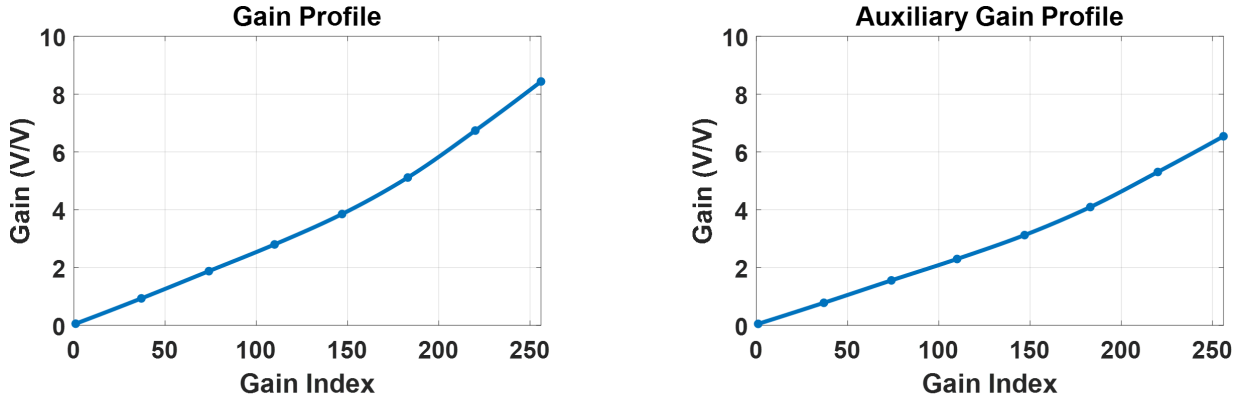


Figure 3.11: Main and auxiliary gain profile sampled from BFIC1 using a gain data sampling size of 8. Solid dots represent discrete measurement data points. Interpolated for the entire gain index range using the shape-preserving piecewise cubic interpolation method: (a) gain profile, $I_{\theta,main} = 175$; (b) auxiliary gain profile, $I_{\theta,aux} = 71$.

As demonstrated in figure 3.11, we can observe that the gain profiles at different phase indexes differ primarily by a scaling factor, while the overall shape of the gain profile is preserved across these directions.

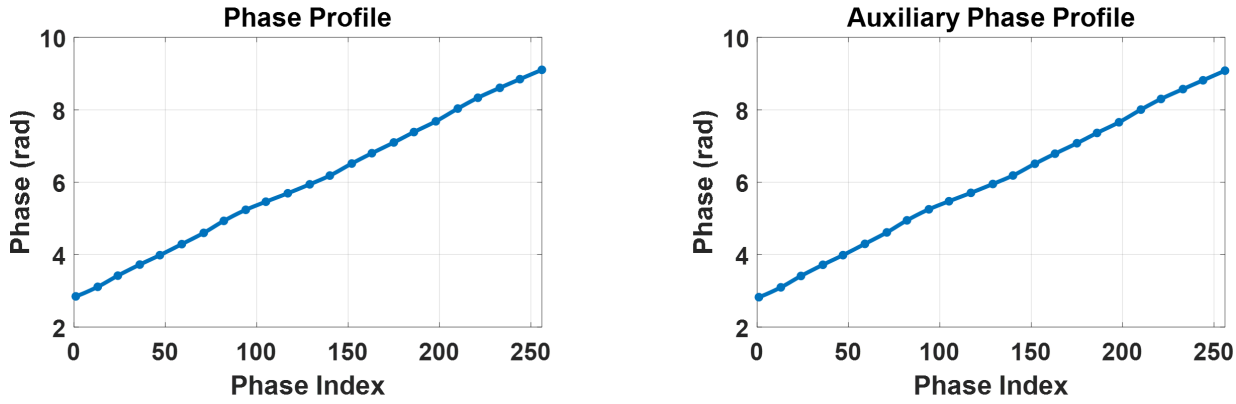
Phase Profile

The phase profile captures the control relationship between the measured VGPS phase and the VGPS phase index. An auxiliary phase profile is defined to capture how the main phase profile changes in function shape across different gain indexes. The main and auxiliary phase profiles, demonstrated in figure 3.12, are defined as:

$$PP(I_\theta) = phase(OD(I_\theta)) = tan^{-1}\left(\frac{imag(OD(I_\theta)}{real(OD(I_\theta)}\right) \tag{3.8}$$

$$APP(I_\theta) = phase(AOD(I_\theta)) = tan^{-1}\left(\frac{imag(AOD(I_\theta)}{real(AOD(I_\theta)}\right) \tag{3.9}$$

As demonstrated in figure 3.12, we can observe that the phase profiles at different gain indexes differ primarily by an offset, while the overall shape of the phase profile is preserved across these gains.



(a) (b)

Figure 3.12: Main and auxiliary phase profile sampled from BFIC1 using an outline data sampling size of 23. Solid dots represent discrete measurement data points. Interpolated for the entire phase index range using the modified Akima piecewise cubic Hermite interpolation method: (a) phase profile, $I_{G,main} = 256$; (b) auxiliary phase profile, $I_{G,aux} = 147$.

Gain Envelope

The gain envelope captures how the maximum gain changes for different phase indexes and it guides the scaling of the main gain profile when adjusting for different phase index directions. An auxiliary gain envelope is defined to capture how the gain envelope changes shape across different gain indexes. The main and auxiliary gain envelopes, demonstrated in figure 3.13, are defined as:

$$GE(I_\theta) = |OD(I_\theta)| \tag{3.10}$$

$$AGE(I_\theta) = |AOD(I_\theta)| \tag{3.11}$$

Since the main gain envelope represents the maximum gain at each phase index, the peak values on the gain profiles shown in figure 3.11 should correspond to the values on the main gain envelope for each respective phase index.

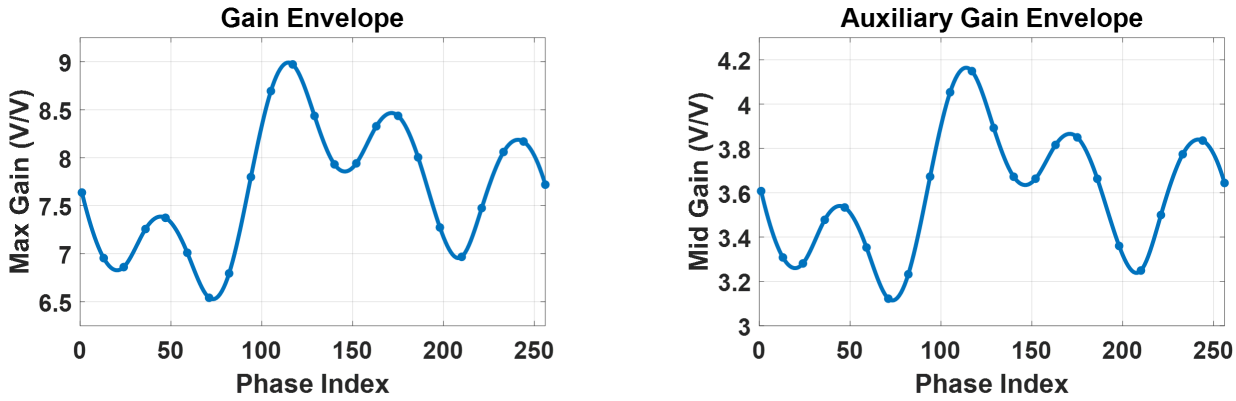


Figure 3.13: Main and auxiliary gain envelope sampled from BFIC1 using an outline data sampling size of 23. Solid dots represent discrete measurement data points. Interpolated for the entire phase index range using the cubic spline interpolation method: (a) gain envelope, $I_{G,main} = 256$; (b) auxiliary gain envelope, $I_{G,aux} = 147$.

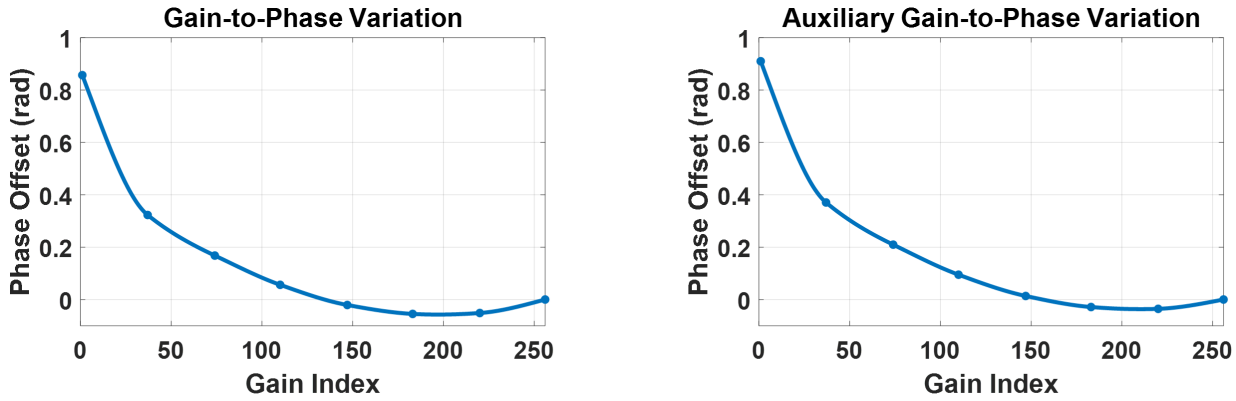
Gain-to-Phase Variation

The gain-to-phase variation captures how the relative phase changes as the gain index changes. An auxiliary gain-to-phase variation is defined to capture how the gain-to-phase variation changes shape across different phase indexes. The main and auxiliary gain-to-phase variation, shown in figure 3.14, are defined as:

$$G2\Delta\theta(I_G) = phase(GD(I_G)) - phase(GD(I_{G,main})) \tag{3.12}$$

$$AG2\Delta\theta(I_G) = phase(AGD(I_G)) - phase(AGD(I_{G,main})) \tag{3.13}$$

The solver uses the relative phase offset provided by the gain-to-phase variation mapping function to shift the phase profile to adjust for the phase variation as the VGPS changes its gain. Since the main phase profile is taken at the maximum gain index, the values on the gain-to-phase variation need to be relative to the phase on the maximum gain index.



(a) (b)

Figure 3.14: Main and auxiliary gain-to-phase variation sampled from BFIC1 using a gain data sampling size of 8. Solid dots represent discrete measurement data points. Interpolated for the entire gain index range using the modified Akima piecewise cubic Hermite interpolation method: (a) gain-to-phase variation, $I_{\theta,main} = 175$; (b) auxiliary gain-to-phase variation, $I_{\theta,aux} = 71$.

Gain Envelope Scaling Profile

The gain envelope scaling profile captures the gain scaling factor from the maximum gain to the auxiliary gain at each phase index. It is defined as follows:

$$GESP(I_\theta) = \frac{AGE(I_\theta)}{GE(I_\theta)} \tag{3.14}$$

Figure 3.15 below shows the gain envelope scaling profile of the BFIC1. We observe that the scaling factor from the maximum gain to the auxiliary gain (near middle) is changing versus the phase index. This profile indicates the effect of relative gain expansion and compression of the gain data at different phase indexes. The gain data at phase indexes near the peak of the $GESP$ show the highest gain compression compared to the mean, while the gain data at phase indexes near the bottom exhibit the highest relative gain expansion.

The $GESP$ provides insight into how the gain profile shape changes across phase indexes. Moving from a phase index near the peak of the $GESP$ to a phase index near the bottom of the $GESP$ results in the gain profile sinking in its middle. Figure 3.16 below demonstrates this phenomenon. Using the BFIC1 as the example, the normalized

gain profile at phase index 47, the peak of $GESP$, has its middle values higher than the normalized gain profile at phase index 175, the bottom of $GESP$. This effect is subtle but its capture is crucial to ensure maximum accuracy.

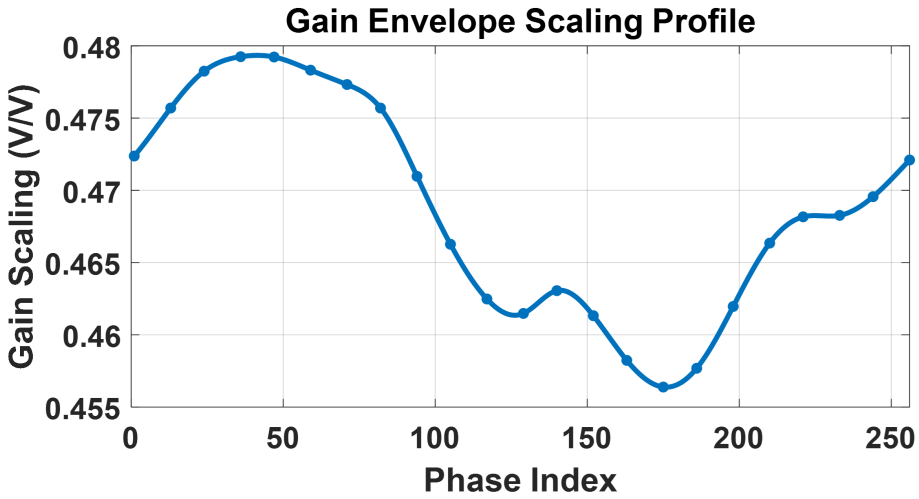


Figure 3.15: Gain Envelope Scaling Profile sampled from BFIC1 using a gain data sampling size of 8, $I_{G,main} = 256$, $I_{G,aux} = 147$. Solid dots represent discrete measurement data points. Interpolated for the entire gain index range using the cubic spline interpolation method.

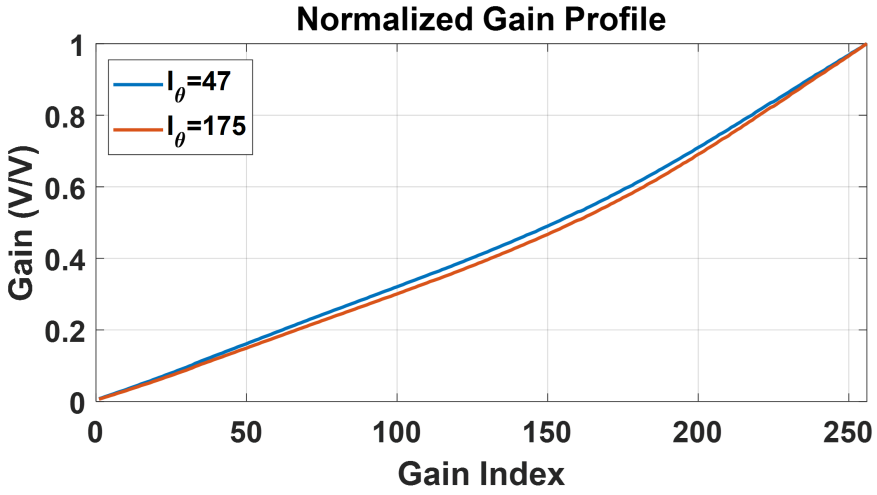


Figure 3.16: Normalized gain profiles sampled from BFIC1 at phase indexes 47 and 175 to demonstrate the shape change.

If the main and auxiliary gain profiles have the two extreme shapes (orange and blue curves in figure 3.16), then the other possible gain profiles in other phase indexes will have a normalized shape that fits in between thus allowing for accurate interpolation.

Gain Profile Scaling Profile

To capture how the normalized shape of the gain profile changes across different phase indexes, the gain profile scaling profile is defined as the normalized element-wise division between the auxiliary gain profile and the main gain profile:

$$GPSP(I_G) = \frac{AGP(I_G)}{GP(I_G)} \cdot \frac{GE(I_{\theta,main})}{GE(I_{\theta,aux})} \tag{3.15}$$

Notice that from the definition, the gain profile scaling profile is normalized to the gain scaling factor on the maximum gain index so that the gain profile scaling profile has a value of "1" on the maximum gain index as shown in figure 3.17 below.

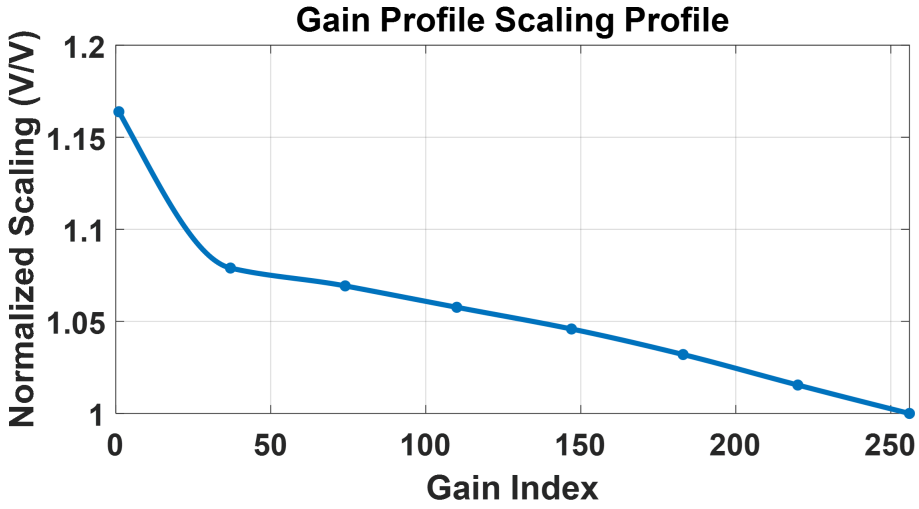


Figure 3.17: Gain Profile Scaling Profile sampled from BFIC1 using a gain data sampling size of 8, $I_{\theta,main} = 175$, $I_{\theta,aux} = 71$. Solid dots represent discrete measurement data points. Interpolated for the entire gain index range using the modified Akima piecewise cubic Hermite interpolation method.

An important detail, as suggested by the definition in (3.15), is that the captured $GPSP$ changes depending on the choices of the $I_{\theta,main}$ and $I_{\theta,aux}$. The general definition

of the gain profile scaling profile incorporating any values of the main and auxiliary phase indexes is:

$$GPSP(I_G) = \frac{|M_{I_G,I_{\theta,aux}}|}{|M_{I_G,I_{\theta,main}}|} \cdot \frac{|M_{I_{G,max},I_{\theta,main}}|}{|M_{I_{G,max},I_{\theta,aux}}|}, \quad for\ I_G \in \{I_{G,min}, ..., I_{G,max}\} \tag{3.16}$$

Using the equation in (3.16), figure 3.18 below confirms the change of the gain profile scaling profile in the general definition as we change the auxiliary phase index while fixing the main phase index. For maximum accuracy, $I_{\theta,\text{main}}$ and $I_{\theta,\text{aux}}$ need to be chosen such that the resulting $GPSP$ is well-defined.

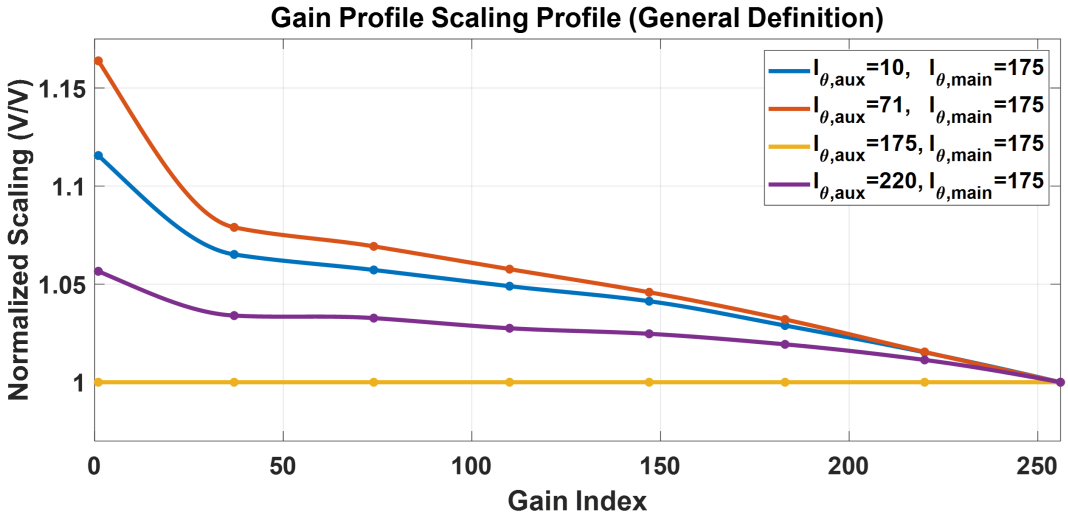


Figure 3.18: General Gain Profile Scaling Profile for different auxiliary phase indexes. Sampled from BFIC1 using a gain data sampling size of 8. Solid dots represent discrete measurement data points. Interpolated for the entire gain index range using the modified Akima piecewise cubic Hermite interpolation method.

Phase Profile Shifting Profile

To capture how the normalized shape of the phase profile changes across different gain indexes, the phase profile shifting profile is defined as the normalized element-wise difference between the auxiliary phase profile and the main phase profile:

$$PPSP(I_\theta) = APP(I_\theta) - PP(I_\theta) - G2\Delta\theta(I_{G,aux}) \tag{3.17}$$

Similar to the $GPSP$, the captured $PPSP$ varies with different selections of $I_{G,main}$ and $I_{G,aux}$. The general definition of the phase profile shifting profile incorporating any values of the main and auxiliary gain indexes is:

$$PPSP(I_\theta) = phase(M_{I_{G,aux},I_\theta}) - phase(M_{I_{G,main},I_\theta}) \\ - (phase(M_{I_{G,aux},I_{\theta,main}}) - phase(M_{I_{G,main},I_{\theta,main}})),\ for\ I_\theta \in \{I_{\theta,min}, \ldots, I_{\theta,max}\} \tag{3.18}$$

To determine the maximum targeting gain states, $I_{G,main}$ is fixed at $I_{G,max}$. Therefore, the choice of $I_{G,aux}$ becomes crucial for capturing a well-defined $PPSP$. Using the equation in (3.18), figure 3.20 explores how the different choices of the auxiliary gain index $I_{G,aux}$ would impact the shape of the phase profile shifting profile with the main gain index $I_{G,main}$ fixed at 256. For maximum accuracy, $I_{G,aux}$ needs to be chosen such that the resulting $PPSP$ is well-defined.

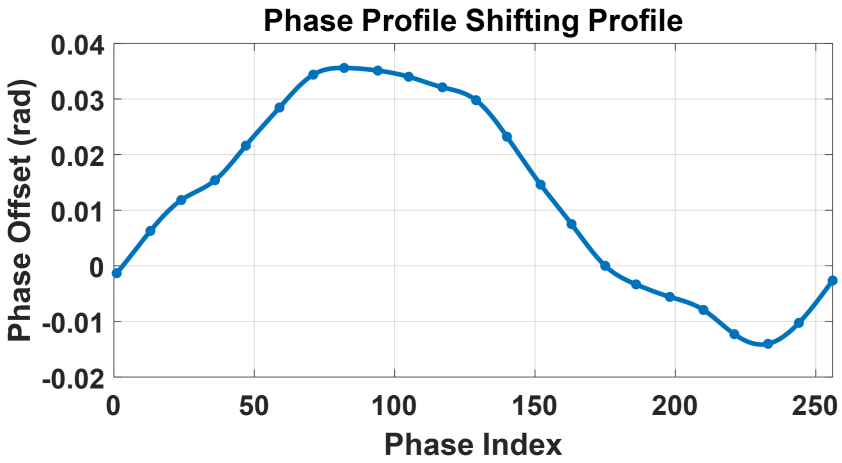


Figure 3.19: Phase Profile Shifting Profile sampled from BFIC1 using an outline data sampling size of 23, $I_{G,main} = 256$, $I_{G,aux} = 147$. Solid dots represent discrete data points. Interpolated for the entire phase index range using the cubic spline interpolation method.

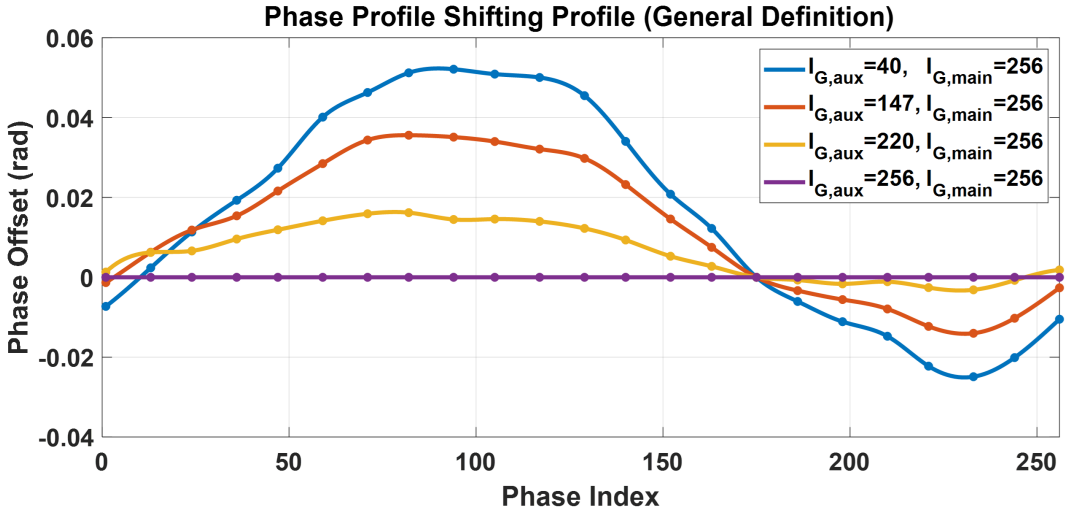


Figure 3.20: General Phase Profile Shifting Profile for different auxiliary gain indexes. Sampled from BFIC1 using an outline data sampling size of 23. Solid dots are discrete data points. Interpolated for the entire phase index range using the cubic spline method.

3.2.5 Control Code Iterative Solver

Due to the inter-dependencies of gain and phase control states as described by the mapping functions shown in section 3.2.4, deriving a closed-form solution for the gain and phase indices is not feasible. Instead, the solver takes an iterative approach to generate a gain and phase index solution for a target gain and phase. After several iterations, the solution for gain and phase indexes settles and the final solution satisfies all eleven mapping functions.

The gain and phase profiles need to intersect at the constellation positions of interest for the solutions to be accurate. Thus, the solver needs to adjust the captured gain and phase profiles by scaling, shifting and shape modification so that they would appear to be captured at the position of interest. From the definitions of the mapping functions in section 3.2.4 above, the adjusted gain profile ($\widetilde{GP}$) and the adjusted phase profile ($\widetilde{PP}$) would take on the following format:

$$\widetilde{GP}(I_G) = GP(I_G) \cdot \frac{GE(I_\theta)}{GE(I_{\theta,main})} \cdot \widetilde{GPSP}(I_G) \tag{3.19}$$

$$\widetilde{PP}(I_\theta) = PP(I_\theta) + G2\Delta\theta(I_G) + \widetilde{PPSP}(I_\theta) \tag{3.20}$$

where $\widetilde{GPSP}$ and $\widetilde{PPSP}$ are the adjusted gain profile scaling profile and the adjusted phase profile shifting profile respectively. We confirm from the two equations above that they are coupled together thus the iterative approach.

With a target phase (θ_t) and target gain (G_t), the unsettled gain index and phase index solutions symbolised by I'_G and I'_θ are calculated and improved iteratively. The solver starts by omitting the gain index dependency on the phase profile. A first guess on the phase index is calculated as:

$$I'_\theta = PP^{-1}(\theta_t) \tag{3.21}$$

Note that the operation in the above equation involves inverting the mapping function and interpolation.

Addressing the changing shape of the $GPSP$, the next step is to adjust the $GPSP$ so that it would appear to be captured with an $I_{\theta,aux}$ equal to the phase index first guess I'_θ. From its definition in (3.15), the adjusted gain profile scaling profile at the auxiliary gain index $I_{G,aux}$ is:

$$\widetilde{GPSP}(I_{G,aux}) = \frac{\widetilde{AGP}(I_{G,aux})}{GP(I_{G,aux})} \cdot \frac{GE(I_{\theta,main})}{GE(I'_\theta)} \tag{3.22}$$

where the $\widetilde{AGP}$ is the adjusted auxiliary gain profile at I'_θ. Since we only care about the $\widetilde{AGP}$ at $I_{G,aux}$, we can replace it with the auxiliary gain envelope AGE:

$$\widetilde{GPSP}(I_{G,aux}) = \frac{AGE(I'_\theta)}{AGE(I_{\theta,main})} \cdot \frac{GE(I_{\theta,main})}{GE(I'_\theta)} \tag{3.23}$$

The above equation can then be rearranged to utilize the gain envelope scaling profile:

$$\begin{aligned} GPSP_{adj}(I_{G,aux}) &= \frac{AGE(I'_\theta)}{AGE(I_{\theta,main})} \cdot \frac{GE(I_{\theta,main})}{GE(I'_\theta)} \\ &= \frac{AGE(I'_\theta)}{GE(I'_\theta)} \div \frac{AGE(I_{\theta,main})}{GE(I'_\theta)} \\ &= \frac{GESP(I'_\theta)}{GESP(I_{\theta,main})} \end{aligned} \tag{3.24}$$

With the solved "true" value at the $I_{G,aux}$ (referred to as an "Observation"), we then scale the $GPSP$ about the baseline of "1" so that it would cross the observation at the $I_{G,aux}$:

$$\widetilde{GPSP}(I_G) = \frac{\widetilde{GPSP}(I_{G,aux}) - 1}{GPSP(I_{G,aux}) - 1} \cdot \Big(GPSP(I_G) - 1\Big) + 1 \tag{3.25}$$

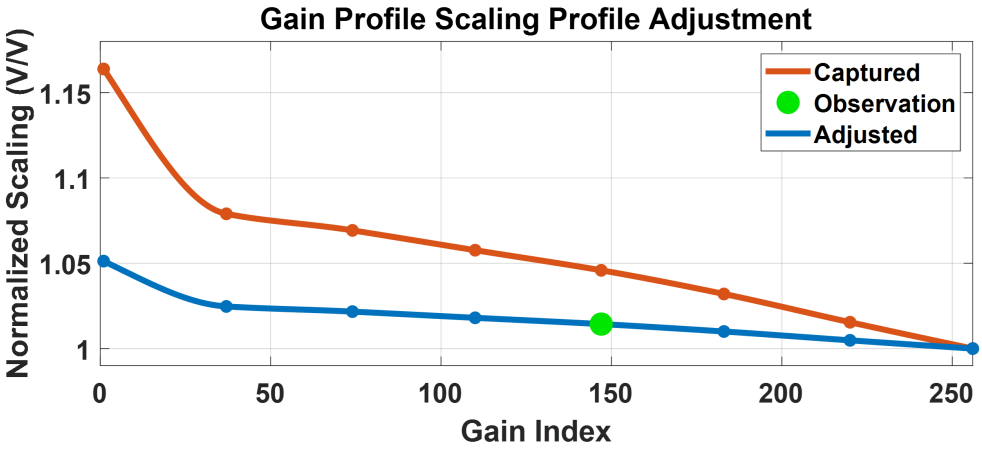


Figure 3.21: Example adjustment of Gain Profile Scaling Profile using an observation at the auxiliary gain index of 147.

Figure 3.21 shows an example of such adjustment. As demonstrated, the $\widetilde{GPSP}$ retains the original shape and crosses the observed value at the auxiliary gain index.

Then using the $\widetilde{GPSP}$, the adjusted gain profile $\widetilde{GP}$ is calculated as:

$$\widetilde{GP}(I_G) = GP(I_G) \cdot \frac{GE(I'_\theta)}{GE(I_{\theta,main})} \cdot \widetilde{GPSP}(I_G) \tag{3.26}$$

As described in (3.26) above, the gain profile is scaled using the ratio of maximum gains described in the gain envelope and then shape-modified using the adjusted gain profile scaling profile. Note that the adjusted gain profile will have the "correct" value at the $I_{G,aux}$ due to the observation at this index in the adjusted gain profile scaling profile.

Finally, a first guess on the gain index is calculated as:

$$I'_G = \widetilde{GP}^{-1}(G_t) \tag{3.27}$$

Now, using the gain and phase indexes first guess (I'_G, I'_θ), a more accurate solution can be found by also solving for the phase offset at the solved gain index.

Addressing the changing shape of the $PPSP$, it needs to be adjusted so that it would appear to be captured with an $I_{G,aux}$ equal to the gain index first guess I'_G. From its definition, the adjusted phase profile shifting profile at the $I_{G,aux}$ is:

$$\widetilde{PPSP}(I_{\theta,aux}) = \widetilde{APP}(I_{\theta,aux}) - PP(I_{\theta,aux}) - G2\Delta\theta(I'_G) \tag{3.28}$$

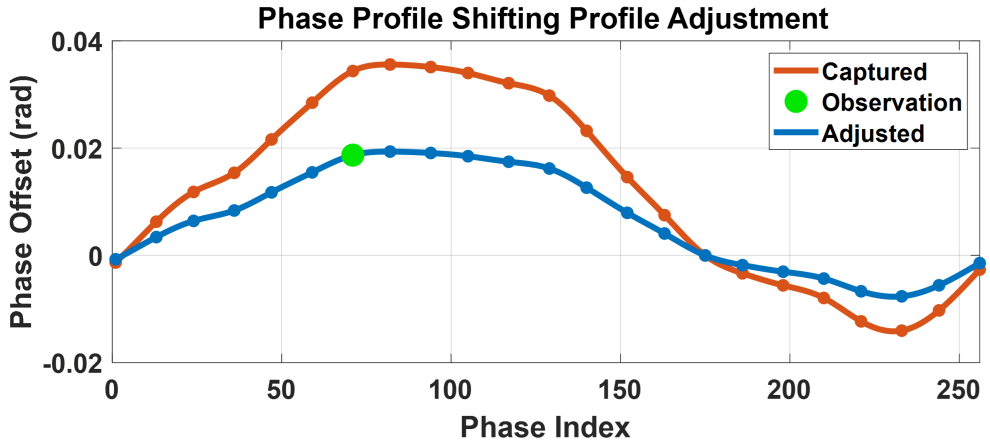


Figure 3.22: Example adjustment of Phase Profile Shifting Profile using an observation at the auxiliary phase index of 71.

where the $\widetilde{APP}$ is the adjusted auxiliary phase profile at I'_G. Since we only care about the $\widetilde{APP}$ at $I_{\theta,aux}$, we can replace it with the auxiliary gain-to-phase variation $AG2\Delta\theta$:

$$\begin{aligned} PPSP_{adj}(I_{\theta,aux}) &= APP_{adj}(I_{\theta,aux}) - PP(I_{\theta,aux}) - G2\Delta\theta(I'_G) \\ &= (AG2\Delta\theta(I'_G) + PP(I_{\theta,aux})) - PP(I_{\theta,aux}) - G2\Delta\theta(I'_G) \\ &= AG2\Delta\theta(I'_G) - G2\Delta\theta(I'_G) \end{aligned} \tag{3.29}$$

With the observation at the $I_{\theta,aux}$, we then scale the $PPSP$ about the baseline of "0" so that it would cross the observation at the $I_{\theta,aux}$:

$$\widetilde{PPSP}(I_\theta) = \frac{\widetilde{PPSP}(I_{\theta,aux})}{PPSP(I_{\theta,aux})} \cdot PPSP(I_\theta) \tag{3.30}$$

Figure 3.22 shows an example of such adjustment. As demonstrated, the adjusted phase profile shifting profile retains the original shape and crosses the observed value at the $I_{\theta,aux}$.

Using the $\widetilde{PPSP}$, the adjusted phase profile $\widetilde{PP}$ is calculated:

$$\widetilde{PP}(I_\theta) = PP(I_\theta) + G2\Delta\theta(I'_G) + \widetilde{PPSP}(I_\theta) \tag{3.31}$$

As described in (3.31) above, the captured phase profile is shifted using the phase offset from the maximum gain described in the gain-to-phase variation and then shape-modified

using the adjusted phase profile shifting profile. Note that the adjusted phase profile will have the "correct" value at the auxiliary phase index due to the observation at this index in the adjusted phase profile shifting profile.

With the adjusted phase profile, an improved solution of the phase index can be found:

$$I'_\theta = \widetilde{PP}^{-1}(\theta_t) \tag{3.32}$$

Now, with the improved solution of the phase index, the algorithm goes back to (3.24) to solve for a better gain index.

Putting the iterative solver together and omitting the intermediate steps, the steps are stated as follows:

$$I'_\theta = PP^{-1}(\theta_t) \tag{3.33}$$

$$\widetilde{GPSP}(I_{G,aux}) = \frac{GESP(I'_\theta)}{GESP(I_{\theta,main})} \tag{3.34}$$

$$\widetilde{GPSP}(I_G) = \frac{\widetilde{GPSP}(I_{G,aux}) - 1}{GPSP(I_{G,aux}) - 1} \cdot \Big(GPSP(I_G) - 1\Big) + 1 \tag{3.35}$$

$$\widetilde{GP}(I_G) = GP(I_G) \cdot \frac{GE(I'_\theta)}{GE(I_{\theta,main})} \cdot \widetilde{GPSP}(I_G) \tag{3.36}$$

$$I'_G = \widetilde{GP}^{-1}(G_t) \tag{3.37}$$

$$\widetilde{PPSP}(I_{\theta,aux}) = AG2\Delta\theta(I'_G) - G2\Delta\theta(I'_G) \tag{3.38}$$

$$\widetilde{PPSP}(I_\theta) = \frac{\widetilde{PPSP}(I_{\theta,aux})}{PPSP(I_{\theta,aux})} \cdot PPSP(I_\theta) \tag{3.39}$$

$$\widetilde{PP}(I_\theta) = PP(I_\theta) + G2\Delta\theta(I'_G) + \widetilde{PPSP}(I_\theta) \tag{3.40}$$

$$I'_\theta = \widetilde{PP}^{-1}(\theta_t) \tag{3.41}$$

$$\textit{Go to } (3.34) \tag{3.42}$$

The iteration should continue until the solved phase index at (3.41) is equal to or within a specified step size of its initial solution in the current iteration, meaning the solutions have settled. When it settles, the resulting gain index I_G and phase index I_θ are stored in the look-up table (LUT) mapping to the current requested targeting position.

The choice of starting the iteration with the phase index first guess is arbitrary. A solution could also be found by first starting with a gain index first guess.

3.2.6 Optimum Sampling Indexes Selection

For the most accurate and consistent calibration performance, the $I_{G,aux}$, $I_{\theta,main}$ and $I_{\theta,aux}$ need to be optimally selected so that the characterization dataset captures the most variations.

As demonstrated in the previous sections, the $GPSP$ and $PPSP$ must be adjusted to be applicable in the solver. Therefore, the captured $GPSP$ and $PPSP$ should exhibit well-defined shapes.

Similar to the relationship in (3.24), the value of the captured $GPSP$ at the $I_{G,aux}$ is:

$$GPSP(I_{G,aux}) = \frac{GESP(I_{\theta,aux})}{GESP(I_{\theta,main})} \tag{3.43}$$

To achieve the most defined $GPSP$, the calculated value in (3.43) needs to be maximized. This requires $I_{\theta,main}$ and $I_{\theta,aux}$ to yield the minimum and maximum values in $GESP$, respectively. Additionally, since $I_{\theta,aux}$ is where the observation lies in the $PPSP$, it is essential for the $PPSP$ to have a significant value at $I_{\theta,aux}$ to ensure the most accurate $PPSP$ scaling. Realizing the above considerations, $I_{\theta,main}$ and $I_{\theta,aux}$ are chosen as:

$$I_{\theta,main} = argmin(GESP(I_\theta)) \tag{3.44}$$

$$I_{\theta,aux} = argmax\left(|PPSP(I_\theta)| \cdot (GESP(I_\theta) - min(GESP(I_\theta)))\right) \tag{3.45}$$

For a defined $PPSP$, the value of the captured $PPSP$ at the $I_{\theta,aux}$ is:

$$PPSP(I_{\theta,aux}) = AG2\Delta\theta(I_{G,aux}) - G2\Delta\theta(I_{G,aux}) \tag{3.46}$$

Note that unlike the $GPSP$, there is no choice of $I_{G,aux}$ other than the ends that gives the maximum $PPSP$ since both the $G2\Delta\theta(I_{G,aux})$ and $AG2\Delta\theta(I_{G,aux})$ are non-periodic series. To avoid extremes and ensure a defined $PPSP$, the $I_{G,aux}$ is chosen to be the middle gain sampling index.

Accommodating for the optimal sampling indexes, an optimized characterization flow is shown in Fig. 3.9.

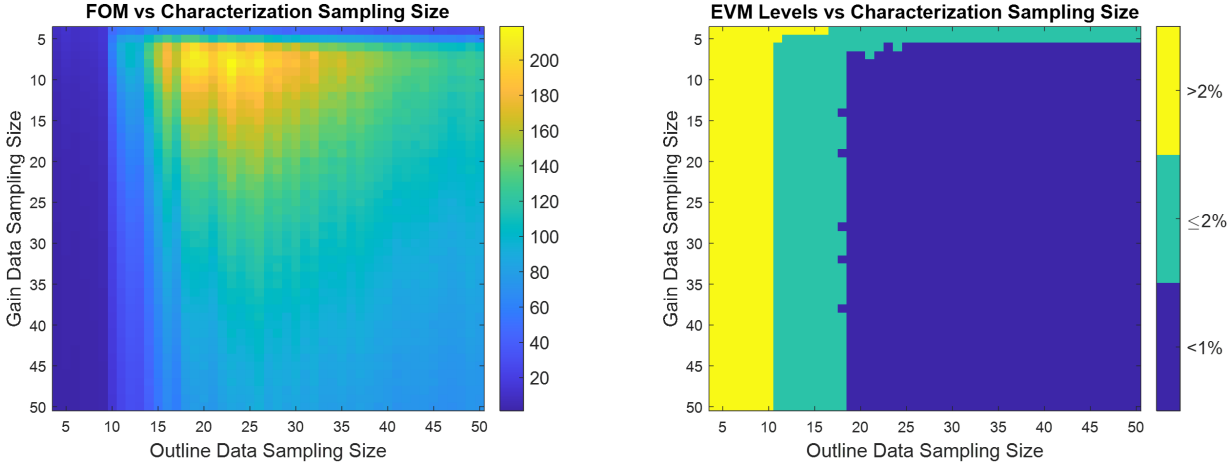
3.2.7 Optimum Sampling Size

To test the effect of changing the sampling size on the calibration performance, the gain data sampling size and the outline data sampling size are swept from 4 to 50 as we record the calibration result of the two channels of the BFIC1. The figure-of-merit of the characterization sampling size is defined as:

$$FOM = (EVM^2 \cdot measurement\ count)^{-1} \tag{3.47}$$

where EVM is the error vector magnitude of all the targeting points averaging over the two channels. Note that we are putting a larger emphasis on the accuracy of the calibration over the number of measurements.

Figure 3.23 below shows the FOM and the EVM levels of the calibration as we vary the sampling size. From figure 3.23a, the sampling size giving the highest FOM is shown in the yellow color region and it is approximately for gain data sampling size from 6 to 10 and for outline data sampling size from 18 to 26. From figure 3.23b, we can see that the EVM of the calibration is less than 1% if the gain data sampling size is greater than 7 and the outline data sampling size is greater than 18. For an outline data sampling size greater than 24, the gain data sampling size only needs to be greater than 5 for the EVM to remain below 1%. This shows the calibration result is stable over the sampling sizes and the optimum result can be reached early using a small sampling size.



(a) (b)

Figure 3.23: Calibration result over the two channels of the BFIC1 with varying characterization sampling size. Targeting 64 phase states, 8 gain states with 1dB gain tunning resolution. (a) FOM; (b) EVM levels.

3.2.8 Targeting Gain Allocation with Tapering Awareness

Typically in array calibration [32, 33], each VGPS in the array is throttled to meet with the VGPS with the minimum gain (maximum uniform gain shown in Fig. 3.24a). This is to ensure gain-invariant phase swing for each element accounting for any gain tapering profile. Subsequently, each VGPS is calibrated with multiple gain states with a defined gain tuning resolution to apply the tapering profile. This method is referred to as the "Forced" taper, as the taper is applied on top of the discrete calibrated gain states.

If the desired gain tapering is known before array calibration, we can directly target the tapered gain states for each element, achieving higher gains compared to the forced taper by optimizing the allocation of array power. The tapering profile indicates the expected power level from each element, thus setting a tapered maximum gain limit on the elements. This scheme, referred to as "Taper Aware", reflects that the calibration process is aware of the tapering profile.

For an N-by-N array, let $\boldsymbol{G}_{max}$ be the matrix of maximum gains of each element in decibels allowing for gain-invariant phase swing. Its entry for the i-th element is calculated as:

$$G_{max,i} = 20\ log(min(GE_i)) \tag{3.48}$$

where GE_i is the gain envelope for the i-th element. Let $\boldsymbol{C}$ be the matrix of the normalized gain tapering coefficient in decibels of each element. Incorporating taper awareness, the matrix of targeting gains of each element $\boldsymbol{G}_t$ is calculated as:

$$\boldsymbol{G}_t = \boldsymbol{C} - max(\boldsymbol{C} - \boldsymbol{G}_{max}) \tag{3.49}$$

The setting of targeting gains of a 4-by-4 array and using the Taylor window gain tapering profile is demonstrated in Fig. 3.24. As observed, with the proposed taper awareness, the targeting gains of the array are significantly increased.

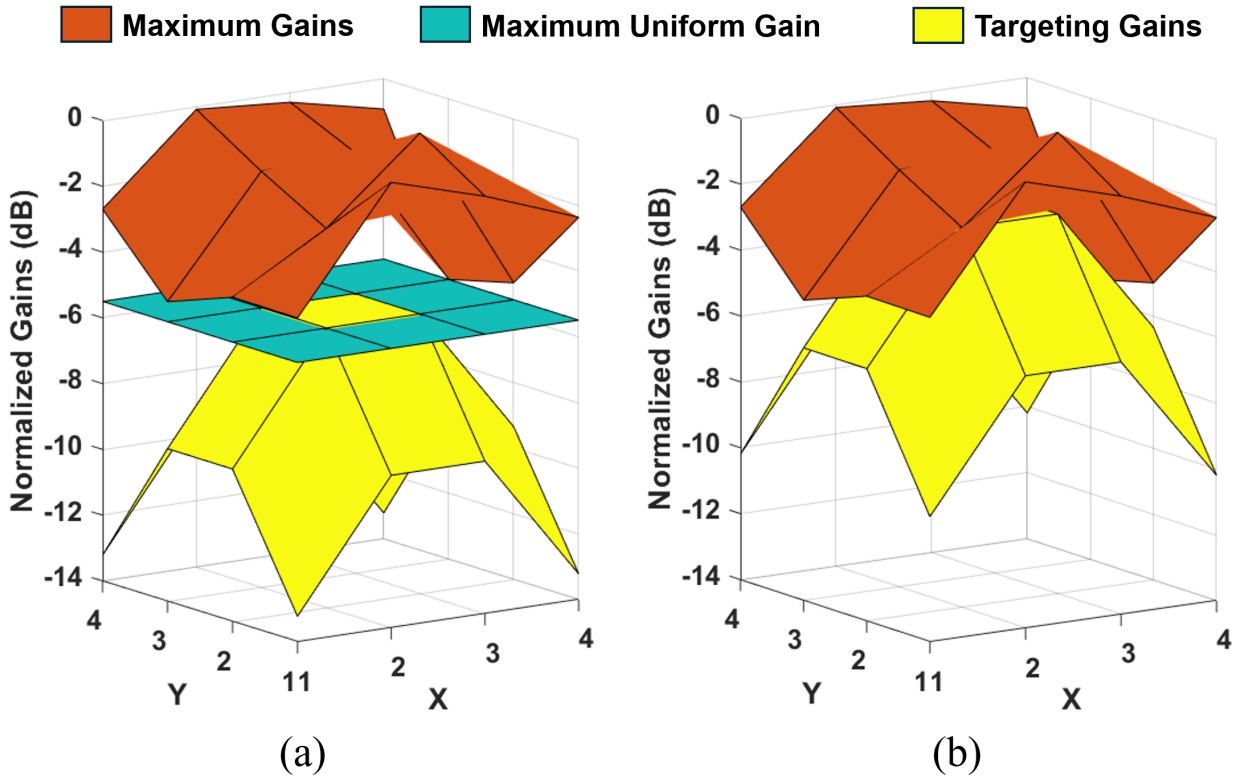


Figure 3.24: Demonstration of the setting of targeting gain states for a 4x4 array with Taylor window gain tapering profile: (a) typical; (b) with taper awareness.

3.3 Adaptive Kernel Search Algorithm

3.3.1 Overview

As previously shown in Fig. 3.4, in the supervised calibration routine, the algorithm initially employs the proposed characterization method to come up with gain and phase indices for the specified constellation positions. It then measures suggested points and evaluates them using pre-defined "Validation Criteria". In any case of disqualification, the algorithm selects the next set of position(s) to find a verified solution for the target point through a process called "Position Compensation". If the measurements do not converge to the targeting point after several iterations, the search area, referred to as the "Kernel", expands and the algorithm performs more measurement iterations. Detailed introduction

of the kernel, validation criteria, and position compensation process are discussed in the following sections. Also, flow charts illustrating the entire adaptive kernel search process can be found in Fig. 3.25.

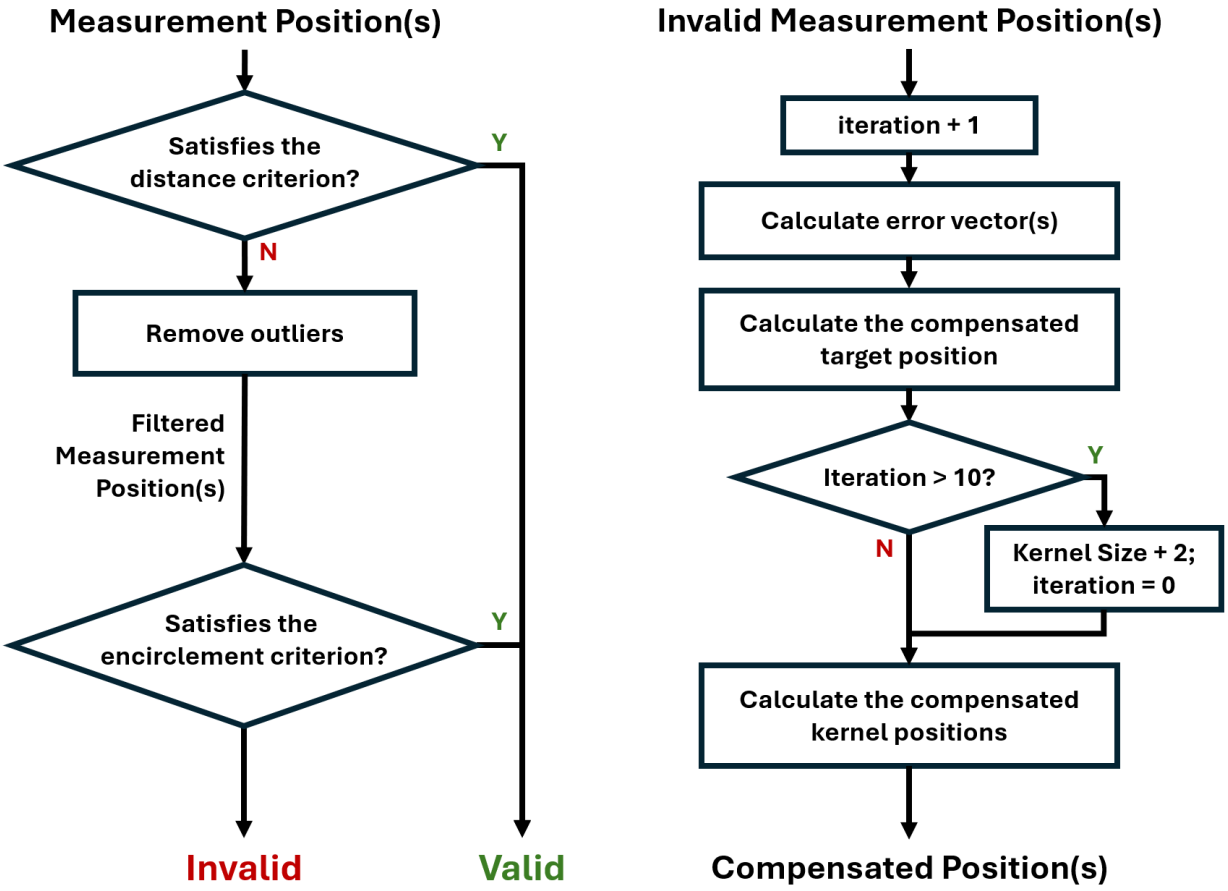


Figure 3.25: Adaptive Kernel Search flow charts: (a) Validation criteria; (b) Position compensation and kernel size expansion.

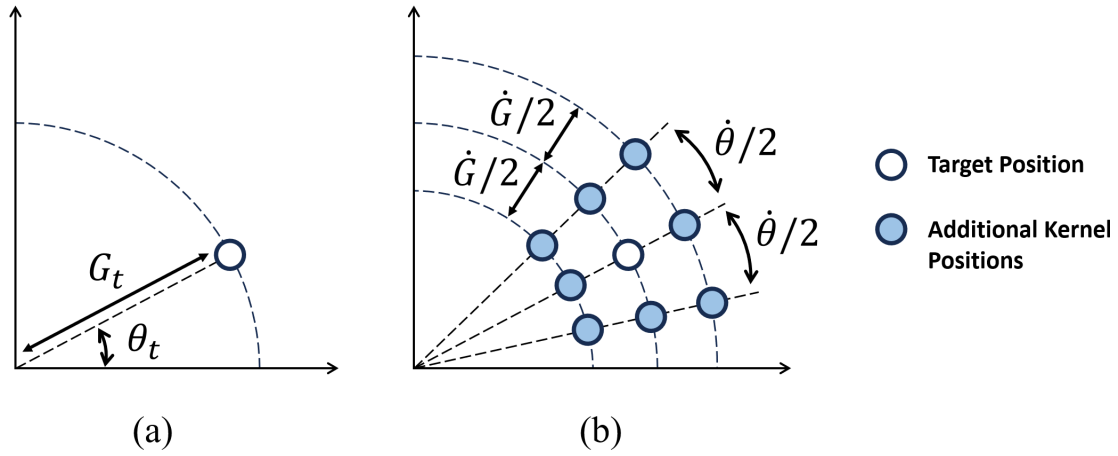


Figure 3.26: Kernel demonstration for: (a) Kernel size N=1; (b) Kernel size N=3.

3.3.2 Kernel Definition

A kernel of size N is a search area consisting of $N \times N$ points and it is demonstrated graphically in Figure 3.26.

In the calibration of a target point in a supervised calibration routine, the kernel size is initially set to 1, shown in Fig. 3.26a, which means the initial search area is just the target point with an absolute value of G_t and phase of θ_t. G_t and θ_t represents the target gain and target phase. When the kernel size (search area) expands to 3, shown in Fig. 3.26b, the target position is surrounded by additional kernel positions and the number of measurements becomes $3 \times 3 = 9$. The additional kernel positions are half steps of polar VGPS resolutions away from the target point. In Figure 3.26b, $\dot{G}$ and $\dot{\theta}$ represent the VGPS gain resolution and the VGPS phase resolution.

A kernel $\mathbf{K}$ of size N is represented mathematically as an N-by-N matrix:

$$\mathbf{K} = \begin{bmatrix} K(1,1) & \dots & K(1,N) \\ \vdots & \ddots & \vdots \\ K(N,1) & \dots & K(N,N) \end{bmatrix}, \; for \; N = 1,3,5,... \tag{3.50}$$

Let $P_{G,\theta}$ denotes the position with an absolute value of G and a phase of θ:

$$P_{G,\theta} = G \cdot e^{j\theta} \tag{3.51}$$

then each element in the kernel is defined as:

$$K(i,j) = P_{G_t + \frac{\dot{G}}{2}\cdot(i-\frac{N+1}{2}),\theta_t + \frac{\dot{\theta}}{2}\cdot(j-\frac{N+1}{2})} \tag{3.52}$$

where G_t is the target gain, θ_t is the target phase, $\dot{G}$ is the VGPS gain resolution and $\dot{\theta}$ is the VGPS phase resolution. The order of measurement for elements in the kernel does not matter. An example kernel of size 3 would be:

$$\mathbf{K}_3 = \begin{bmatrix} P_{G_t-\frac{\dot{G}}{2},\theta_t-\frac{\dot{\theta}}{2}} & P_{G_t-\frac{\dot{G}}{2},\theta_t} & P_{G_t-\frac{\dot{G}}{2},\theta_t+\frac{\dot{\theta}}{2}} \\ P_{G_t,\theta_t-\frac{\dot{\theta}}{2}} & P_{G_t,\theta_t} & P_{G_t,\theta_t+\frac{\dot{\theta}}{2}} \\ P_{G_t+\frac{\dot{G}}{2},\theta_t-\frac{\dot{\theta}}{2}} & P_{G_t+\frac{\dot{G}}{2},\theta_t} & P_{G_t+\frac{\dot{G}}{2},\theta_t+\frac{\dot{\theta}}{2}} \end{bmatrix} \tag{3.53}$$

From the size 3 kernel in (3.53), we confirm that the center element is the target point. Elements above and below are half a step of VGPS gain resolution apart, while elements to the left and right are half a step of VGPS phase resolution apart. If the constellation is continuous, these half-step increments ensure there are no possible solutions in between even with varying native resolution, allowing a local best solution to surface via the "encirclement criterion" defined in the validation criteria in Section 3.3.3.

3.3.3 Validation Criteria

The validation criteria aim to determine whether the current set of measurements contains a solution for the current target point. Once validated, the closest measurement to the target point will be selected, and the corresponding gain and phase indices will be saved to the LUT. To identify the validation zone, the "distance criterion" and "encirclement criterion" are defined as follows:

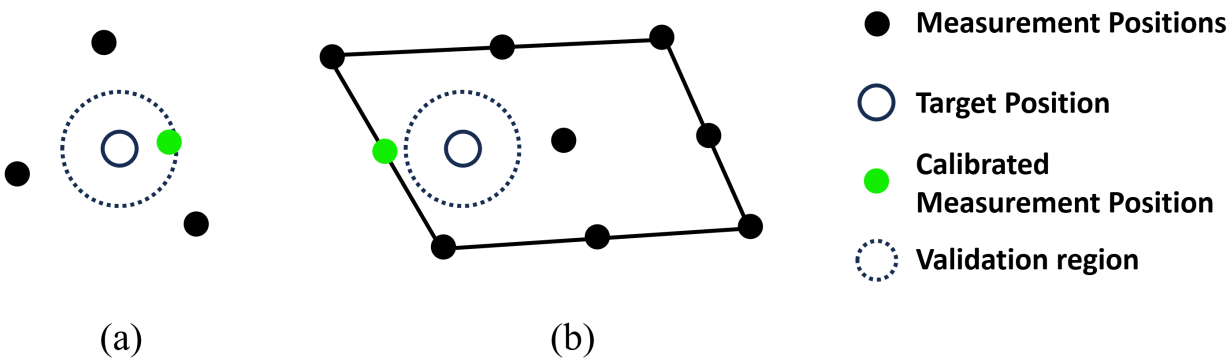


Figure 3.27: Validation criteria: (a) Distance criterion; (b) Encirclement criterion.

Distance Criterion

The distance criterion checks if the measured points are within the specified vicinity of the current target point. A circular "validation region" is defined around the target point with a radius calculated in (3.54). As shown in Fig. 3.27a and described in the flow chart in Fig. 3.25a, a set of measurements is validated if any of the measurement positions fall inside the validation region.

The radius of the validation region is calculated individually for every target point and it is demonstrated in Fig. 3.28. For each target point, the radius of the validation region is defined as the minimum distance from the target point to its nearest neighboring target points divided by a coefficient T that is larger than or equal to 2:

$$R_{val} = min(|P_{G_t,\theta_t} - P_{G_t \pm \dot{G}_t, \theta_t \pm \dot{\theta}_t}|) \cdot \frac{1}{T}, \quad for\ T \geq 2 \tag{3.54}$$

where R_{val} is the radius of the validation region, $\dot{G}_t$ is the target gain resolution, $\dot{\theta}_t$ is the target phase resolution and T is the validation tolerance coefficient.

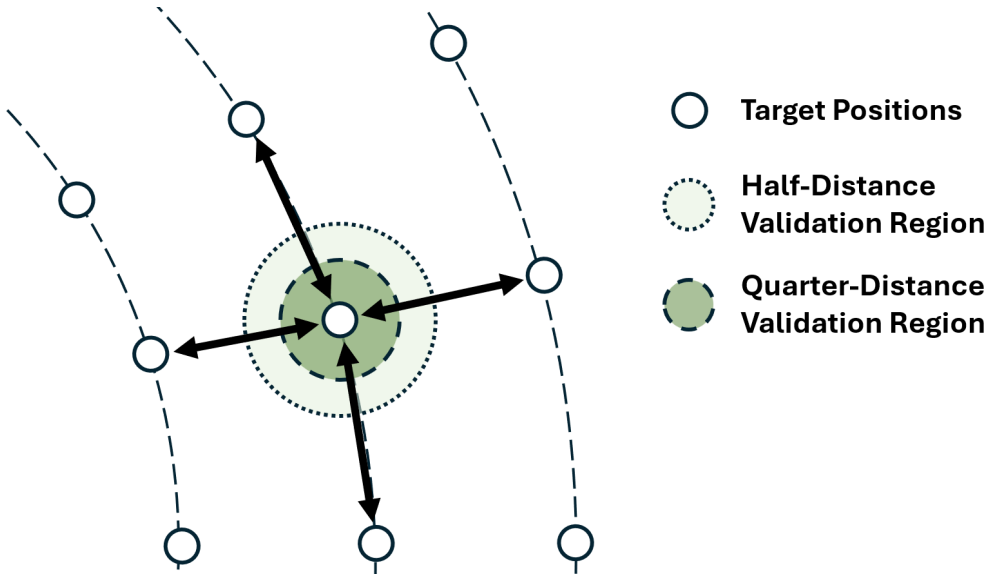


Figure 3.28: Validation region for a target point. Figure showing half-distance validation region (dotted line) and quarter-distance validation region (dashed line).

A higher validation tolerance coefficient would lead to a smaller validation region, as demonstrated by the quarter-distance validation region in Fig. 3.28, and consequently

stricter criteria for gain and phase error. The most relaxed distance criterion is achieved with a validation tolerance coefficient of 2 as demonstrated by the half-distance validation region in Fig. 3.28. In this most relaxed case, the validation regions of different target points are at most touching each other thus avoiding overlapping validations.

Encirclement Criterion

If the current set of measurements fails the distance criterion, then the encirclement criterion checks if the current target point is encircled by the current set of measurements as described in the flow chart in Fig. 3.25. Note that the encirclement criterion is only meaningful when the kernel size is larger than 1.

Since the additional kernel positions are half steps of VGPS resolutions away from the target position, a continuous VGPS constellation ensures there are no other possible measurement positions within the boundary created by the current measurements. Therefore, a local best solution is found if the target position is within this boundary. This criterion is graphically illustrated in Fig. 3.27b.

As shown in the flow chart in Fig. 3.25a, it is important to filter the current set of measurements to remove outliers before calculating the boundary. Outliers can distort the validation boundaries, leading to inaccurate results.

Also, for high-resolution VGPS, it might be advantageous to increase the steps in the expansion of the kernel so that the measured kernel positions would occupy a bigger space and thus easier to encircle the target position and reducing the number of iterations. The risk of increasing the steps in the kernel is that the algorithm might overlook some possible solutions and miss the local best solution.

3.3.4 Position Compensation

If the current set of measurements as requested by the kernel is invalid, there is no solution for the target point within that kernel. The position compensation algorithm aims to identify the next kernel to measure, ensuring the new measurements are closer to the target point and more likely to be valid.

The position compensation process is illustrated in Figure 3.29. The algorithm starts by calculating error vectors from the ideal kernel positions to the measured positions. An average error vector for the kernel is then computed and used to determine the compensated target point's position. A new kernel is built around this compensated target point and

measured in the next iteration. As shown in the flow chart in Fig. 3.25b, if the compensated kernel remains invalid after several iterations, the kernel size expands. In our testing, we set an iteration threshold of 10 and a kernel expansion step of 2, increasing the kernel size by 2 after every 10 failed iterations.

Notably, the measurement positions are stored in memory, avoiding repeated actual measurements for the same gain and phase indexes. Thus, if a solution is hard to find due to local constellation gaps, the kernel compensation often makes small adjustments over multiple iterations, frequently resolving to the same gain and phase index. Consequently, the number of measurements does not increase linearly with iterations.

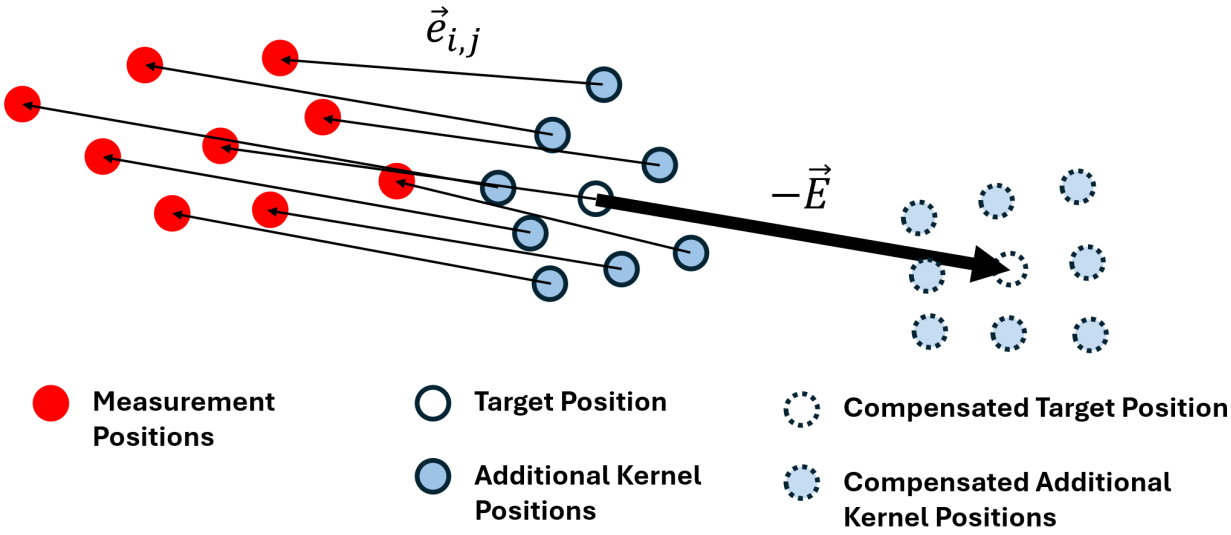


Figure 3.29: Position Compensation demonstration for a kernel of size 3.

Let $\mathbf{M_K}$ be the matrix of measurement positions acquired from measuring gain and phase indexes solved from the targeting positions in the kernel $\mathbf{K}$. The error vector matrix $\mathbf{e}$ is defined as the difference between the measurement positions $\mathbf{M_K}$ and the kernel $\mathbf{K}$:

$$\mathbf{e} = \mathbf{M_K} - \mathbf{K} \tag{3.55}$$

Each element in the resulting error vector matrix $\mathbf{e}$ represents the error vector between the kernel position $K(i,j)$ and its corresponding measurement position $M_K(i,j)$:

$$\mathbf{e} = \begin{bmatrix} \vec{e}_{1,1} & \cdots & \vec{e}_{1,N} \\ \vdots & \ddots & \vdots \\ \vec{e}_{N,1} & \cdots & \vec{e}_{N,N} \end{bmatrix} \tag{3.56}$$

$$\vec{e}_{i,j} = M_K(i,j) - K_N(i,j) \tag{3.57}$$

It is important to point out that the calculation of error vectors only considers those kernel positions whose measurement positions are not identified as outliers in the validation criteria.

The average error vector $\vec{E}$ is defined as the average of all of the elements in the error vector matrix $\mathbf{e}$:

$$\vec{E} = mean(\mathbf{e}) \tag{3.58}$$

As demonstrated in Figure 3.29, the average error vector $\vec{E}$ is then used to calculate the position of the compensated target point. Let $\hat{P}_t$ be the position of the compensated target point:

$$\hat{P}_t = P_{G_t,\theta_t} - \vec{E} = P_{\hat{G}_t,\hat{\theta}_t} \tag{3.59}$$

where $\hat{G}_t$ and $\hat{\theta}_t$ are the compensated target gain and phase and they are calculated as:

$$\hat{G}_t = |P_{G_t,\theta_t} - \vec{E}| \tag{3.60}$$

$$\hat{\theta}_t = phase(P_{G_t,\theta_t} - \vec{E}) \tag{3.61}$$

With the compensated target point, the compensated kernel $\hat{\mathbf{K}}$ of size N has its elements as:

$$\hat{K}(i,j) = P_{\hat{G}_t + \frac{\dot{G}}{2}\cdot(i-\frac{N+1}{2}),\hat{\theta}_t + \frac{\dot{\theta}}{2}\cdot(j-\frac{N+1}{2})} \tag{3.62}$$

A compensated kernel of size 3 would be:

$$\hat{\mathbf{K}}_3 = \begin{bmatrix} P_{\hat{G}_t-\frac{\dot{G}}{2},\hat{\theta}_t-\frac{\dot{\theta}}{2}} & P_{\hat{G}_t-\frac{\dot{G}}{2},\hat{\theta}_t} & P_{\hat{G}_t-\frac{\dot{G}}{2},\hat{\theta}_t+\frac{\dot{\theta}}{2}} \\ P_{\hat{G}_t,\hat{\theta}_t-\frac{\dot{\theta}}{2}} & P_{\hat{G}_t,\hat{\theta}_t} & P_{\hat{G}_t,\hat{\theta}_t+\frac{\dot{\theta}}{2}} \\ P_{\hat{G}_t+\frac{\dot{G}}{2},\hat{\theta}_t-\frac{\dot{\theta}}{2}} & P_{\hat{G}_t+\frac{\dot{G}}{2},\hat{\theta}_t} & P_{\hat{G}_t+\frac{\dot{G}}{2},\hat{\theta}_t+\frac{\dot{\theta}}{2}} \end{bmatrix} \tag{3.63}$$

Note that this implementation compensates only the target point using the average error vector, while other points in the kernel are generated based on the kernel's definition. Alternatively, all positions could be compensated individually using their respective error vectors in $\mathbf{e}$. However, due to the high accuracy of the proposed characterization method, the results should be similar for both implementations.

3.4 Experimental Validation

The two proposed calibration routines are tested on two different commercially available BFICs and two different arrays built using those two BFICs. The measurement is conducted at 25 degrees Celsius and at 38.5GHz which is the center frequency of the two BFICs rated frequency range. For confidentiality reasons under the non-disclosure agreement, the names and part numbers of the two commercially available BFICs used for testing are not disclosed.

For the BFIC calibrations in this section, we include the measurement and calibration setup, calibrated constellation comparison for a single constellation setting and calibration results comparison table for multiple constellation settings. For the array calibrations in this section, we include the measurement and calibration setup, the table showing the constellation performance and the radiation patterns.

3.4.1 BFIC1 Calibration

BFIC1 is a 37.1 - 40GHz quad channel analog beamforming IC and it has 8-bit gain control and 8-bit phase control.

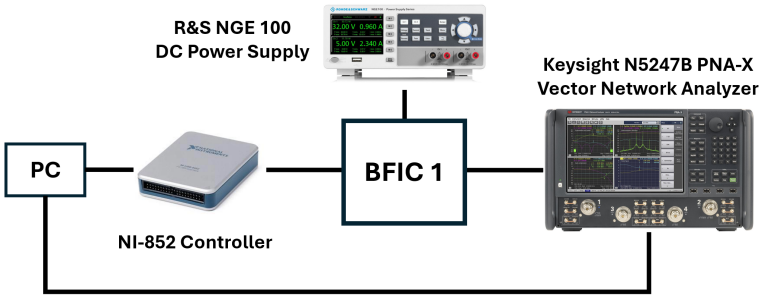
BFIC1 Measurement Setup

Figure 3.30a shows the block diagram of the measurement setup and Figure 3.30b shows a picture of that setup. The algorithm is running in MATLAB installed on the PC which communicates with the national instrument controller (NI-852) to send control bits to the IC. The IC is powered by ROHDE&SCHWARZ NGE 100 DC power supply. The measurement instrument is the Keysight N5247B PNA-X vector network analyzer which measures the S-parameters of the IC. The measured S-parameters are then sent to the PC and read by the calibration algorithm.

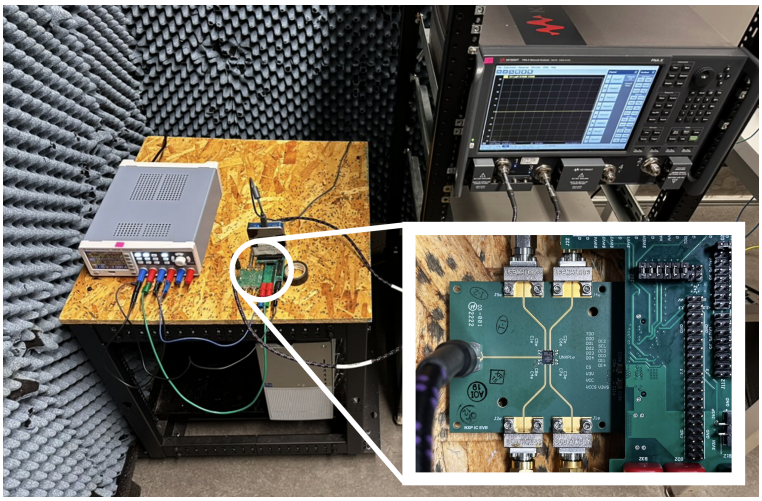
BFIC1 Calibration Setup

For the BFIC calibration demonstrated in this section, the maximum targeting gains are calculated without the proposed gain tapering awareness. To demonstrate the efficacy of the two proposed calibration routines. We benchmark them against the most accurate calibration method “Exhaustive Search” and the “No Calibration” method which is to

input the gain and phase indexes directly with no look-up-table. We evaluate the "No Calibration" method since some BFICs come pre-calibrated with a factory set look-up-table and they are advertised to be used "calibration-free".



(a)



(b)

Figure 3.30: Measurement setup for BFIC1: (a) Setup block diagram; (b) Setup picture.

Note that for the "No Calibration" method, to keep the scenario realistic, the phase and magnitude of the control state with the phase index of 1 and the maximum gain is referenced as the 0 phase and the maximum targeting gain for the calibration. Also, the gain tuning setting is guided by the least-significant-bit (LSB) specified in the datasheet.

Figure 3.31 below shows the single-channel full measurement of the BFIC1 for the exhaustive search method. We can see the measurements are clean and the constellation is dense and continuous.

For the proposed calibration method, we choose an outline data sampling size of 23 and a gain data sampling size of 8 for the optimal calibration FOM (section 3.23) which means only 58 measurements are needed to characterize the 8-bit phase and 8-bit gain BFIC1. Due to the excellent accuracy of the proposed characterization method, the supervised routine only performs a significant amount of corrections when the validation is very strict. The supervised routine uses a validation tolerance coefficient T of 10 which means the validated points are 5 times closer to the targeting points than what's needed to satisfy the targeting phase and gain resolution.

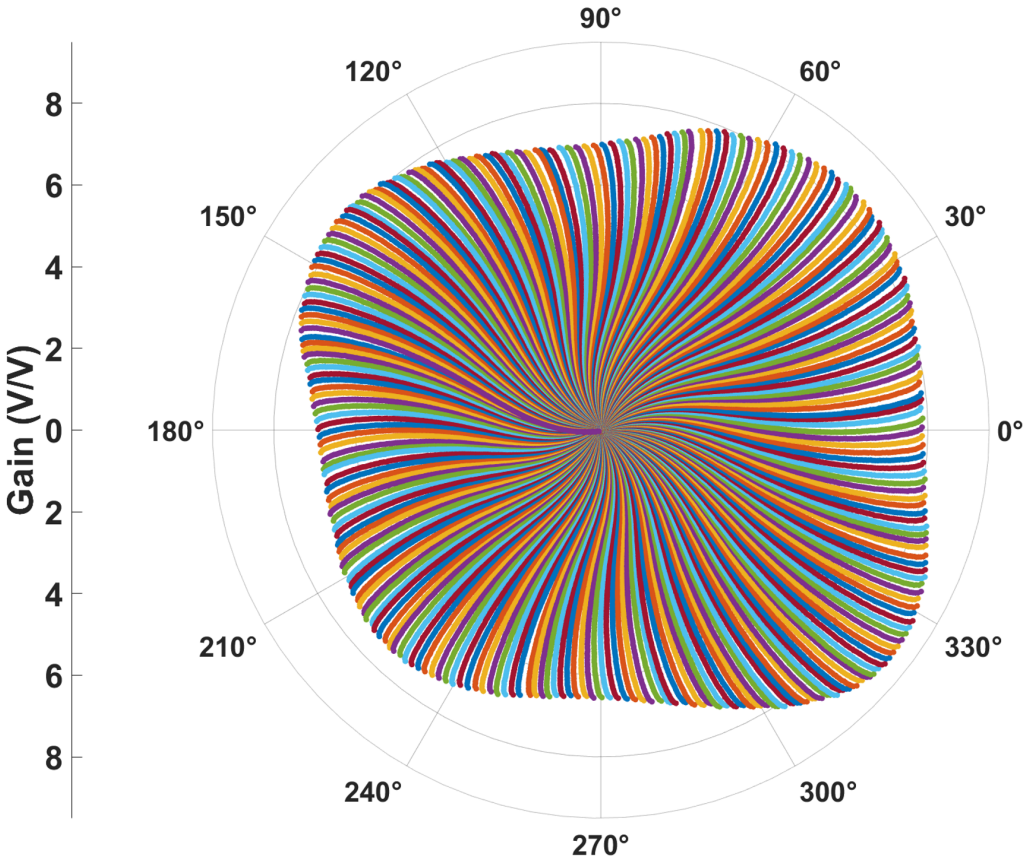


Figure 3.31: BFIC1 single-channel full measurement.

It is important to clarify that, in order to show the calibration performance of the proposed unsupervised routine, test measurements need to be done for us to evaluate the gain and phase errors of each of its solved gain and phase indexes. Those test measurements are not performed in the practical operation of the unsupervised calibration routine.

BFIC1 Calibrated Constellation Comparison

Figure 3.32 below shows the calibrated constellation of the BFIC1 using two benchmarking methods and two proposed methods. The calibration in figure 3.32 targets 64 phase states, 8 gain states with 1dB gain tuning resolution. Calibration results targeting different constellation settings are included in the table 3.1 below.

From the calibrated constellations in Figure 3.32 below, it is evident that the two proposed calibration routines produce results nearly identical to that of the exhaustive search method. In contrast, the constellation with no calibration exhibits significantly larger errors. Note that the magnitude of the constellation without calibration is slightly higher than the calibrated constellations since the calibration needs to sacrifice the gain in some of the directions to ensure gain-invariant phase tuning and this is ensured by the maximum targeting gain condition in (3.48).

The calibrated constellation points in both the supervised and unsupervised constellations are spatially distinguishable and they fall in the vicinity of their corresponding targeting constellation points. Comparing the supervised and unsupervised constellation to that of the exhaustive search method, we see that the supervised constellation is a little bit better as a result of the super tight setting of the validation tolerance coefficient.

We can also interpret the unsupervised constellation as the first guess into the adaptive kernel search algorithm in the supervised routine. We can see that the first guesses for the desired constellation are already really accurate for this BFIC and the supervised routine needs to have a tight validation region to show its ability to account for the intricate and somewhat "random" response details that the characterization cannot model.

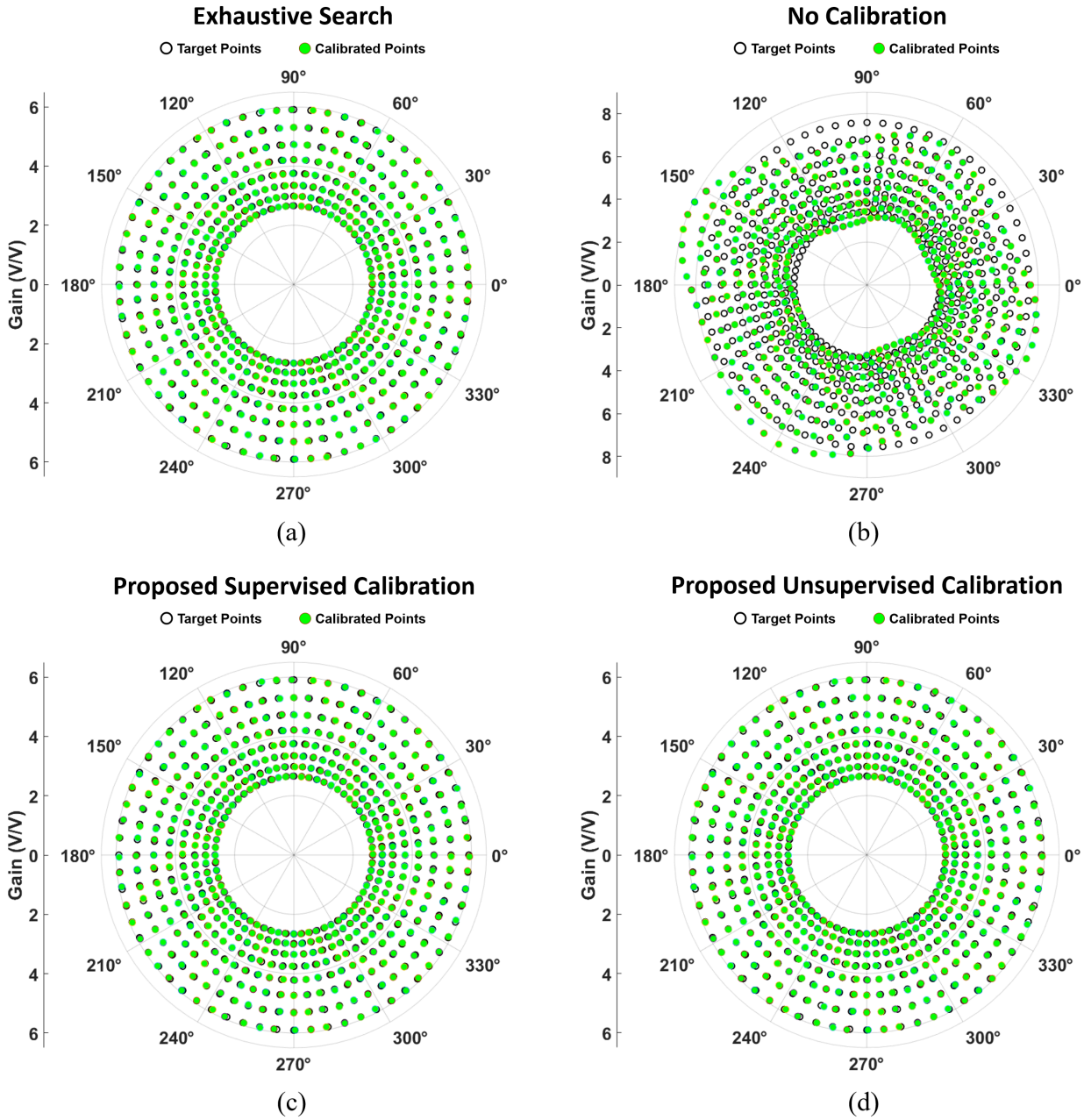


Figure 3.32: Calibrated targeting constellation on BFIC1 using different calibration methods. Targeting 64 phase states, 8 gain states with 1dB gain tuning resolution. Proposed characterization method using outline data sampling size of 23 and gain data sampling size of 8. (a) Exhaustive search; (b) No calibration; (c) Proposed supervised calibration; (d) Proposed unsupervised calibration.

Table 3.1: BFIC1 calibration results comparison. Characterized using outline data sampling size of 23 and gain data sampling size of 8. The supervised routine has the validation tolerance coefficient set to 10.

	Exhaustive Search	**Supervised**	**Unsupervised**	**No Calibration**
Target 5-bit phase, 8 gain states with 1dB gain tuning resolution				
Phase RMSE (°)	0.40	0.41	0.44	3.04
Peak Phase Error (°)	0.86	0.86	1.06	8.08
Gain RMSE (dB)	0.02	0.03	0.04	0.72
Peak Gain Error (dB)	0.06	0.09	0.09	1.68
EVM (%)	0.73	0.79	0.85	9.46
# of Measurements	65536	467	58	0
Calibration Time	5h 23m	2m	16.4s	0
Target 6-bit phase, 8 gain states with 1dB gain tuning resolution				
Phase RMSE (°)	0.40	0.41	0.45	3.05
Peak Phase Error (°)	0.93	0.93	1.20	8.09
Gain RMSE (dB)	0.02	0.03	0.03	0.73
Peak Gain Error (dB)	0.06	0.08	0.12	1.68
EVM (%)	0.73	0.77	0.85	9.52
# of Measurements	65536	1050	58	0
Calibration Time	5h 23m	5m	16.8s	0
Target 8-bit phase, 8 gain states with 1dB gain tuning resolution				
Phase RMSE (d°)	0.40	0.40	0.46	3.06
Peak Phase Error (°)	0.97	0.97	1.40	8.17
Gain RMSE (dB)	0.02	0.02	0.04	0.73
Peak Gain Error (dB)	0.07	0.07	0.13	1.70
EVM (%)	0.72	0.72	0.86	9.53
# of Measurements	65536	5110	58	0
Calibration Time	5h 23m	25m	17.1s	0
Target 8-bit phase, 16 gain states with 0.5dB gain tuning resolution				
Phase RMSE (°)	0.41	0.41	0.47	3.09
Peak Phase Error (°)	0.99	0.99	1.41	9.09
Gain RMSE (dB)	0.02	0.02	0.04	0.72
Peak Gain Error (dB)	0.07	0.07	0.13	1.70
EVM (%)	0.73	0.73	0.88	9.52
# of Measurements	65536	10237	58	0
Calibration Time	5h 23m	50m	17.5s	0

BFIC1 Calibration Results Comparison

Table 3.1 above shows the calibration results comparing different methods and targeting different numbers of phase and gain states. We can see that the calibration results of the two proposed calibration routines are similar to that of the exhaustive search method in terms of phase and gain errors across all cases while performing a fraction of the measurements. The no calibration method, however, consistently delivers the worst performance by far with EVMs averaging about 9.5% in all cases and we can conclude that the BFIC1 is not suited for operating without calibration.

To highlight the efficiency of the proposed unsupervised calibration, which only uses the proposed characterization to solve the gain and phase indexes, it achieves excellent and consistent gain and phase Root Mean Square Error (RMSE) across different constellation settings while only performing 58 measurements. Compared to the 65536 measurements demanded by the exhaustive search method, it achieves this excellent result using 1100 times fewer measurements. In terms of calibration time, the unsupervised calibration finishes at around 16 to 17 seconds which is worlds apart from the five and half hours needed for the exhaustive search method. For beamforming purposes, the difference in the gain and phase errors and the achieved EVM is virtually identical using the exhaustive search and the proposed unsupervised calibration. This shows the exceptional accuracy and efficiency of the proposed characterization method.

For the unsupervised calibration, the achieved EVM, which accounts for both gain and phase errors, stays constant as we target higher phase and gain resolutions. For higher targeting resolutions, the margins for the gain and phase errors become smaller thus the achieved gain and phase errors in proportion to the needed errors to satisfy the targeting resolution becomes worse. In the case of targeting 8-bit phase and 16 gain states with 0.5dB gain resolution, the phase RMSE and gain RMSE need to be lower than 0.7 degrees and 0.25dB respectively for the achieved points to be distinguishable. For this high-resolution setting, our unsupervised calibration achieves phase RMSE and gain RMSE of 0.47 degrees and 0.04dB respectively which still comfortably fits in the margin.

Another note on the unsupervised calibration is that the number of measurements needed for a high FOM is not dependent on the native resolution of the VGPS but instead depends on the level of variation in the constellation. This means that to calibrate a VGPS of even higher resolution (9-bit for example), the number of measurements needed does not scale up linearly making it ideal for calibrating super high-resolution VGPSs in the future. However, this also means the advantage of the unsupervised calibration is not as pronounced if the VGPS is of low resolution.

The supervised calibration is a fail-safe for the unsupervised calibration in that it actively checks every solution. We can observe its fail-safe nature by confirming the significant peak phase and gain error reduction by moving from unsupervised calibration to supervised calibration. The supervised routine should improve every metric of the unsupervised routine where possible and necessary to satisfy the validation criteria at the cost of performing a number of measurements at least as large as the number of targeting points.

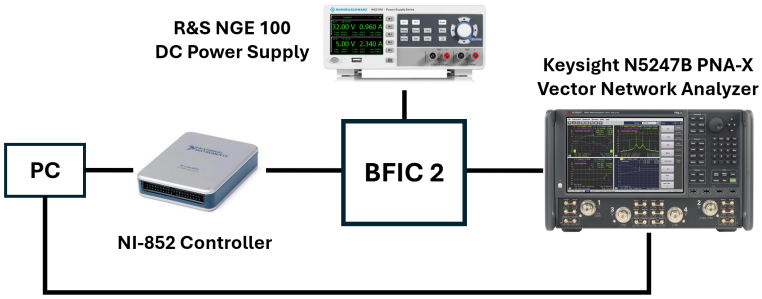
We can see that the number of measurements needed for the supervised routine quickly rises as we target higher gain and phase resolutions. When targeting a higher resolution, the validation region becomes smaller making the adaptive kernel search algorithm take more iterations and larger kernel size to find a solution, contributing to the rapid rise of the number of measurements. In all cases, the supervised calibration strikes a balance in the calibration result and the number of measurements between the exhaustive search and the unsupervised calibration.

It is worth noting that if the validation tolerance coefficient in the supervised calibration is set to infinity, meaning the routine relies solely on the encirclement criterion, the supervised calibration result becomes equivalent to the exhaustive search calibration result, albeit by measuring only points near the target points. Therefore, if the user aims to achieve the best calibration performance possible, the supervised routine can deliver it with the same or fewer measurements compared to the exhaustive search method.

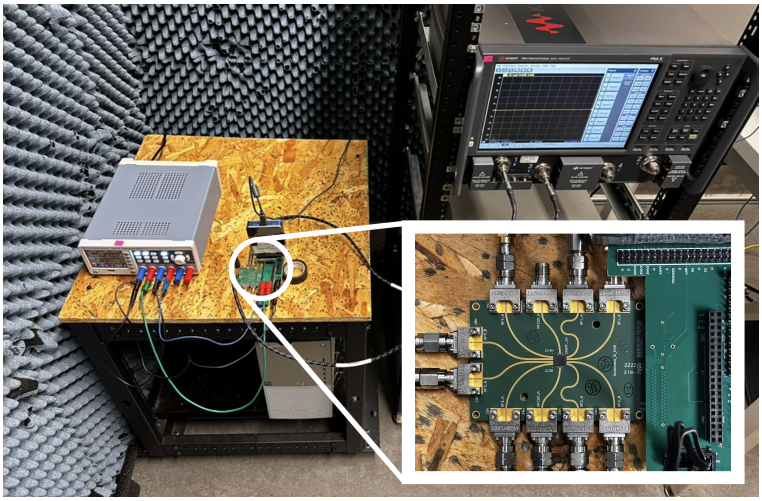
3.4.2 BFIC2 Calibration

BFIC2 is a 37-40 GHz Dual Polarized Quad 4x2 Beamforming IC and it has 5-bit gain control (4-bit gain for each element) and 6-bit phase control.

BFIC2 Measurement Setup



(a)



(b)

Figure 3.33: Measurement setup for BFIC2: (a) Setup block diagram; (b) Setup picture.

Figure 3.33a shows the block diagram of the measurement setup and Figure 3.33b shows a picture of that setup. The algorithm is running in MATLAB installed on the PC which communicates with the national instrument controller (NI-852) to send control bits to the IC. The IC is powered by ROHDE&SCHWARZ NGE 100 DC power supply. The

measurement instrument is the Keysight N5247B PNA-X vector network analyzer which measures the S-parameters of the IC. The measured S-parameters are then sent to the PC and read by the calibration algorithm.

BFIC2 Calibration Setup

For the BFIC calibration demonstrated in this section, the maximum targeting gains are calculated without the proposed gain tapering awareness. To demonstrate the efficacy of the two proposed calibration routines. We benchmark them against the most accurate calibration method "Exhaustive Search" and the "No Calibration" method which is to input the gain and phase indexes directly with no look-up-table.

Note that for the "No Calibration" method, to keep the scenario realistic, the phase and magnitude of the control state with the phase index of 1 and the maximum gain is referenced as the 0 phase and the maximum targeting gain for the calibration. Also, the gain tuning setting is guided by the least-significant-bit (LSB) specified in the datasheet.

Figure 3.34 below shows the single-channel full measurement of the BFIC2 for the exhaustive search method. We can see the number of available states is significantly less than the BFIC1 shown in figure 3.31 which means the calibration has significantly less room to select the states for the targeting points. We also see that the constellation of BFIC2 is less continuous than the constellation of BFIC1, which hints at regional unpredictability and reduced efficacy of the proposed characterization method.

To characterize the BFIC2, we choose an outline data sampling size of 10 and a gain data sampling size of 4 for the optimal calibration FOM which means only 24 measurements are needed for the characterization. The supervised routine uses a validation tolerance coefficient T of 2 which means the validated points are at least reaching exactly what's needed to satisfy the targeting phase and gain resolution.

It is important to clarify that, in order to show the calibration performance of the proposed unsupervised routine, test measurements need to be done for us to evaluate the gain and phase errors of each of its solved gain and phase indexes. Those test measurements are not performed in the practical operation of the unsupervised calibration routine.

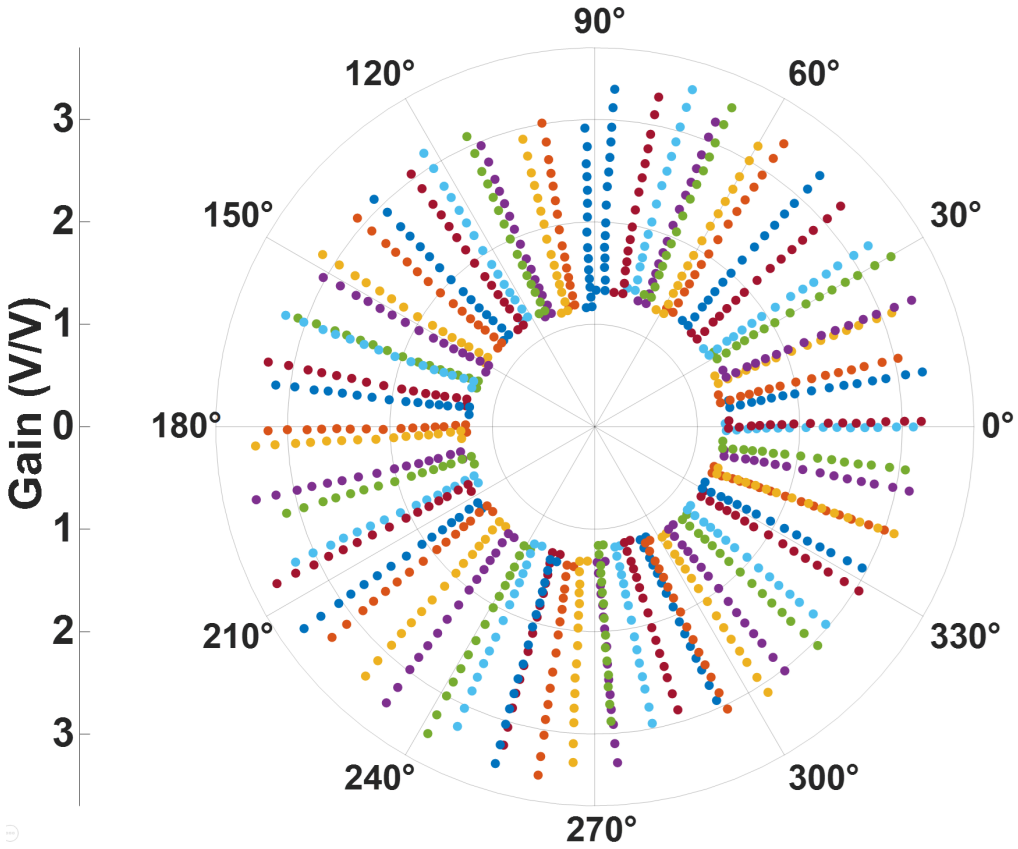


Figure 3.34: BFIC2 single-channel full measurement.

BFIC2 Calibrated Constellation Comparison

Figure 3.35 below shows the calibrated constellation of the BFIC2 using two benchmarking methods and two proposed methods. The calibration in figure 3.35 targets 64 phase states (native phase resolution), 8 gain states with 1dB gain tuning resolution. Calibration results targeting different constellation settings are included in the table 3.2 below.

From the calibrated constellations in Figure 3.35 below, it is clear that all calibration methods cannot give excellent results since the BFIC2 is unable to produce measurement positions near some of the targeting positions. The exhaustive search method gives the best possible constellation whereas the no calibration method exhibits significant errors and is the worst by far. The two proposed calibration routines, although has limited room for action, still work as intended in that they approach the result of the exhaustive search

while using a fraction of the measurements. We can see from Figure 3.35c and 3.35d that the proposed methods have the gain under control versus phase, unlike the no calibration method.

Note that the magnitude of the constellation without calibration is slightly higher than the calibrated constellations since the calibration needs to sacrifice the gain in some of the directions to ensure gain-invariant phase tuning and this is ensured by the maximum targeting gain condition in (3.48).

Comparing the supervised and unsupervised constellations, we see that the supervised constellation is cleaner and has no significant point errors (observe the points in the lowest gain states), which demonstrates the fail-safe nature of the supervised routine. The calibration of the BFIC2 shows the value of the supervised routine in that it gives results comparable to the exhaustive search regardless of how predictable the constellation is while taking equal or fewer measurements depending on the targeting states. The unsupervised constellation, although has slightly higher errors than the supervised constellation, is still much better than the constellation without calibration.

From the calibrated constellations, we can conclude that the BFIC2 needs calibration for deployment in an array. In addition to the sub-optimal single-channel calibration performance, if the BFIC2 is to be used in a phased array, it is also going to suffer from the phase and gain response difference between the different channels, which our characterization method automatically corrects.

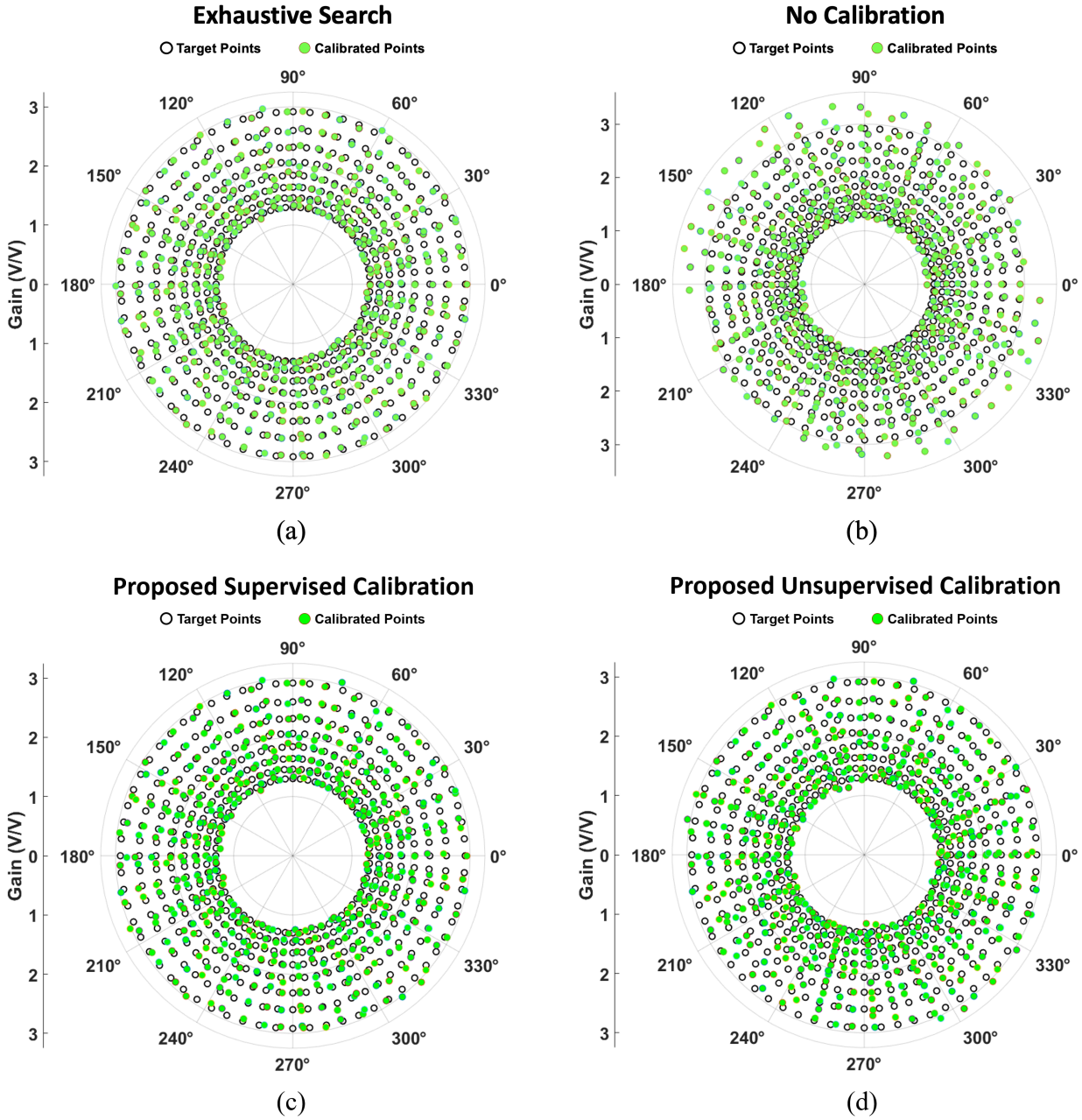


Figure 3.35: Calibrated targeting constellation on BFIC2 using different calibration methods. Targeting 64 phase states, 8 gain states with 1dB gain tuning resolution. Proposed characterization method using outline data sampling size of 10 and gain data sampling size of 4. (a) Exhaustive search; (b) No calibration; (c) Proposed supervised calibration; (d) Proposed unsupervised calibration.

Table 3.2: BFIC2 calibration results comparison. Characterized using an outline data sampling size of 10 and a gain data sampling size of 4. The supervised routine has the validation tolerance coefficient set to 2.

	Exhaustive Search	**Supervised**	**Unsupervised**	**No Calibration**
Target 4-bit phase, 8 gain states with 1dB gain tuning resolution				
Phase RMSE (°)	1.68	1.70	2.22	2.13
Peak Phase Error (°)	3.77	3.77	7.31	6.04
Gain RMSE (dB)	0.15	0.21	0.36	0.74
Peak Gain Error (dB)	0.31	0.50	1.04	1.48
EVM (%)	3.20	3.84	5.04	9.62
# of Measurements	1024	239	24	0
Calibration Time	382.8s	91.8s	9.1s	0
Target 5-bit phase, 8 gain states with 1dB gain tuning resolution				
Phase RMSE (°)	1.52	1.61	2.10	2.42
Peak Phase Error (°)	4.06	4.06	7.31	7.21
Gain RMSE (dB)	0.16	0.21	0.34	0.65
Peak Gain Error (dB)	0.49	0.50	1.04	1.40
EVM (%)	3.01	3.62	4.70	8.72
# of Measurements	1024	412	24	0
Calibration Time	382.8s	156.7s	9.3s	0
Target 6-bit phase, 8 gain states with 1dB gain tuning resolution				
Phase RMSE (°)	1.98	2.00	2.67	3.51
Peak Phase Error (°)	4.12	4.12	7.40	10.22
Gain RMSE (dB)	0.17	0.17	0.35	0.67
Peak Gain Error (dB)	0.54	0.50	1.10	1.49
EVM (%)	3.64	3.74	5.42	10.19
# of Measurements	1024	849	24	0
Calibration Time	382.8s	317.8s	9.5s	0
Target 6-bit phase, 14 gain states with 0.5dB gain tuning resolution				
Phase RMSE (°)	2.02	2.03	2.67	3.56
Peak Phase Error (°)	4.13	4.30	7.40	10.22
Gain RMSE (dB)	0.16	0.17	0.35	0.68
Peak Gain Error (dB)	0.48	0.73	1.10	1.49
EVM (%)	3.64	3.64	5.38	10.24
# of Measurements	1024	952	24	0
Calibration Time	382.8s	358.6s	9.6s	0

BFIC2 Calibration Results Comparison

Table 3.2 presents the calibration results comparing different methods for various numbers of phase and gain states. The proposed supervised routine yields results closely approaching those of the exhaustive search method while requiring fewer measurements. The unsupervised routine, though introducing slightly higher errors, greatly reduces the number of measurements needed. In stark contrast, the no calibration method consistently exhibits the poorest performance, with EVMs averaging around 9.7% across all cases, indicating that the BFIC2 is unsuitable for operation without calibration.

Due to the limited points in the constellation of the BFIC2, calibration performance across different target resolutions is less consistent than that of the BFIC1. The discontinuities present in the constellation shown in Fig. 3.34 lead to discontinuous mapping functions and less effective characterization.

Despite this, the efficiency of the proposed unsupervised calibration is noteworthy. Utilizing only 24 measurements, the unsupervised calibration achieves an EVM that is half of that of the calibration-free method. This 40-fold reduction in the number of measurements compared to the exhaustive search is significant, although it pales in comparison to the 1100-fold reduction observed with the BFIC1, which features much higher resolution gain and phase tuning. This disparity underscores that the optimal characterization sampling size for best calibration FOM does not scale linearly with BFIC resolution. The proposed unsupervised calibration routine demonstrates a greater advantage when calibrating higher-resolution BFICs.

For the unsupervised calibration, the achieved EVM—accounting for both gain and phase errors—is consistently about 1.5% higher than that of the exhaustive search method. This is due to the less predictable constellation and limited degree of freedom within the low-resolution constellation. As targeting resolutions increase, the margins for gain and phase errors become smaller, exacerbating the proportional errors needed to meet the target resolution. For instance, when targeting 6-bit phase and 16 gain states with 0.5dB gain resolution, phase RMSE and gain RMSE must be below 2.81 degrees and 0.25dB, respectively, for the achieved points to be distinguishable. In this high-resolution setting, our unsupervised calibration achieves phase RMSE and gain RMSE of 2.67 degrees and 0.35dB, respectively, failing the gain error requirement. Here, the supervised routine excels by individually validating each calibrated point, significantly reducing peak errors compared to the unsupervised calibration.

The supervised calibration acts as a fail-safe for the unsupervised calibration, actively verifying every solution. This fail-safe nature is evident in the substantial reductions in

peak phase and gain errors observed when transitioning from unsupervised to supervised calibration. The supervised routine is designed to improve every metric of the unsupervised routine where possible and necessary to meet validation criteria, albeit at the cost of performing a number of measurements at least equal to the number of target points.

The measurement savings of the supervised routine are less pronounced, particularly when targeting phase resolutions of 5-bit and above, as the targeting states cover nearly the entire available constellation. As the resolution increases, the validation region shrinks, causing the adaptive kernel search algorithm to require more iterations and larger kernel sizes to find a solution. This contributes to a rapid increase in the number of measurements. In all scenarios, the supervised calibration strikes a balance between the calibration results and the number of measurements, positioned between the exhaustive search and the unsupervised calibration.

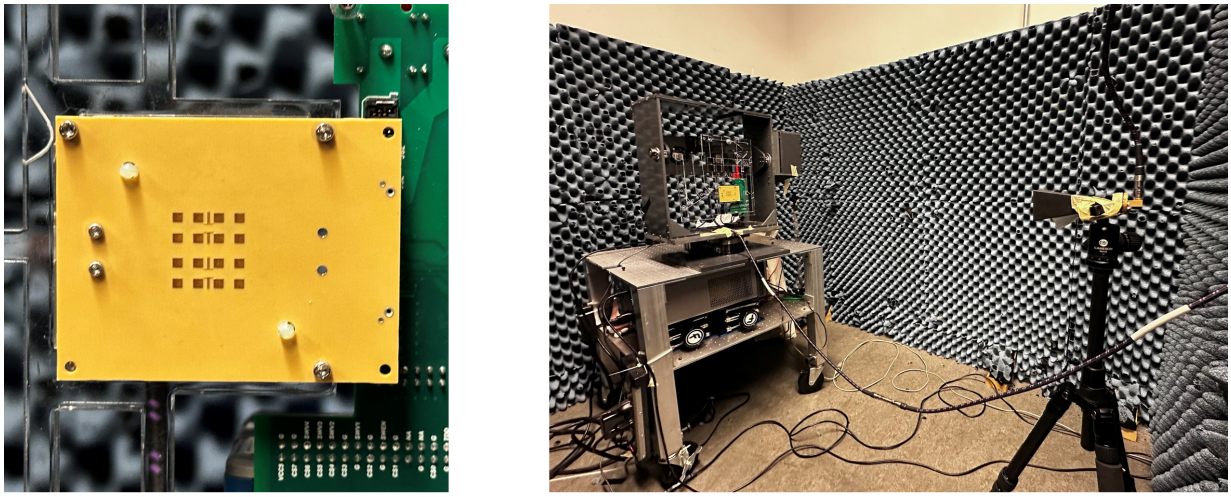
3.4.3 4×4 BFIC1 Array Calibration

4×4 BFIC1 Array Measurement Setup

Figure 3.36 below shows the array and the measurement setup. The measurement is conducted in the far-field with the array mounted on a horizontally rotating motor, pointing at a horn antenna. The algorithm runs in MATLAB on a PC, which communicates with the National Instruments controller (NI-852) to send control bits to the BFICs on the array. The array is powered by a ROHDE & SCHWARZ NGE 100 DC power supply. The measurement instrument, a Keysight N5247B PNA-X vector network analyzer, measures the S-parameters of the link from the array to the horn antenna. During calibration, each array channel is turned on individually while the other channels are turned off. The measured S-parameters are then sent to the PC and processed by the algorithm.

4×4 BFIC1 Array Calibration Setup

The array targeting gains are set using both the typical discrete gain states method and the proposed taper-aware method to demonstrate the effect of gain tapering on the radiation pattern. For the "No Taper" scenario, the array utilizes the maximum gain states of the calibrated discrete gain states. In the "Forced Taper" scenario, the array applies a taper using the calibrated discrete gain states. For the "Taper Aware" scenario, the array directly targets the desired gains as described in (3.49).



(a) (b)

Figure 3.36: Measurement setup for 4×4 BFIC1 array: (a) Array close up; (b) Setup picture.

The taper used in this calibration is the Taylor window taper targeting side-lobe level (SLL) of -17.7 dB. The proposed characterization method uses an outline data sampling size of 23 and a gain data sampling size of 8. The supervised routine uses a validation tolerance coefficient T of 10 for stringent validation.

4×4 BFIC1 Array Constellation Performance

From Table 3.3, we can see that the constellation performance of the two proposed calibrations approaches the result of the exhaustive search while requiring significantly fewer measurements. The constellation without calibration exhibits substantially higher errors, which are even greater than the no-calibration result of the BFIC in Table 3.1, demonstrating the effects of the response differences among the various array elements.

Compared to the BFIC constellation results in Table 3.1, we observe that the unsupervised calibration incurs a penalty in achieved EVM due to the increased randomness present in array over-the-air (OTA) measurements. However, the results of the exhaustive search and the supervised calibration remain consistent with the BFIC calibration results, demonstrating their robustness.

The efficacies of the proposed calibrations are noteworthy. The unsupervised calibration

demonstrates its excellent efficiency by completing the calibration in just over 5 minutes compared to the 7 days required by the exhaustive search method while achieving excellent results. The supervised calibration demonstrates its robustness by achieving virtually identical results to the exhaustive search method while only taking 3 hours.

Table 3.3: 4x4 BFIC1 array calibration results comparison.

	Exhaustive Search	**Supervised**	**Unsupervised**	**No Calibration**
Target 6-bit phase, 8 gain states with 1dB gain tuning resolution				
Phase RMSE (°)	0.41	0.41	0.63	18.30
Gain RMSE (dB)	0.03	0.03	0.05	2.76
EVM (%)	0.76	0.80	1.18	53.51
# of Measurements	1048576	19100	928	0
Calibration Time	7d	3h	331.7s	0

4×4 BFIC1 Array Radiation Pattern

In this subsection, the effects of the proposed calibration methods on the array radiation pattern are experimentally validated and compared to the exhaustive search method. Figure 3.37 shows the measured array radiation patterns. Specifically, Figure 3.37a and Figure 3.37b present the radiation patterns at the board side. Figure 3.37c compares the board side radiation patterns calibrated using the unsupervised routine with three different gain tapering solutions. Lastly, Figure 3.37d illustrates the beam-steered radiation patterns for all calibration methods with gain tapering.

To ensure the measured radiations reflect the theoretical gain tapering assumption that the array elements are isotropic, the radiations in Figures 3.37a, 3.37b, and 3.37c are measured with a fixed motor position while the beam is electrically steered. The beam-steered radiation pattern in Figure 3.37d is measured using the mechanically rotating motor.

For all scenarios, the radiation patterns of the two proposed methods remain virtually identical to the exhaustive search method, demonstrating their excellent calibration accuracy. The slight imbalance in the calibrated radiation patterns could be due to their passive calibration nature, which omits the effects of dynamic current loading and active antenna couplings. As indicated by the findings in [5], this imbalance in passive calibration can be

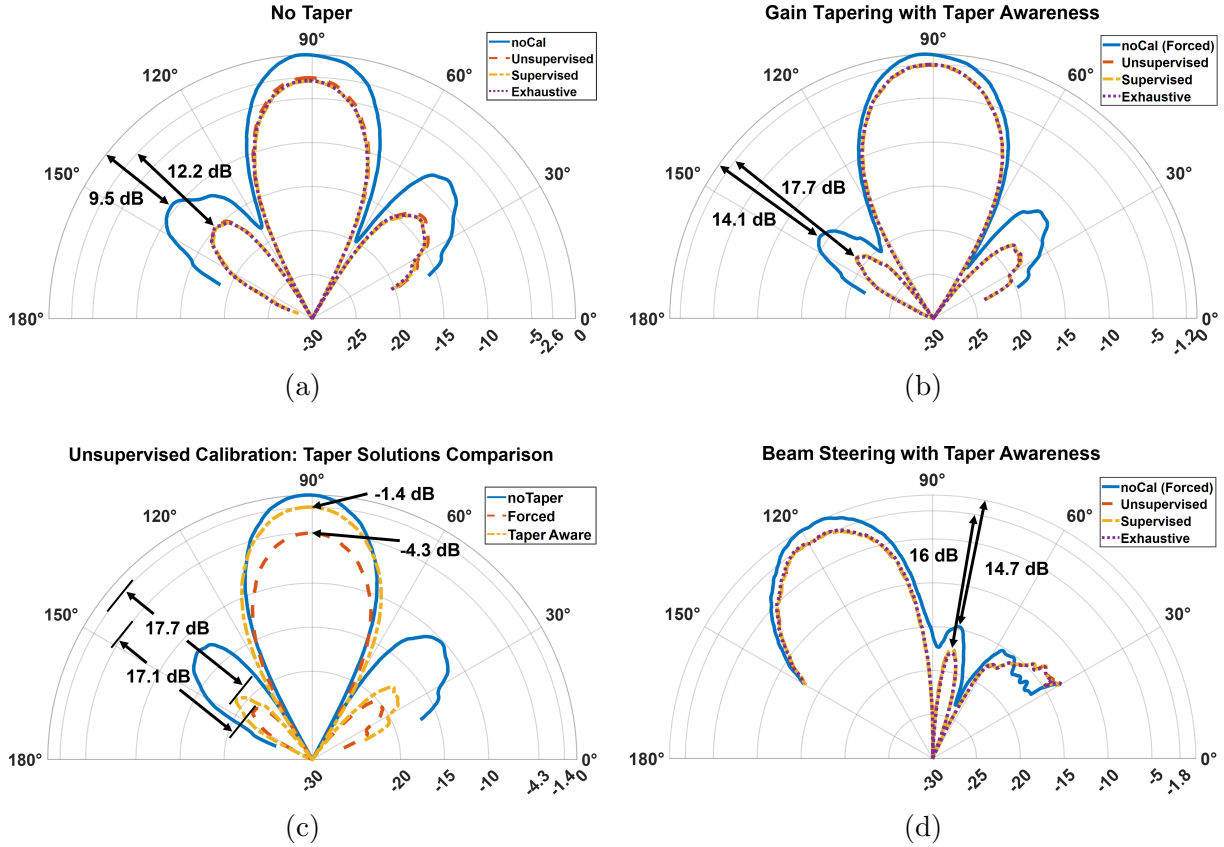


Figure 3.37: Measured radiation pattern of the 4x4 BFIC1 array: (a) No taper; (b) Gain tapering with taper awareness; (c) Unsupervised calibration comparing taper solutions; (d) Beam steering.

corrected in active calibration, where the array is calibrated using the proposed methods with all elements turned "ON".

In the no taper scenario shown in Figure 3.37a, the "noCal" method, corresponding to no calibration, exhibits the highest power but the worst SLL of -9.5 dB and the shallowest nulls. The other calibration methods overlap, demonstrating better SLL of -12.2 dB and significantly deeper nulls. This shows that array calibration involves sacrificing gain to improve phase accuracy.

For the tapered scenario shown in Figure 3.37b, all the calibrated radiations align and have a reduced SLL of -17.7 dB, matching the theoretical value. The "noCal" method, not compatible with gain taper awareness, applies a "forced" taper on the array's gain states.

The “noCal” radiation achieves an SLL of -14.1 dB, which is reduced compared to the no taper scenario but significantly deviates from the theoretical -17.7 dB.

Comparing the effects of different gain tapering solutions (no taper, forced taper, and taper aware), Figure 3.37c shows the radiation of the unsupervised calibration using these solutions. The no taper solution has the highest gain at the main lobe but the worst SLL. The taper aware method achieves 2.9 dB higher gain than the forced taper method, validating the promise of taper awareness as proposed in Section 3.2.8. The SLL of the taper aware method matches the theoretical -17.7 dB, while the forced taper, experiencing quantization errors from discrete targeting gain states, achieves an SLL of -17.1 dB.

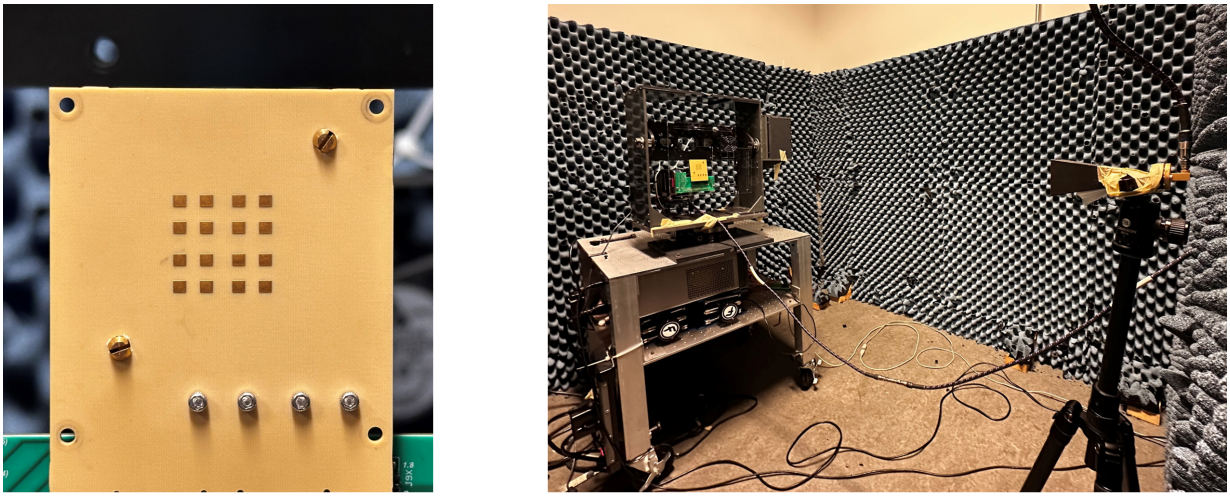
For demonstrating beam-steering, Figure 3.37d shows the mechanically-steered radiation of all methods with the beam steered to -30 degrees. The calibrated radiations of all methods remain consistent while steered, exhibiting excellent pointing accuracy but a deteriorated SLL compared to the radiation pointed at the board side. As expected, the “noCal” method has the worst SLL and the shallowest nulls.

3.4.4 4×4 BFIC2 Array Calibration

Figure 3.36 below shows the array and the measurement setup. The measurement is conducted in the far-field with the array mounted on a horizontally rotating motor, pointing at a horn antenna. The algorithm runs in MATLAB on a PC, which communicates with the National Instruments controller (NI-852) to send control bits to the BFICs on the array. The array is powered by a ROHDE & SCHWARZ NGE 100 DC power supply. The measurement instrument, a Keysight N5247B PNA-X vector network analyzer, measures the S-parameters of the link from the array to the horn antenna. During calibration, each array channel is turned on individually while the other channels are turned off. The measured S-parameters are then sent to the PC and processed by the algorithm.

4×4 BFIC2 Array Calibration Setup

The array targeting gains are set using both the typical discrete gain states method and the proposed taper-aware method to demonstrate the effect of gain tapering on the radiation pattern. For the “No Taper” scenario, the array utilizes the maximum gain states of the calibrated discrete gain states. In the “Forced Taper” scenario, the array applies a taper using the calibrated discrete gain states. For the “Taper Aware” scenario, the array directly targets the desired gains as described in (3.49).



(a) (b)

Figure 3.38: Measurement setup for 4×4 BFIC2 array: (a) Array close up; (b) Setup picture.

The taper used in this calibration is the Taylor window taper targeting side-lobe level (SLL) of -15.8 dB. The proposed characterization method uses an outline data sampling size of 10 and a gain data sampling size of 4. The supervised routine uses a validation tolerance coefficient T of 2.

4×4 BFIC2 Array Constellation Performance

From Table 3.4, we can see the constellation performance of the two proposed calibrations compared to the results of the exhaustive search and no calibration. The constellation without calibration exhibits substantially higher errors, even greater than the no-calibration result of the BFIC in Table 3.2, demonstrating the effects of response differences among the various array elements.

Compared to the BFIC constellation results in Table 3.2, we observe that the unsupervised calibration incurs a penalty in achieved EVM due to increased randomness present in array over-the-air (OTA) measurements. However, the results of the exhaustive search and the supervised calibration remain consistent with the BFIC calibration results, demonstrating their robustness.

The efficacies of the proposed calibrations are noteworthy. The unsupervised calibration

Table 3.4: 4x4 BFIC2 array calibration results comparison.

	Exhaustive Search	**Supervised**	**Unsupervised**	**No Calibration**
Target 6-bit phase, 8 gain states with 1dB gain tuning resolution				
Phase RMSE (°)	1.96	1.98	2.70	10.37
Gain RMSE (dB)	0.17	0.18	0.43	2.19
EVM (%)	3.68	3.75	6.08	27.21
# of Measurements	16384	5774	384	0
Calibration Time	1h 22m	29m	117s	0

demonstrates its efficiency by completing the calibration in just under 2 minutes, compared to the 1 hour and 22 minutes required by the exhaustive search method. While the constellation result of the unsupervised calibration is not close to the exhaustive search method, it is still much better than no calibration. The supervised calibration demonstrates its robustness by achieving virtually identical results to the exhaustive search method while only taking half an hour.

4×4 BFIC2 Array Radiation Pattern

In this subsection, the effects of the proposed calibration methods on the array radiation pattern are experimentally validated and compared to the exhaustive search method. Figure 3.39 shows the measured array radiation patterns. Specifically, Figure 3.39a and Figure 3.37b present the radiation patterns at the board side. Figure 3.39c compares the board side radiation patterns calibrated using the unsupervised routine with three different gain tapering solutions. Lastly, Figure 3.39d illustrates the beam-steered radiation patterns for all calibration methods with gain tapering.

To ensure the measured radiations reflect the theoretical gain tapering assumption that the array elements are isotropic, the radiations in Figures 3.39a, 3.39b, and 3.39c are measured with a fixed motor position while the beam is electrically steered. The beam-steered radiation pattern in Figure 3.39d is measured using the mechanically rotating motor.

For all scenarios, the radiation patterns of the proposed supervised calibration remain virtually identical to the exhaustive search method, while the proposed unsupervised calibration closely follows the exhaustive search method. This demonstrates the accuracy of the proposed methods, particularly highlighting the robustness of the proposed supervised

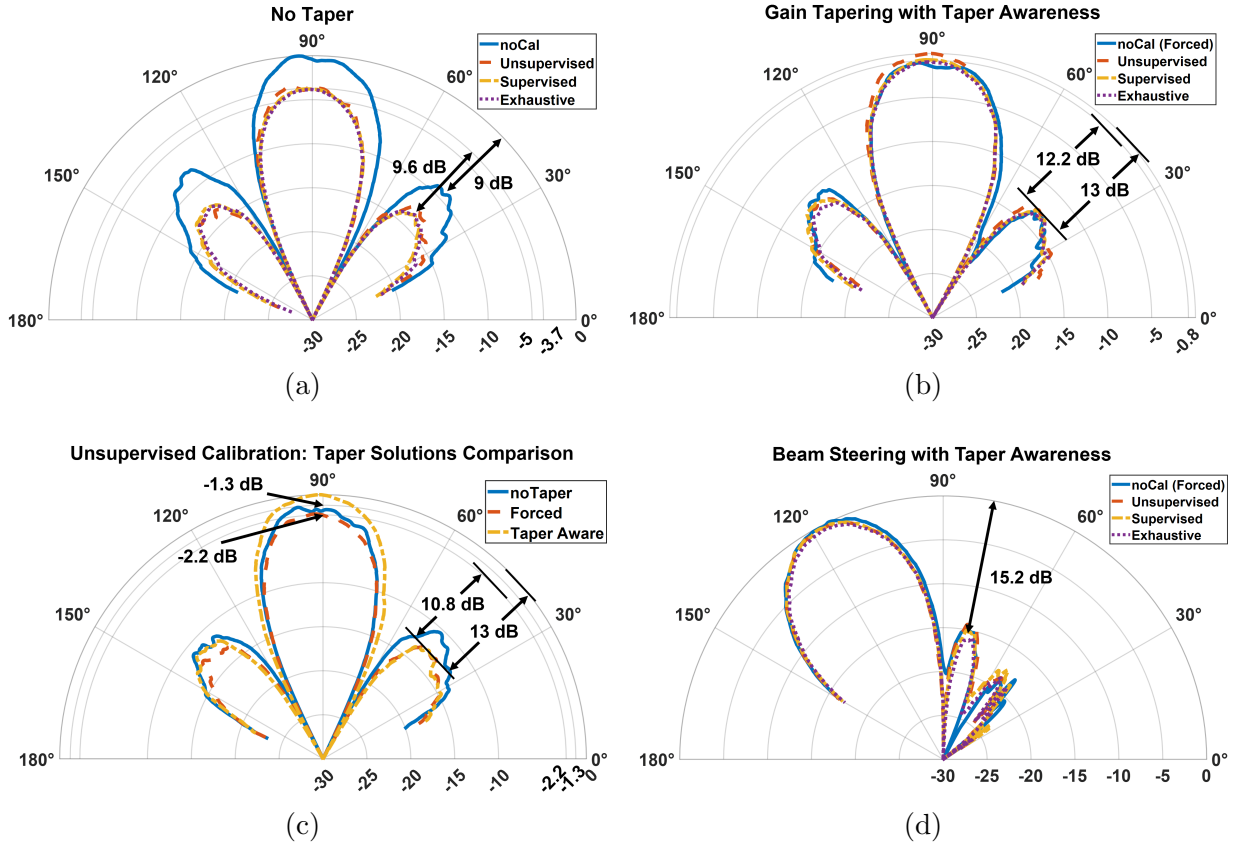


Figure 3.39: Measured radiation pattern of the 4x4 BFIC2 array: (a) No taper; (b) Gain tapering with taper awareness; (c) Unsupervised calibration comparing taper solutions; (d) Beam steering.

calibration.

The slight imbalance in the calibrated radiation patterns could be due to their passive calibration nature, which omits the effects of dynamic current loading and active antenna couplings. As indicated by the findings in [5], this imbalance in passive calibration can be corrected in active calibration, where the array is calibrated using the proposed methods with all elements turned "ON".

In the no taper scenario shown in Figure 3.39a, the "noCal" method, corresponding to no calibration, exhibits the highest power but the worst SLL of -9 dB and the shallowest nulls. The other calibration methods overlap, demonstrating better slightly SLL of -9.6 dB and significantly deeper nulls. This shows that array calibration involves sacrificing gain

to improve phase accuracy.

For the tapered scenario shown in Figure 3.39b, all the radiation patterns roughly align, with the radiation from the unsupervised calibration peaking slightly higher than the other methods and achieving a slightly better reduced SLL of -13 dB compared to the -12.2 dB of the other methods. Note that the achieved SLL of all methods significantly deviates from the theoretical -15.8 dB. This is due to significant power variations between elements in the BFIC2 array, and its BFIC's limited gain tuning range causes the targeted gain states to be clipped, preventing the desired taper from being produced accurately.

The "noCal" method, not compatible with gain taper awareness, applies a "forced" taper on the array's gain states. Unlike the result in the BFIC1 array shown in Figure 3.37b, the "noCal" radiation pattern of the BFIC2 array has gain in line with the other methods. This is because the BFIC2 array's middle elements have the lowest maximum gain, and the higher gains of the other elements are not pronounced when a taper is applied.

Comparing the effects of different gain tapering solutions (no taper, forced taper, and taper aware), Figure 3.39c shows the radiation of the unsupervised calibration using these solutions. The taper aware method achieves 2.2 dB higher gain than the forced taper method, validating the promise of taper awareness as proposed in Section 3.2.8. The -13 dB SLL of the taper aware method is better than the -10.8 dB SLL of the forced taper method, demonstrating the quantization error and extended targeting gain clipping experienced by the forced taper method. The no taper solution, apart from having the worst SLL, has lower gain at the main lobe than the taper aware method. Unlike the BFIC1 array shown in Figure 3.37c, this is caused by the large power variations between elements in the BFIC2 array.

For demonstrating beam-steering, Figure 3.39d shows the mechanically-steered radiation pattern of all methods with the beam steered to -30 degrees. The calibrated radiations of all methods remain consistent while steered, exhibiting excellent pointing accuracy and a lower SLL of -15.2 dB compared to the radiation pointed at the board side. The "noCal" method has about the same SLL as the other calibrated radiation patterns but exhibits the shallowest nulls close to the main lobe.

3.5 Remarks

From the experimental results in Section 3.4, we see that the two proposed calibration routines achieve calibrated constellations and array radiation patterns approaching those of the exhaustive search method while requiring significantly fewer measurements. Comparing

the calibration results of the two arrays, it is evident that the advantages of the proposed methods are more pronounced when the arrays have higher resolution and more continuous constellations.

It can also be concluded that having array elements with a greater native gain tuning range is crucial for correcting the power differences between the elements in the array and accurately producing the desired gain taper. The proposed taper aware method for setting the targeting gains for a desired taper demonstrates higher power and more accurate tapering compared to the forced taper, as it is less sensitive to targeting gain quantization errors and experiences delayed gain clipping when the taper extends beyond the array's gain tuning range.

Chapter 4

Channel Transformation and Similarity Sequencing Techniques for Intelligent Phased Array Calibration

Using our proposed characterization method, described in chapter 3 above, already significantly speeds up the phased array calibration. As demonstrated in the testing of the 4×4 BFIC1 array and using our proposed unsupervised calibration routine, the number of measurements needed for array calibration is reduced by more than 1100 times compared to the state-of-the-art exhaustive search method, speeding up the calibration that would take more than 7 days to less than 5 minutes, all while providing virtually identical beamforming performance in the measured radiation patterns.

However, further improvement is possible for array calibration. Figure 4.1 below shows the full measurements of all 16 channels of the 4×4 BFIC1 array. We observe that the shape of the constellations from one element to another does not significantly change. In general, the array elements should have similar responses if they are using the same BFIC. Using our proposed characterization method, this similarity in the channel responses translates to similar shapes in the mapping functions between channels as demonstrated in figure 4.4 below. Thus, instead of acquiring the characterization dataset of every channel individually, it is feasible to transfer captured information from one channel to another.

We describe the process of transferring the captured information between channels as "channel transformation" and we do this by transforming the generated mapping functions. From chapter 3 above, we see that our defined mapping functions fully and accurately describe the channel response and give excellent calibration results. The objective of

channel transformation is to synthesize the mapping functions for a targeting channel as accurately as possible without acquiring the full characterization dataset, shown in figure 3.8, thereby achieving extra savings on the number of measurements for array calibration.

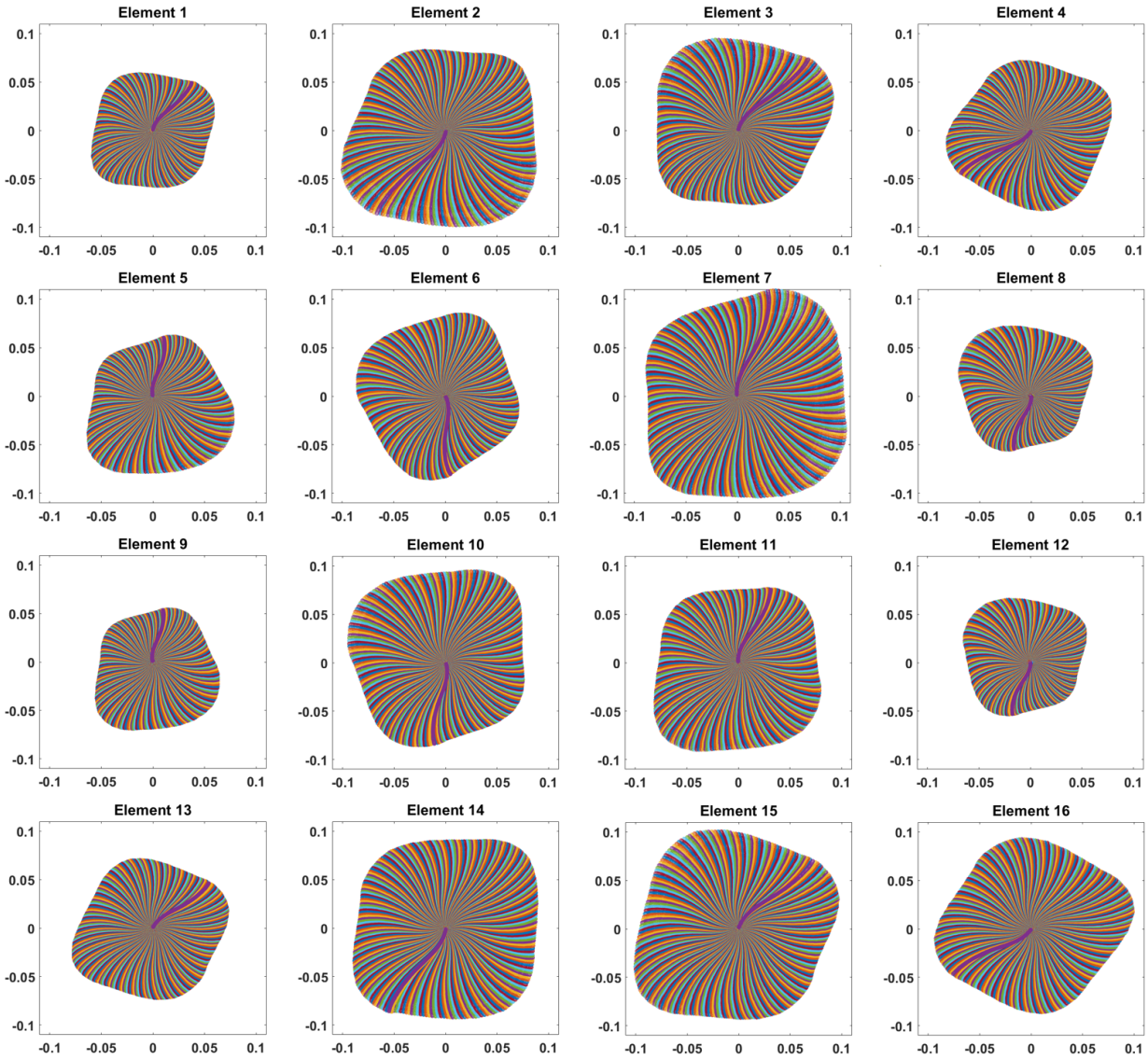


Figure 4.1: Full 16 channels far-field measurements for 4×4 BFIC1 array. Measurement for a specific element is done in the far-field with the other elements turned "OFF". Plots are scaled preserving the received power level and the x-axis and y-axis show the real and imaginary parts of the transmission coefficient, respectively.

4.1 Overview

Channel transformation investigates the potential similarities in mapping functions across different channels within an array. As observed from the main mapping functions of channel 5 and channel 4 of the 4×4 BFIC1 array in figure 4.4 below, the mapping functions across channels exhibit similar shapes except for the gain envelope. Taking a similar approach to the proposed characterization method but rather than transforming the mapping functions across the different regions in the constellation accounting for the variations within the channel, we transform them across channels accounting for the power difference and phase offset between the different channels in the array. Then, the characterization method will take care of transforming the synthesized mapping functions across the different regions in the targeting constellation.

Once a channel in the array is fully characterized using the proposed characterization method, it is designated as the "reference channel" and possesses the complete "reference mapping functions." The proposed channel transformation technique transfers these reference mapping functions from the "reference channel" to the "targeting channel." This process utilizes the reference mapping function along with a subset of the characterization dataset acquired in the targeting channel, known as the "transformation dataset," to synthesize the mapping function of the targeting channel, accurately describing its response.

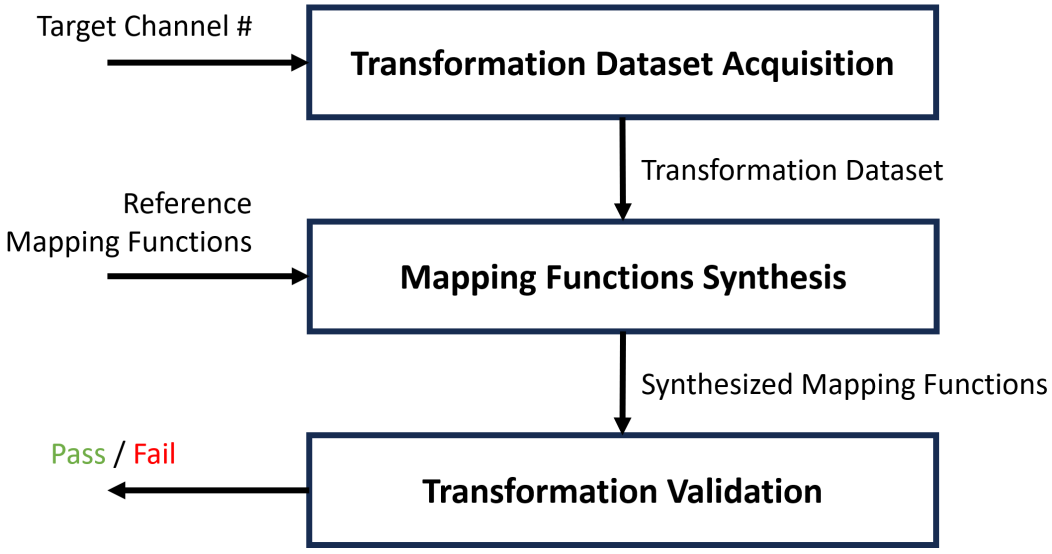


Figure 4.2: Top-level flow chart of the channel transformation process.

The top-level and partial flow chart of the channel transformation process is shown in figure 4.2 below. With a target channel, the algorithm acquires the transformation dataset, illustrated in figure 4.3 below, which along with the reference mapping functions allows the algorithm to calculate the variations in the channel response between the reference channel and the targeting channel. The algorithm then uses this inter-channel variation to adjust the reference mapping functions in a process called "mapping functions synthesis", so that the synthesized mapping functions, which maintain the characteristics of the reference channel, now describe the targeting channel.

Due to the uncertainty in channel responses that exist between channels, a fail-safe mechanism called "transformation validation" is in place to avoid catastrophic beamformer failure. The transformation validation process tests the performance of synthesized mapping functions on the targeting channel using the distance criterion introduced in the supervised routine in section 3.3.3 above. The algorithm handles the validation result, whether it "passes" or "fails", in a higher entity that controls the overall flow of the channel transformation. The complete flow diagram of the channel transformation process is shown in figure 4.6.

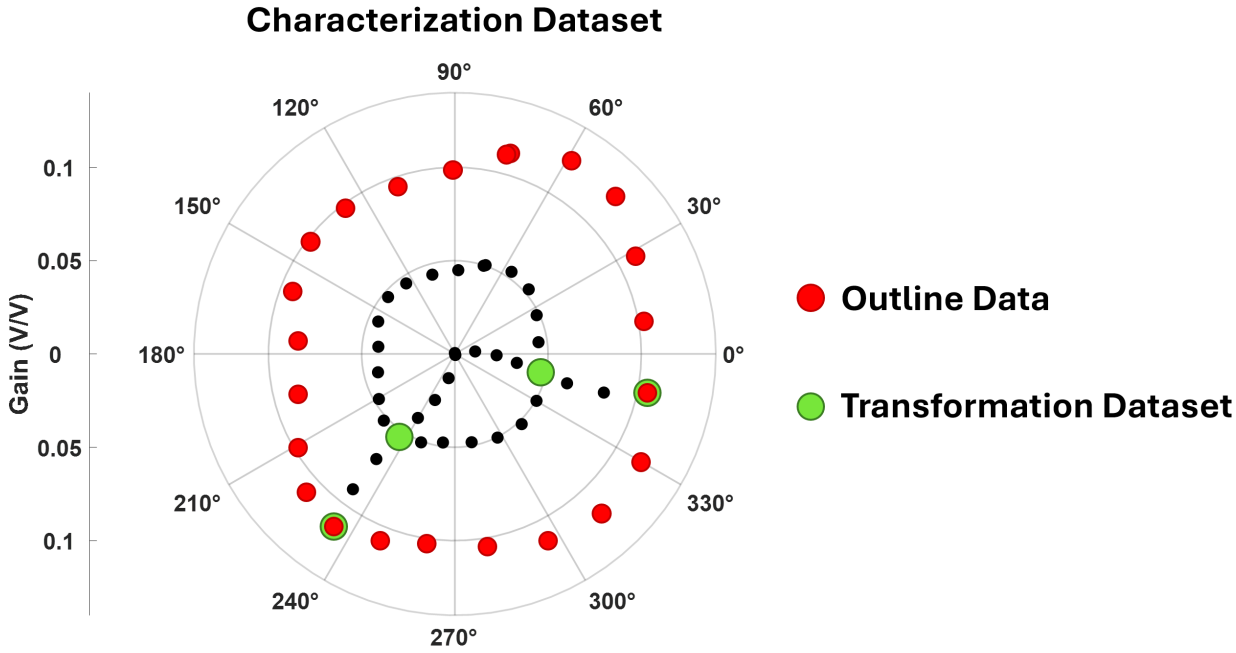


Figure 4.3: Demonstration showing the subset of the characterization dataset used for channel transformation.

Among all the mapping functions defined in the proposed characterization method, the gain envelope, which represents the maximum gains enclosing the channel constellation, uniquely captures the distortion in the constellation shapes of different channels. Figure 4.4 below shows the main mapping functions of channel 5 and channel 7. These figures confirm that, unlike other mapping functions, the gain envelope exhibits unpredictable variation across channels. This unpredictability and its ability to encapsulate the constellation shape information make the gain envelope nontransferable. However, this very characteristic makes it an excellent candidate for channel identification.

Exploiting this characteristic is a process called "Array Elements Similarity Sequencing", which identifies the best pairs of reference and target channels for the highest transformation success rate. By sequencing the channels in order of constellation similarity, achieved by extracting information from the channels' gain envelope, channel transformation becomes more deliberate and successful more often. As demonstrated in the flow chart in figure 4.6, similarity sequencing determines which channel becomes the reference and which channel is to be transformed using which reference. In other words, similarity sequencing is the brain, and channel transformation is the tool, enabling intelligent phased array calibration.

In order to sequence the array accurately and determine the maximum targeting gain, the outline data for each channel must be precise. This data, acquired in addition to the transformation dataset, ensures the most accurate gain envelope and phase profile. Depending on the outline data sampling size, fully acquiring this data for each element can significantly increase the number of measurements needed for channel transformation. Since the main objective is to ensure similarity sequencing, the gain envelope needs to be sampled sufficiently to capture most of its variation features.

"Dynamic Sampling" is a process that determines the minimum outline data sampling size necessary to ensure the correct function of similarity sequencing. By analyzing the gain envelope, it identifies the sampling size required to capture the majority of the frequency contents within the gain envelope, allowing for the reconstruction of the original upsampled outline data via interpolation.

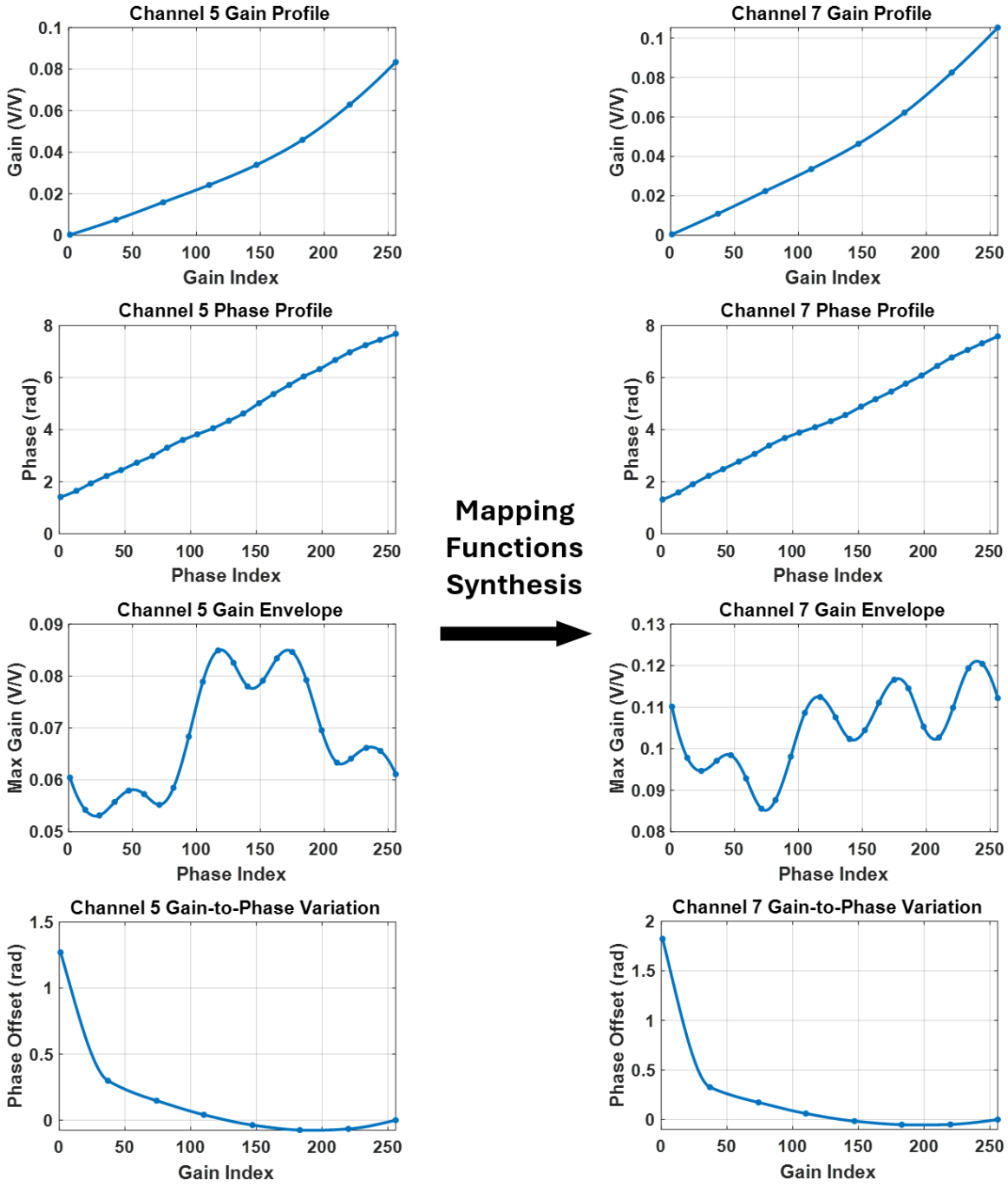


Figure 4.4: Mapping functions synthesis demonstration for the 4×4 BFIC1 array. Demonstrating the synthesis of the four main mapping functions from channel 5 to channel 7.

Figure 4.5 illustrates the composite mapping functions of channel 5 and channel 7. This figure demonstrates that the periodic series, namely the gain envelope scaling profile ($GESP$) and the phase profile shifting profile ($PPSP$), experience phase shifts across different channels. This detail is important to consider as we discuss the process of mapping function synthesis in subsequent sections.

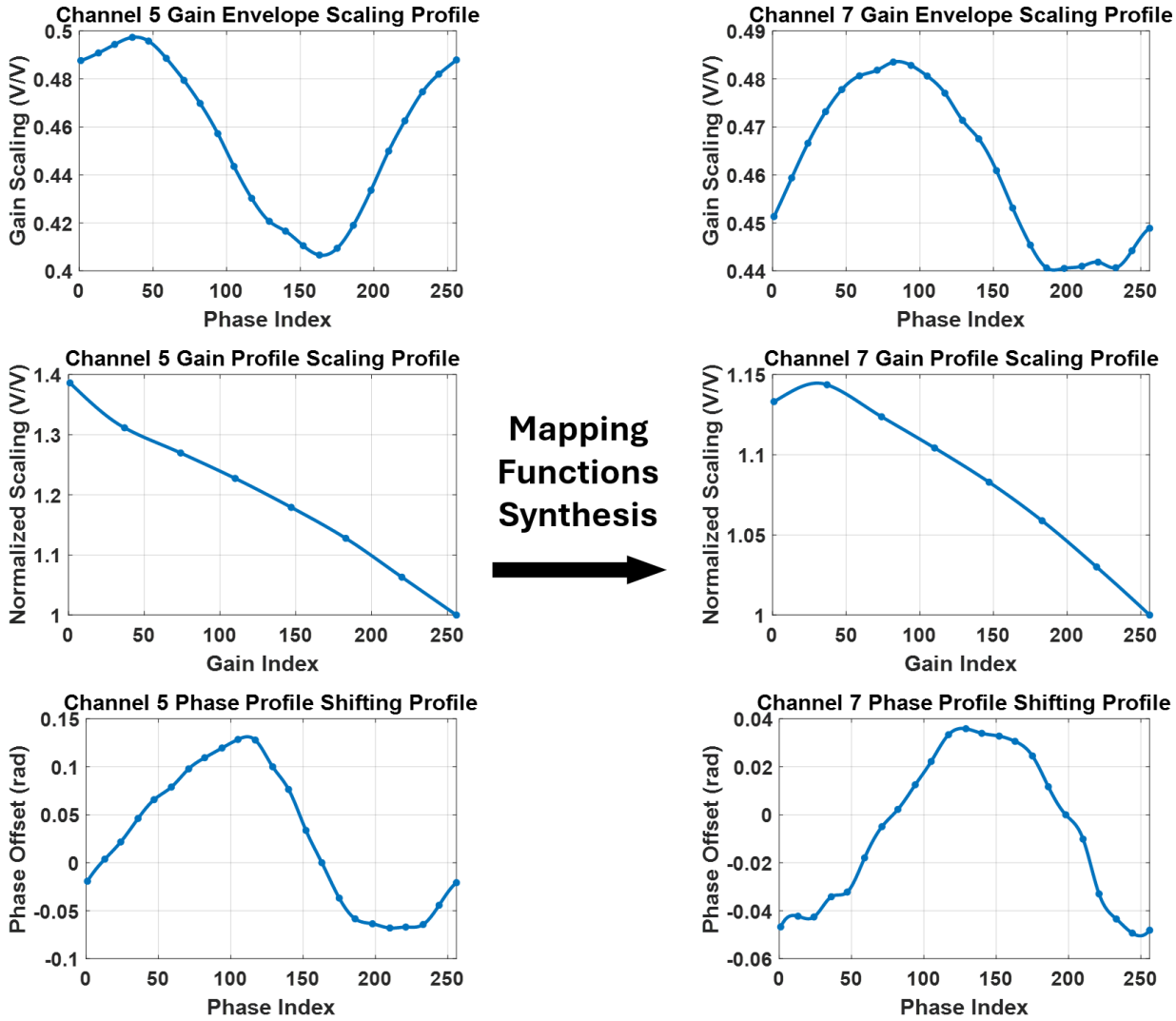


Figure 4.5: Mapping functions synthesis demonstration for the 4×4 BFIC1 array. Demonstrating the synthesis of the three composite mapping functions from channel 5 to channel 7.

4.2 Channel Transformation Routine

The complete flow chart of the channel transformation routine is shown in figure 4.6. The output of this routine is the mapping functions for all the channels in the array. As depicted in the flow chart, the channel transformation routine is divided into three blocks: dynamic sampling, similarity sequencing, and channel transformation.

The dynamic sampling block provides the algorithm with the outline data for all the channels in the array, using a dynamically adjusted outline data sampling size. The acquired outline data is used to calculate the targeting gains and provide the gain envelopes and phase profiles of all the channels. The outline data is also fed into the next block for similarity sequencing.

In similarity sequencing, the algorithm analyzes the gain envelopes of all the channels and calculates the fully connected "distance" matrix, which specifies the distance between the different channels. From this distance matrix, the algorithm generates a tree data structure that organizes channels from the root node (reference channel) to the children (targeting channels) in layers of similarity levels, minimizing the cost of the tree. This block, called "Similarity Tree Management," acts as a control unit for the "Channel Transformation" block, providing it with the reference channel number, reference mapping functions, and specifying a targeting channel. The "Channel Transformation" block then performs the transformation, informs the "Similarity Tree Management" of the transformation status (whether it succeeded or failed), and waits for the next instruction. Based on the transformation status of the different channels, the "Similarity Tree Management" updates the similarity tree and the reference channel accordingly. If a new reference is needed, the "Similarity Tree Management" acquires the new reference mapping functions by performing a complete channel characterization on the new reference channel.

Within the "Channel Transformation" block, the process includes transformation dataset acquisition, mapping function synthesis, and transformation validation. In addition to the discussion on channel transformation earlier, the process of transformation dataset acquisition and mapping function synthesis is iterative. Depending on the synthesis results, new transformation data are defined and acquired through several iterations. After the eleven mapping functions are synthesized, the transformation validation sets two targeting points to test the worst-case performance of the mapping functions. The results of these validation tests are then reported to the "Similarity Tree Management."

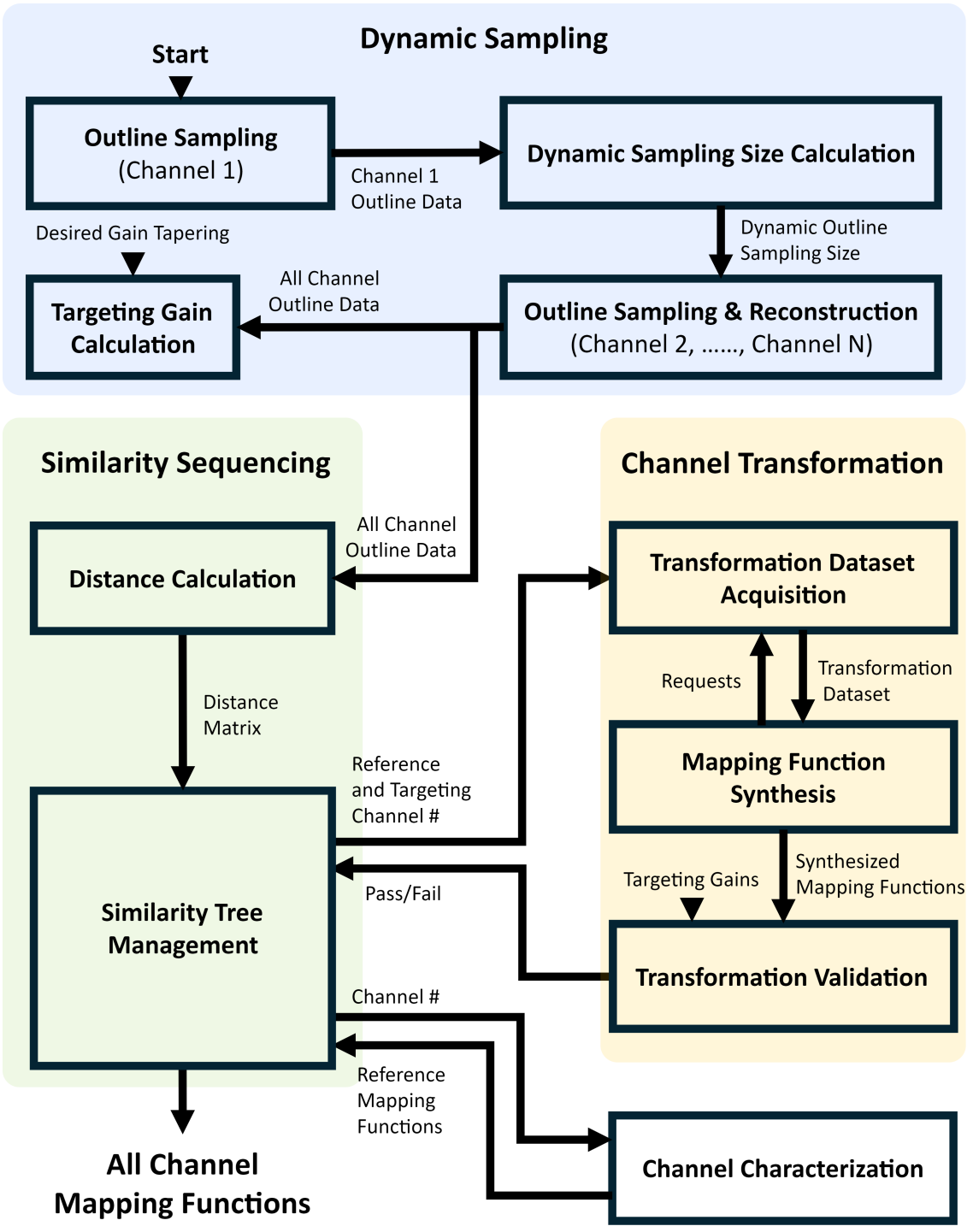


Figure 4.6: Adaptive Channel Transformation flow diagram.

4.3 Channel Transformation Method

4.3.1 Transformation Dataset Acquisition

To capture the most information on inter-channel response variations, the transformation dataset is identified at the four intersections in the characterization dataset, as illustrated in figure 4.7. For convenience, these data points are named after the gain and phase indexes from which they are measured (the gain is categorized as "mid" and "max" reflecting the sampling index choice). The four data points in the transformation dataset are defined as:

$$T_{max,main} = M^t_{I^t_{G,main}, I^t_{\theta,main}} \tag{4.1}$$

$$T_{mid,main} = M^t_{I^t_{G,aux}, I^t_{\theta,main}} \tag{4.2}$$

$$T_{max,aux} = M^t_{I^t_{G,main}, I^t_{\theta,aux}} \tag{4.3}$$

$$T_{mid,aux} = M^t_{I^t_{G,aux}, I^t_{\theta,aux}} \tag{4.4}$$

where $I^t_{G,main}$, $I^t_{G,aux}$ and $I^t_{\theta,main}$, $I^t_{\theta,aux}$ denotes the main and auxiliary gain and phase indexes in the targeting channel respectively, $M^t_{I^t_G, I^t_\theta}$ denotes the measured point in the targeting channel from measuring the gain index I^t_G and phase index I^t_θ.

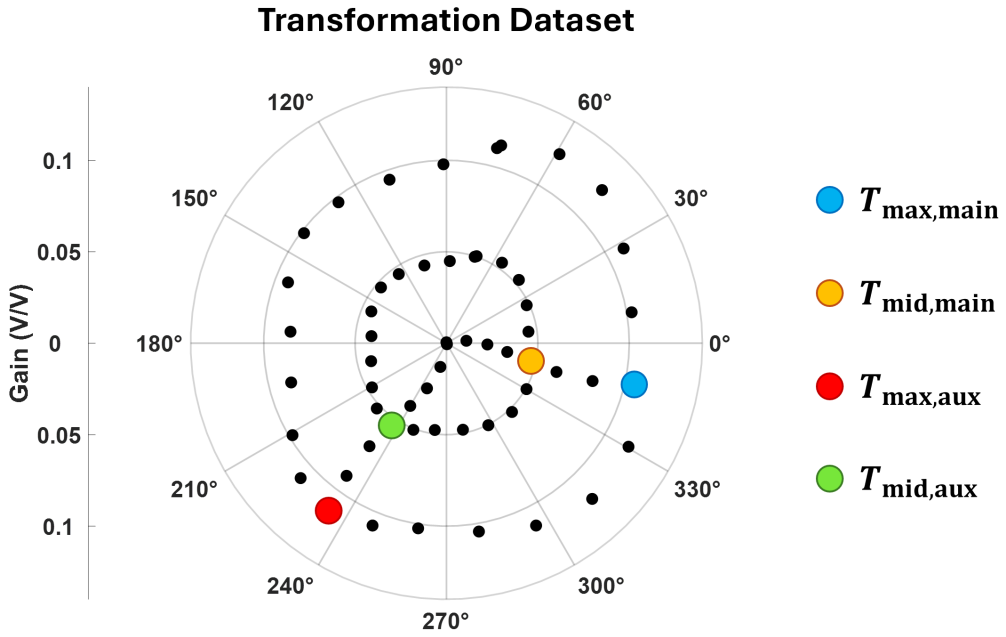


Figure 4.7: Transformation Dataset illustration.

Corresponding to the transformation dataset in the targeting channel, the reference datasets in the reference channel are defined as:

$$R_{max,main} = M^r_{I^r_{G,main},I^r_{\theta,main}} \tag{4.5}$$

$$R_{mid,main} = M^r_{I^r_{G,aux},I^r_{\theta,main}} \tag{4.6}$$

$$R_{max,aux} = M^r_{I^r_{G,main},I^r_{\theta,aux}} \tag{4.7}$$

$$R_{mid,aux} = M^r_{I^r_{G,aux},I^r_{\theta,aux}} \tag{4.8}$$

where $I^r_{G,main}$, $I^r_{G,aux}$ and $I^r_{\theta,main}$, $I^r_{\theta,aux}$ denotes the main and auxiliary gain and phase indexes in the reference channel respectively, $M^r_{I^r_G,I^r_\theta}$ denotes the measured point in the reference channel from measuring the gain index I^r_G and phase index I^r_θ.

The main and auxiliary gain indexes, $I_{G,main}$ and $I_{G,aux}$, are set to the same index across the different channels:

$$I_{G,main} = I^t_{G,main} = I^r_{G,main} = I_{G,max} \tag{4.9}$$

$$I_{G,aux} = I^t_{G,aux} = I^r_{G,aux} \tag{4.10}$$

The main and auxiliary phase indexes, $I_{\theta,main}$ and $I_{\theta,aux}$, however, could differ between the reference channel and the targeting channel. The targeting phase sampling indexes are determined progressively as the algorithm synthesizes the mapping functions.

4.3.2 Mapping Functions Synthesis

In mapping function synthesis, the algorithm adjusts the reference mapping functions to fit the response of the targeting channel. The reference mapping functions provide the function shape, while the transformation dataset provides the observations for the mapping functions to fit within the targeting channel. As discussed in the characterization section above, the "observation" at index I_o refers to the "correct" value of the mapping function at I_o obtained from an orthogonal series or, in the case of channel transformation, direct measurements.

For the different gain series mapping functions, the observation scheme involves making one observation at the maximum value and another at the midpoint, thereby performing necessary scaling and shape adjustments. For the phase series mapping functions, the potential phase shift in the phase index is approximated by the phase index shift of the gain envelope compared to the reference. After adjusting the phase index, the vertical

offset and amplitude of the phase series mapping functions are determined by the two observations made at the main and auxiliary phase indexes.

It is important to note that the main and auxiliary phase indexes in the targeting channel can differ between channel transformation and full characterization since the decision-making mapping functions, i.e., $GESP$ and $PPSP$, are synthesized and not entirely accurate. A significant deviation in the sampling indexes from the optimum could lead to reduced calibration accuracy.

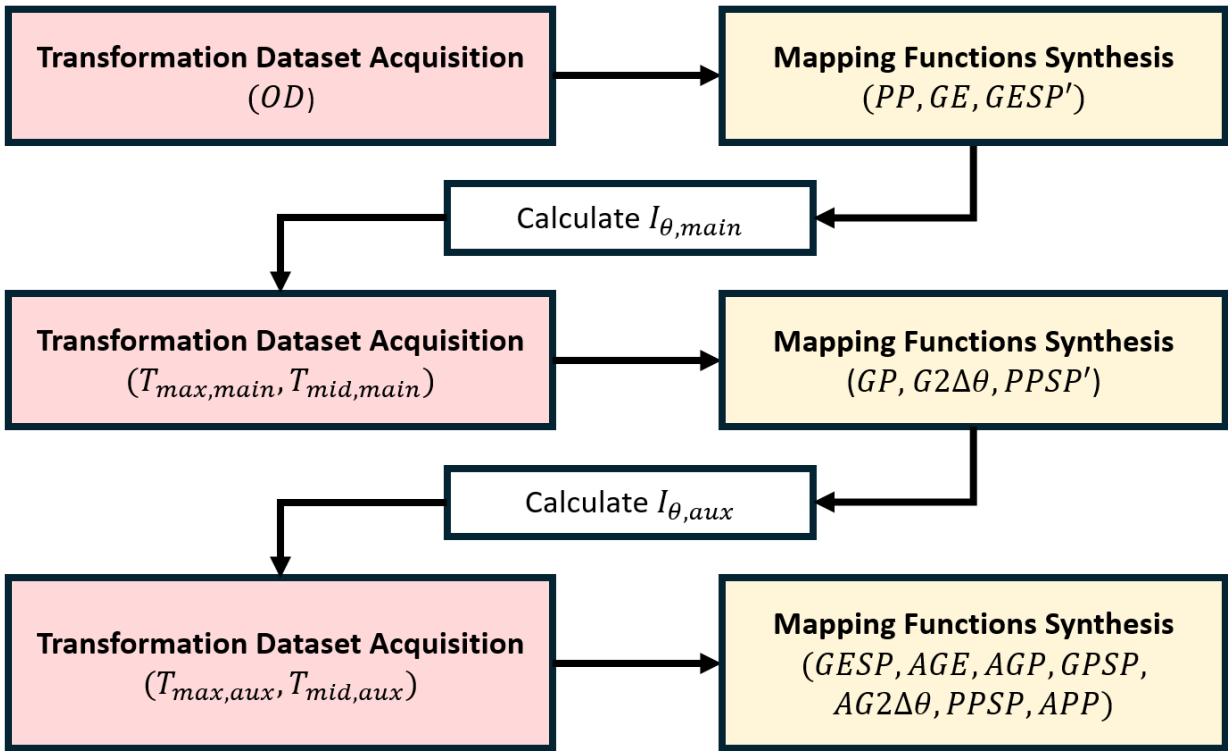


Figure 4.8: Transformation Dataset Acquisition and Mapping Functions Synthesis flow chart.

The mapping functions synthesis is not a parallel process and follows a defined operation sequence. Figure 4.8 illustrates the sequence of the transformation dataset acquisition and mapping functions synthesis. The sections below cover the synthesis algorithm not in this order and the sequential walk-through of the synthesis algorithm is in section 4.3.3 below. Note that $GESP'$ and $PPSP'$ in figure 4.8 refer to partially synthesized mapping functions that will be completed in subsequent steps.

For this section, the plots of mapping functions synthesis from channel 5 to channel 7 in the 4x4 BFIC1 array are used as examples for demonstration.

Gain Profile

The synthesis of the main and auxiliary gain profiles in the targeting channel relies on the observations made on $I^t_{G,main} = I_{G,max}$ and $I^t_{G,aux}$. From the transformation dataset, the two observations for the main gain profile in the targeting channel GP_t are:

$$GP_t(I^t_{G,main}) = |T_{max,main}| \tag{4.11}$$

$$GP_t(I^t_{G,aux}) = |T_{mid,main}| \tag{4.12}$$

To synthesize the gain profile in the targeting channel, the reference gain profile GP_r is first scaled to fit the observation at $I_{G,max}$:

$$GP_t(I_G) = GP_r(I_G) \cdot \frac{|T_{max,main}|}{|R_{max,main}|} \tag{4.13}$$

Then, the resulting $GP_t(I_G)$ is shape-modified to fit the observation at $I_{G,aux}$. To perform this shape modification, the algorithm first calculates the boundaries, or fixed ends, of the gain profile for which the shape modification doesn't affect. The upper fixed end is $GP_t(I_{G,max})$ since it is already observed. The lower fixed end is $GP_t(0)$ since the gain index of 0 is not reachable and is assumed to be a constant. This lower fixed end is calculated by extrapolation of the reference gain envelope:

$$GP_t(0) = extrapolate\big(GP_r(I_G)@I_G = 0\big) \tag{4.14}$$

With the upper and lower fixed ends, the gain profile in (4.13) is scaled with respect to the line connecting the two fixed ends to fit the observation at $I^t_{G,aux}$. The line connecting the two ends and the synthesized gain profile is calculated as:

$$L(I_G) = \frac{GP_t(I^t_{G,main}) - GP_t(0)}{I^t_{G,main}} \cdot I_G + GP_t(0) \tag{4.15}$$

$$GP_t(I_G) = (GP_t(I_G) - L(I_G)) \cdot \frac{|T_{mid,main}| - L(I^t_{G,aux})}{GP_t(I^t_{G,aux}) - L(I^t_{G,aux})} + L(I_G) \tag{4.16}$$

For the auxiliary gain profile in the targeting channel AGP_t, the two observations are:

$$AGP_t(I^t_{G,main}) = |T_{max,aux}| \tag{4.17}$$

$$AGP_t(I^t_{G,aux}) = |T_{mid,aux}| \tag{4.18}$$

Following a similar process and using the reference auxiliary gain profile AGP_r, the auxiliary gain profile in the targeting channel AGP_t is synthesized as:

$$AGP_t(I_G) = AGP_r(I_G) \cdot \frac{|T_{max,aux}|}{|R_{max,aux}|} \tag{4.19}$$

$$AGP_t(0) = extrapolate\big(AGP_r(I_G)@I_G = 0\big) \tag{4.20}$$

$$L(I_G) = \frac{AGP_t(I^t_{G,main}) - AGP_t(0)}{I^t_{G,main}} \cdot I_G + AGP_t(0) \tag{4.21}$$

$$AGP_t(I_G) = (AGP_t(I_G) - L(I_G)) \cdot \frac{|T_{mid,aux}| - L(I^t_{G,aux})}{AGP_t(I^t_{G,aux}) - L(I^t_{G,aux})} + L(I_G) \tag{4.22}$$

Figure 4.9 demonstrates the synthesis of the main and auxiliary gain profiles in the targeting channel. We confirm that the synthesized gain profiles follow the same shape as their references and they pass through their respective observations.

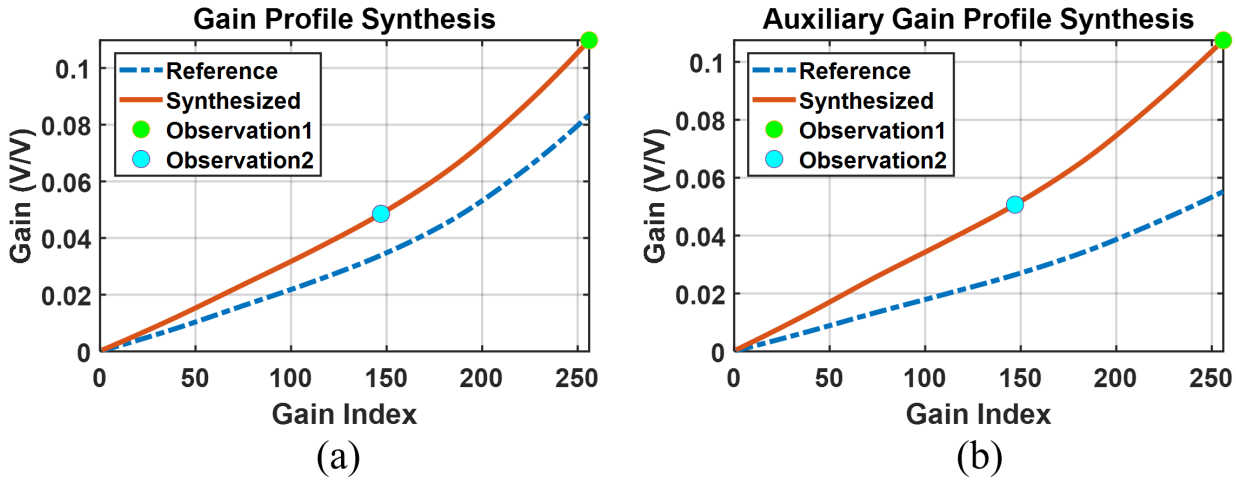


Figure 4.9: Gain profile synthesis illustration: (a) gain profile synthesis; (b) auxiliary gain profile synthesis.

Phase Profile

The main phase profile in the targeting channel PP_t is directly available from the outline data of the targeting channel $OD_t(I_\theta)$ acquired from dynamic sampling:

$$PP_t(I_\theta) = phase(OD_t(I_\theta)) \tag{4.23}$$

The auxiliary phase profile in the targeting channel APP_t would have the following two observations:

$$APP_t(I^t_{\theta,main}) = phase(T_{mid,main}) \tag{4.24}$$

$$APP_t(I^t_{\theta,aux}) = phase(T_{mid,aux}) \tag{4.25}$$

Since the two observations made on the auxiliary phase profile cannot be used simultaneously for scaling or shifting without conflicts, direct observation of the auxiliary phase profile leads to loss of information. Instead, the algorithm synthesizes the auxiliary phase profile using an intermediate technique. By synthesizing the phase profile shifting profile, the auxiliary phase profile is derived from the definitions in (3.17). Unlike the auxiliary phase profile, the phase profile shifting profile can be synthesized using both observations without information loss, resulting in a more natural and continuous auxiliary phase profile.

Assuming the synthesis of the phase profile shifting profile in the targeting channel $PPSP_t$ has already been done, the APP_t is synthesized from the definition of the $PPSP$:

$$APP_t(I_\theta) = PPSP_t(I_\theta) + PP_t(I_\theta) + phase(T_{mid,main}) - phase(T_{max,main}) \tag{4.26}$$

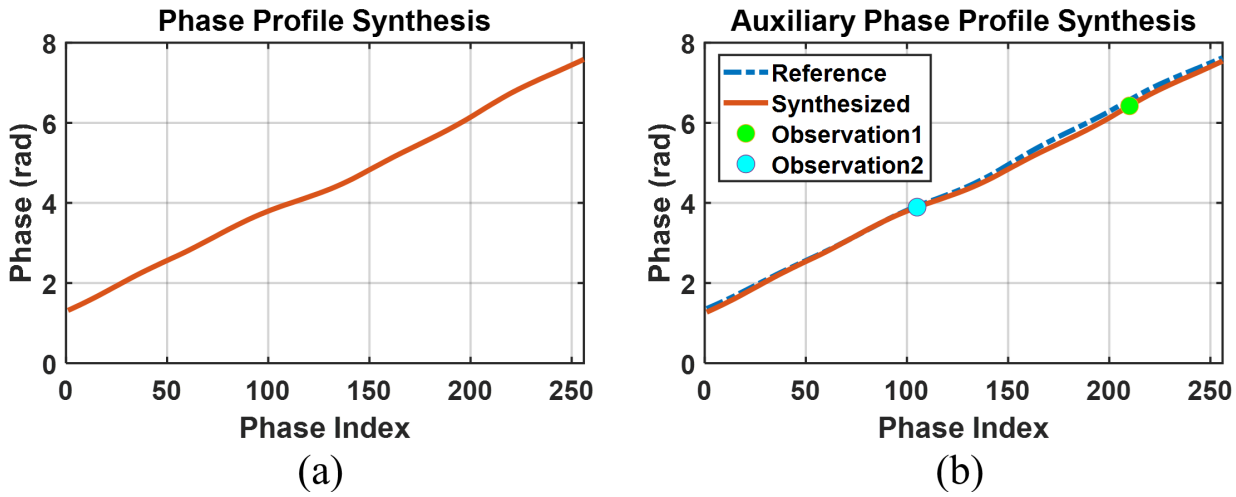


Figure 4.10: Phase profile synthesis illustration: (a) Phase profile synthesis; (b) Auxiliary phase profile synthesis.

Figure 4.10 demonstrates the synthesis of the main and auxiliary phase profiles in the targeting channel. We confirm that the synthesized auxiliary phase profile passes through its observations.

Gain Envelope

The main gain envelope in the targeting channel (GE_t) is directly available from the outline data of the targeting channel $OD_t(I_\theta)$ acquired from dynamic sampling:

$$GE_t(I_\theta) = |OD_t(I_\theta)| \tag{4.27}$$

The auxiliary gain envelope in the targeting channel AGE_t would have the following two observations:

$$AGE_t(I^t_{\theta,main}) = |T_{mid,main}| \tag{4.28}$$

$$AGE_t(I^t_{\theta,aux}) = |T_{mid,aux}| \tag{4.29}$$

Similar to the synthesis of the auxiliary phase profile in the targeting channel, the synthesis of the auxiliary gain envelope in the targeting channel AGE_t is done via the synthesis of the gain envelope scaling profile to avoid the loss of information.

Assuming the synthesis of the gain envelope scaling profile in the targeting channel $GESP_t$ has already been done, the AGE_t is synthesized from the definition of the $GESP$:

$$AGE_t(I_\theta) = GESP_t(I_\theta) \cdot GE_t(I_\theta) \tag{4.30}$$

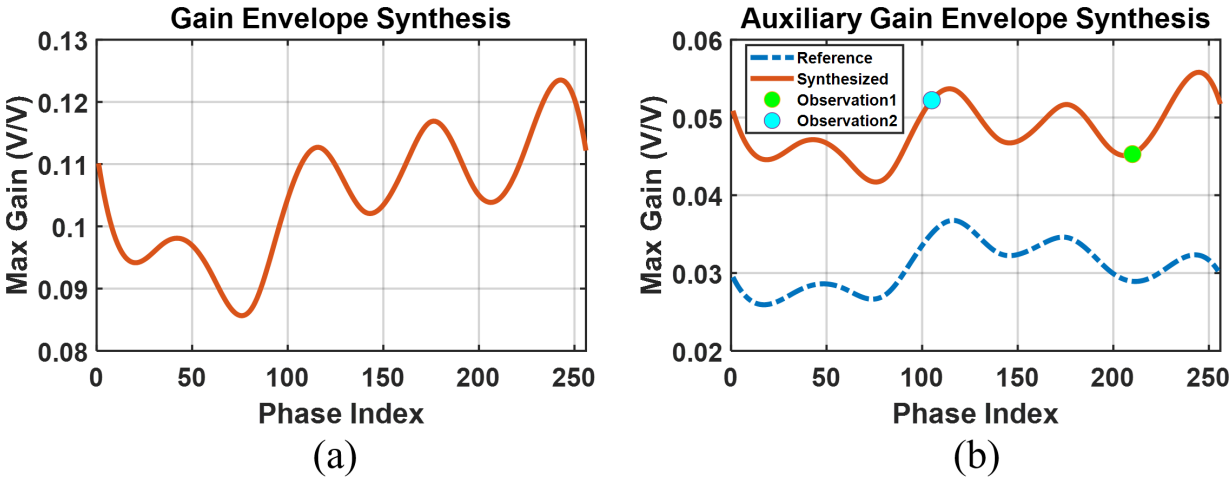


Figure 4.11: Gain envelope synthesis illustration: (a) Gain envelope synthesis; (b) Auxiliary gain envelope synthesis.

Figure 4.11 demonstrates the synthesis of the main and auxiliary gain envelopes in the targeting channel. We confirm that the synthesized auxiliary gain envelope passes through its observations.

Gain-to-Phase Variation

The synthesis of the main and auxiliary gain-to-phase variations in the targeting channel relies on the observation made on $I^t_{G,aux}$ only since the gain-to-phase variation by definition has a value of 0 at $I^t_{G,main}$. From the transformation dataset, the observation for the main gain-to-phase variation in the targeting channel $G2\Delta\theta_t$ is:

$$G2\Delta\theta_t(I^t_{G,aux}) = phase(T_{mid,main}) - phase(T_{max,main}) \tag{4.31}$$

Since the gain-to-phase variation is a gain series, we deploy a similar function-fitting approach as the synthesis of the gain profiles to align the gain-to-phase variation with the observation. Scaling with respect to the two fixed ends and using the reference gain-to-phase variation $G2\Delta\theta_r$, the gain-to-phase variation in the targeting channel $G2\Delta\theta_t$ is synthesized as:

$$G2\Delta\theta_t(0) = extrapolate\big(G2\Delta\theta_r(I_G)@I_G = 0\big) \tag{4.32}$$

$$L(I_G) = \frac{G2\Delta\theta_t(I^t_{G,main}) - G2\Delta\theta_t(0)}{I^t_{G,main}} \cdot I_G + G2\Delta\theta_t(0) = \frac{-G2\Delta\theta_t(0)}{I^t_{G,main}} \cdot I_G + G2\Delta\theta_t(0) \tag{4.33}$$

$$G2\Delta\theta_t(I_G) = (G2\Delta\theta_t(I_G) - L(I_G)) \cdot \frac{phase(T_{mid,main}) - phase(T_{max,main}) - L(I^t_{G,aux})}{G2\Delta\theta_t(I^t_{G,aux}) - L(I^t_{G,aux})} + L(I_G) \tag{4.34}$$

For the auxiliary gain-to-phase variation in the targeting channel $AG2\Delta\theta_t$, its observation is:

$$AG2\Delta\theta_t(I^t_{G,aux}) = phase(T_{mid,aux}) - phase(T_{max,aux}) \tag{4.35}$$

Then, using the reference auxiliary gain-to-phase variation $AG2\Delta\theta_r$, the auxiliary gain-to-phase variation in the targeting channel $AG2\Delta\theta_t$ is synthesized as:

$$AG2\Delta\theta_t(0) = extrapolate\big(AG2\Delta\theta_r(I_G)@I_G = 0\big) \tag{4.36}$$

$$L(I_G) = \frac{AG2\Delta\theta_t(I^t_{G,main}) - AG2\Delta\theta_t(0)}{I^t_{G,main}} \cdot I_G + AG2\Delta\theta_t(0) = \frac{-AG2\Delta\theta_t(0)}{I^t_{G,main}} \cdot I_G + AG2\Delta\theta_t(0) \tag{4.37}$$

$$AG2\Delta\theta_t(I_G) = (AG2\Delta\theta_t(I_G) - L(I_G)) \cdot \frac{phase(T_{mid,aux}) - phase(T_{max,aux}) - L(I^t_{G,aux})}{AG2\Delta\theta_t(I^t_{G,aux}) - L(I^t_{G,aux})} + L(I_G) \tag{4.38}$$

Figure 4.12 demonstrates the synthesis of the main and auxiliary gain-to-phase variations in the targeting channel. We confirm that the synthesized gain-to-phase variations pass through its observation.

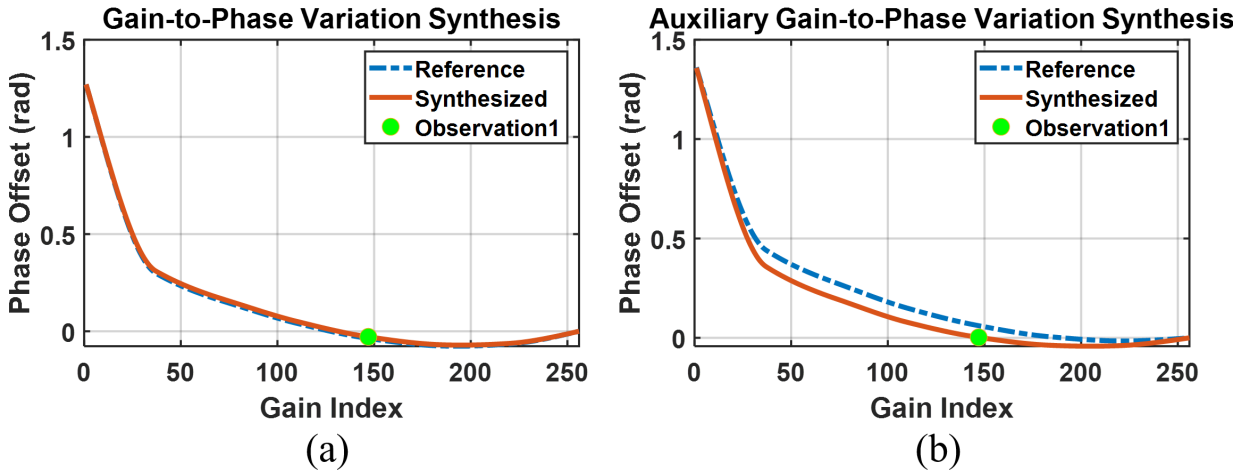


Figure 4.12: Gain-to-phase variation synthesis illustration: (a) Gain-to-phase variation synthesis; (b) Auxiliary gain-to-phase variation synthesis.

Gain Envelope Scaling Profile

As outlined in the flow chart in figure 4.8, the gain envelope scaling profile in the targeting channel $GESP_t$ needs to be synthesized early. This is because the $GESP_t$ is important in deciding where the optimum $I^t_{\theta,main}$ and $I^t_{\theta,aux}$ are:

$$I^t_{\theta,main} = argmin(GESP_t(I_\theta)) \tag{4.39}$$

$$I^t_{\theta,aux} = argmax\left(|PPSP_t(I_\theta)| \cdot (GESP_t(I_\theta) - min(GESP_t(I_\theta)))\right) \tag{4.40}$$

Since the $PPSP_t$ depends on $I^t_{\theta,main}$, the algorithm starts with synthesizing the $GESP_t$ to determine the $I^t_{\theta,main}$. From the definition of the gain envelope scaling profile, the $GESP_t$ is defined as:

$$GESP_t(I_\theta) = \frac{AGE_t(I_\theta)}{GE_t(I_\theta)} \tag{4.41}$$

To use this definition, the algorithm would require both the main and auxiliary gain envelopes in the targeting channel from the start. However, the auxiliary gain envelope is not initially available and acquiring it would require extensive measurements.

As indicated in (4.39), the $GESP_t$ must have the correct maximum and minimum indexes for accurate selection of $I^t_{\theta,main}$. Thus, for the purpose of selecting the optimum $I^t_{\theta,main}$, $GESP_t$ does not need fully accurate magnitudes initially. An approximation of $GESP_t$ can be made by substituting the targeting auxiliary gain envelope AGE_t with

the reference auxiliary gain envelope AGE_r. However, due to the unpredictability in the gain envelopes across channels, using the potentially magnitude and phase misaligned reference auxiliary gain envelope alters the phase of $GESP_t$, affecting the selection of $I^t_{\theta,main}$. Therefore, the algorithm needs an alternative method to synthesize the $GESP_t$.

Theoretically, the mapping functions GE, AGE, $GESP$, and $PPSP$ are bound to the phases of the main and auxiliary outline data. Assuming the main and auxiliary outline data rotate in phase index by roughly the same amount across different channels, the phase shift in $GESP$ and $PPSP$ can be approximated as the phase shift in GE. Even if the main and auxiliary gain envelopes rotate by different amounts across channels, as long as their shapes are similar, it primarily affects the amplitude of the $GESP$, not the location of the maximum and minimum. Therefore, by extracting the phase shift in the gain envelope from the reference channel to the targeting channel, we can approximate $GESP_t$ and $PPSP_t$ in the targeting channel by shifting their references by the same amount.

For accurate detection of the phase of the gain envelope, its fundamental tone, which has the period of the entire phase index range, is extracted and used for calculating the phase shift in the phase index. Assuming the phase index range is from 1 to $I_{\theta,max}$, the phase index shift ΔI_θ from the reference gain envelope GE_r to the targeting gain envelope GE_t is calculated as:

$$\Delta I_\theta = \left(phase(\sum_{n=0}^{I_{\theta,max}-1} GE_t(n) e^{j2\pi n/I_{\theta,max}}) - phase(\sum_{n=0}^{I_{\theta,max}-1} GE_r(n) e^{j2\pi n/I_{\theta,max}}) \right) \frac{I_{\theta,max}}{2\pi} \tag{4.42}$$

Using this index shift along with the reference gain envelope scaling profile $GESP_r$, the preliminary gain envelope scaling profile in the targeting channel $GESP'_t$ is synthesized as:

$$GESP'_t(I_\theta) = GESP_r(I_\theta - \Delta I_\theta) \tag{4.43}$$

From $GESP'_t$, the $I^t_{\theta,main}$ could be calculated as:

$$I^t_{\theta,main} = argmin(GESP'_t(I_\theta)) \tag{4.44}$$

Figure 4.13 demonstrates the detection of the phase shift in the gain envelope from the reference channel to the targeting channel and the subsequent synthesis of the preliminary gain envelope scaling profile in the targeting channel.

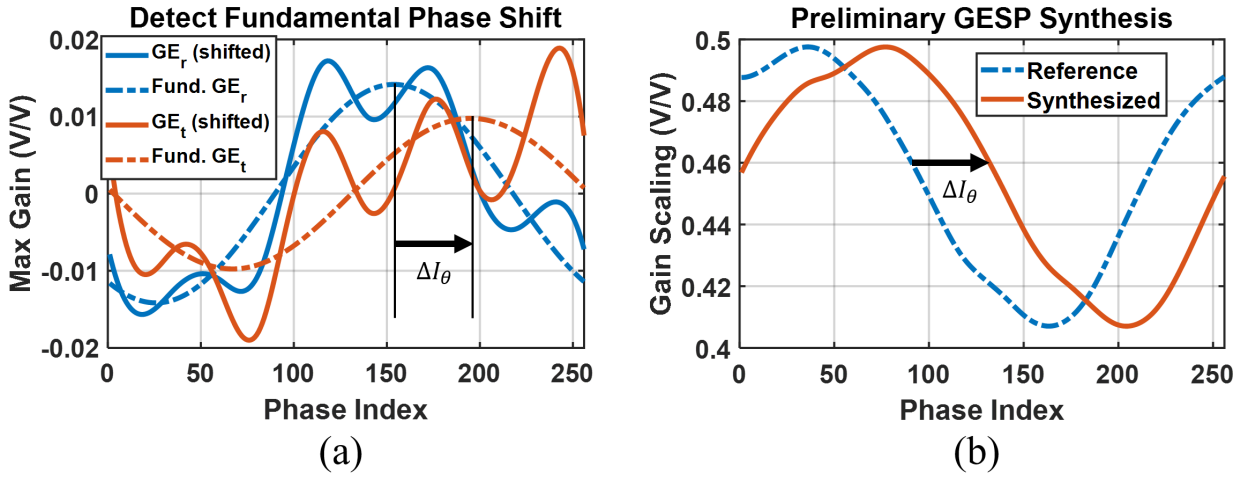


Figure 4.13: Preliminary GESP synthesis illustration: (a) Detect fundamental gain envelope phase shift; (b) Preliminary GESP synthesis.

As the algorithm progresses to acquire the transformation dataset, the two observations of the $GESP_t$ are calculated:

$$GESP_t(I^t_{\theta,main}) = \frac{|T_{mid,main}|}{|T_{max,main}|} \tag{4.45}$$

$$GESP_t(I^t_{\theta,aux}) = \frac{|T_{mid,aux}|}{|T_{max,aux}|} \tag{4.46}$$

For synthesizing the final gain envelope scaling profile in the targeting channel $GESP_t$, the algorithm utilizes the two observations to shift and scale the function and fix it in place on the y-axis. First, the preliminary gain envelope scaling profile in the targeting channel $GESP'_t$ is shifted to meet with the observation at $I^t_{\theta,main}$;

$$GESP_t(I_\theta) = GESP'_t(I_\theta) + \frac{|T_{mid,main}|}{|T_{max,main}|} - GESP'_t(I^t_{\theta,main}) \tag{4.47}$$

Then, it is scaled with respect to the y-value of the first observation at $I^t_{\theta,main}$ to meet with the second observation at $I^t_{\theta,aux}$:

$$GESP_t(I_\theta) = \frac{\frac{|T_{mid,aux}|}{|T_{max,aux}|} - \frac{|T_{mid,main}|}{|T_{max,main}|}}{GESP_t(I^t_{\theta,aux}) - \frac{|T_{mid,main}|}{|T_{max,main}|}} \cdot \left(GESP_t(I_\theta) - \frac{|T_{mid,main}|}{|T_{max,main}|}\right) + \frac{|T_{mid,main}|}{|T_{max,main}|} \tag{4.48}$$

Note that the above synthesis procedures are sensitive to the relative magnitudes of the two observations. If the $I^t_{\theta,main}$ and $I^t_{\theta,aux}$ are chosen based on the proposed definitions in (4.39) and (4.40), then they will be far apart.

Figure 4.14 demonstrates the synthesis of the final gain envelope scaling profile in the targeting channel. We confirm that the synthesized gain envelope scaling profile passes through its observations.

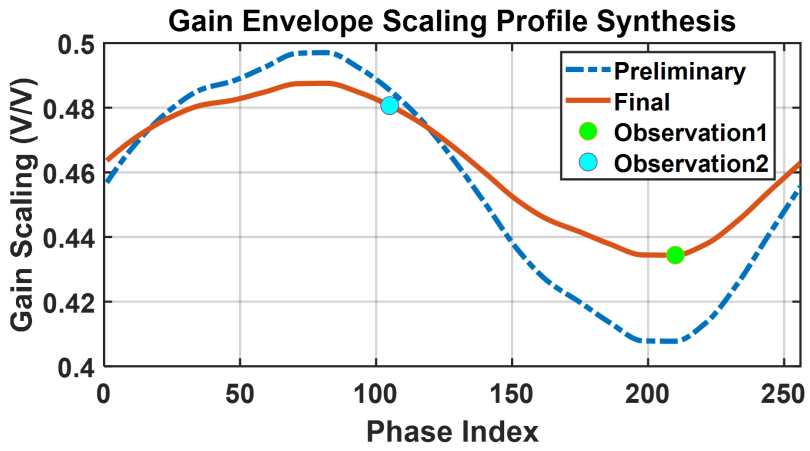


Figure 4.14: Final gain envelope scaling profile synthesis illustration.

Gain Profile Scaling Profile

Gain profile scaling profile in the targeting channel $GPSP_t$ only has one observation at $I^t_{G,aux}$ since by its definition in (3.15), it has a value of 1 at $I^t_{G,main}$. The observation of the $GPSP_t$ is:

$$GPSP_t(I^t_{G,aux}) = \frac{|T_{mid,aux}|}{|T_{mid,main}|} \cdot \frac{|T_{max,main}|}{|T_{max,aux}|} \tag{4.49}$$

The synthesis of the $GPSP_t$ is done by synthesizing the main and auxiliary gain profiles in the targeting channel GP_t and AGP_t and using the definition in (3.15):

$$GPSP_t(I_G) = \frac{AGP_t(I_G)}{GP_t(I_G)} \cdot \frac{GE_t(I^t_{\theta,main})}{GE_t(I^t_{\theta,aux})} \tag{4.50}$$

Figure 4.15 demonstrates the synthesis of the gain profile scaling profile in the targeting channel. We confirm that the synthesized gain profile scaling profile passes through its observation.

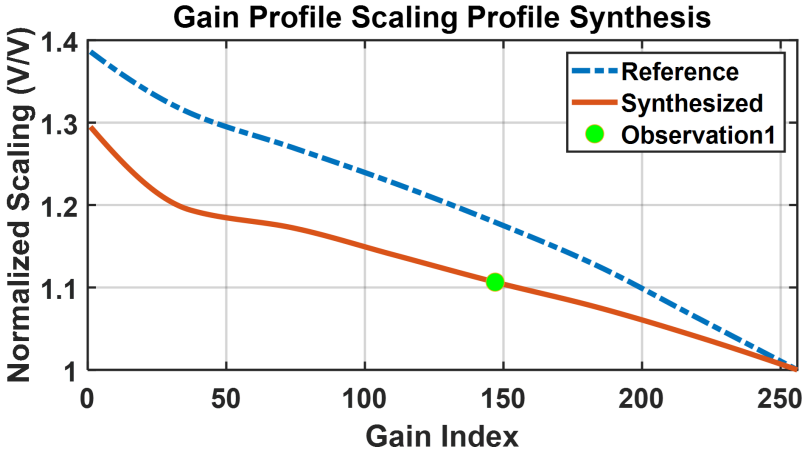


Figure 4.15: Gain profile scaling profile synthesis illustration.

Phase Profile Shifting Profile

As depicted in the flow chart in figure 4.8, the synthesis of the phase profile shifting profile in the targeting channel $PPSP_t$ has two stages similar to the synthesis of the $GESP_t$. This is because the $PPSP_t$ decides the choice of $I^t_{\theta,aux}$ but it need an observation at the decided $I^t_{\theta,aux}$ to be fully accurate.

At the stage of deciding the $I^t_{\theta,aux}$, the preliminary phase profile shifting profile and gain envelope scaling profile in the targeting channel, $PPSP'_t$ and $GESP'_t$, needs to have the correct phase for the figure-of-merit (FOM) based selection scheme in (4.51) below to function correctly.

$$I^t_{\theta,aux} = argmax\left(|PPSP'_t(I_\theta)| \cdot (GESP'_t(I_\theta) - min(GESP'_t(I_\theta)))\right) \tag{4.51}$$

As discussed in the gain envelope scaling profile synthesis section above (section 4.3.2), the phase shift in $PPSP$ from the reference channel to the targeting channel can be approximated by the phase shift in the gain envelopes from the reference channel to the targeting channel. Using the phase index shift calculated in (4.42), the reference phase profile shifting profile $PPSP_r$ is shifted to synthesize the $PPSP'_t$:

$$PPSP'_t(I_\theta) = PPSP_r(I_\theta - \Delta I_\theta) \tag{4.52}$$

From the definition of the $PPSP$ in (3.17), it needs to have a value of 0 at the $I^t_{\theta,main}$:

$$PPSP'_t(I^t_{\theta,main}) = 0 \tag{4.53}$$

To meet this observation, the resulting $PPSP'_t$ is shifted vertically to have a value of 0 at the $I^t_{\theta,main}$:

$$PPSP'_t(I_\theta) = PPSP'_t(I_\theta) - PPSP'_t(I^t_{\theta,main}) \tag{4.54}$$

Then, the $I^t_{\theta,aux}$ is calculated using (4.51) and the $T_{max,aux}$ and $T_{mid,aux}$ are acquired. Using the newly acquired transformation data, a second observation is calculated at the $I^t_{\theta,aux}$ (derived from (3.29)):

$$PPSP_t(I^t_{\theta,aux}) = AG2\Delta\theta_t(I^t_{G,aux}) - G2\Delta\theta_t(I^t_{G,aux}) \tag{4.55}$$

$$= phase(T_{mid,aux}) - phase(T_{max,aux}) - phase(T_{mid,main}) + phase(T_{max,main}) \tag{4.56}$$

To meet with this observation, the $PPSP_t$ is scaled about the baseline of 0:

$$PPSP_t(I_\theta) = \frac{AG2\Delta\theta_t(I^t_{G,aux}) - G2\Delta\theta_t(I^t_{G,aux})}{PPSP_t(I^t_{\theta,aux})} \cdot PPSP_t(I_\theta) \tag{4.57}$$

Figure 4.16 demonstrates the synthesis of the $PPSP_t$. We confirm that the synthesized phase profile shifting profile passes through its observations.

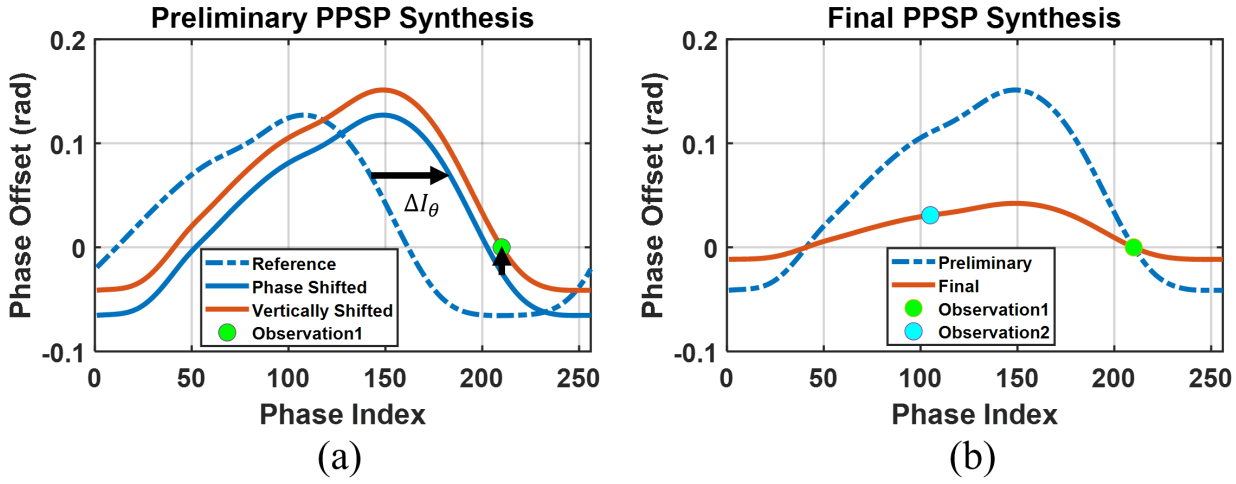


Figure 4.16: Phase profile shifting profile synthesis illustration: (a) Preliminary PPSP synthesis; (b) Final PPSP synthesis.

4.3.3 Synthesis Sequence Walk-through

In the transformation dataset acquisition and mapping functions synthesis sections above (section 4.3.1 and 4.3.2), the algorithms are defined, derived and presented in detail. However, the algorithm is not presented in the order in which they occur in the channel transformation routine. To clear causality confusion, this section presents the algorithm sequentially.

Figure 4.17 defines three stages for the routine of transformation dataset acquisition and mapping functions synthesis. Provided that the "Similarity Tree Management", shown in figure 4.6, calls for the transformation of the targeting channel from the fully characterized reference channel, the three stages are presented in order.

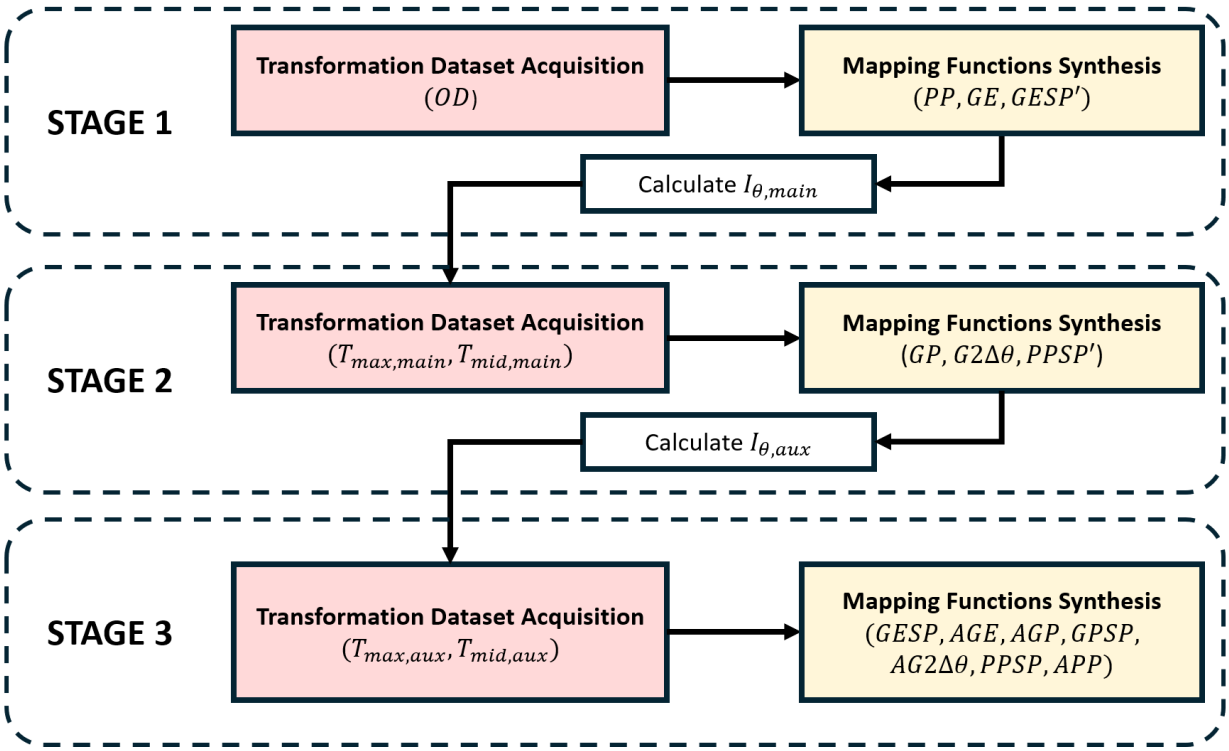


Figure 4.17: Transformation Dataset Acquisition and Mapping Functions Synthesis stages.

Stage 1

Arriving at stage 1, the algorithm has the defined reference mapping functions and the outline data of all elements. $I^t_{G,main}$ and $I^t_{G,aux}$ are set to $I^r_{G,main}$ and $I^r_{G,aux}$, respectively. Stage 1 proceeds as follows:

$$PP_t(I_\theta) = phase(OD_t(I_\theta)) \tag{4.58}$$

$$GE_t(I_\theta) = |OD_t(I_\theta)| \tag{4.59}$$

$$\Delta I_\theta = \left(phase(\sum_{n=0}^{I_{\theta,max}-1} GE_t(n) e^{j2\pi n/I_{\theta,max}}) - phase(\sum_{n=0}^{I_{\theta,max}-1} GE_r(n) e^{j2\pi n/I_{\theta,max}}) \right) \frac{I_{\theta,max}}{2\pi} \tag{4.60}$$

$$GESP'_t(I_\theta) = GESP_r(I_\theta - \Delta I_\theta) \tag{4.61}$$

$$I^t_{\theta,main} = argmin(GESP'_t(I_\theta)) \tag{4.62}$$

Stage 2

Arriving at stage 2, the algorithm acquires the transformation data $T_{max,main}$ and $T_{mid,main}$ using the $I^t_{\theta,main}$ calculated from stage 1.

$$T_{max,main} = M^t_{I^t_{G,main}, I^t_{\theta,main}} \tag{4.63}$$

$$T_{mid,main} = M^t_{I^t_{G,aux}, I^t_{\theta,main}} \tag{4.64}$$

Note that since the $T_{max,main}$ is included in the targeting channel's outline data, it can be calculated as:

$$T_{max,main} = GE_t(I^t_{\theta,main}) \cdot e^{jPP_t(I^t_{\theta,main})} \tag{4.65}$$

Similarly, $R_{max,main}$ can be calculated as:

$$R_{max,main} = GE_r(I^r_{\theta,main}) \cdot e^{jPP_r(I^r_{\theta,main})} \tag{4.66}$$

Stage 2 proceeds as follows:

$$GP_t(I_G) = GP_r(I_G) \cdot \frac{|T_{max,main}|}{|R_{max,main}|} \tag{4.67}$$

$$GP_t(0) = extrapolate\big(GP_r(I_G)@I_G = 0\big) \tag{4.68}$$

$$L(I_G) = \frac{GP_t(I^t_{G,main}) - GP_t(0)}{I^t_{G,main}} \cdot I_G + GP_t(0) \tag{4.69}$$

$$GP_t(I_G) = (GP_t(I_G) - L(I_G)) \cdot \frac{|T_{mid,main}| - L(I^t_{G,aux})}{GP_t(I^t_{G,aux}) - L(I^t_{G,aux})} + L(I_G) \tag{4.70}$$

$$G2\Delta\theta_t(0) = extrapolate\big(G2\Delta\theta_r(I_G)@I_G = 0\big) \tag{4.71}$$

$$L(I_G) = \frac{G2\Delta\theta_t(I^t_{G,main}) - G2\Delta\theta_t(0)}{I^t_{G,main}} \cdot I_G + G2\Delta\theta_t(0) = \frac{-G2\Delta\theta_t(0)}{I^t_{G,main}} \cdot I_G + G2\Delta\theta_t(0) \tag{4.72}$$

$$G2\Delta\theta_t(I_G) = (G2\Delta\theta_t(I_G) - L(I_G)) \cdot \frac{phase(T_{mid,main}) - phase(T_{max,main}) - L(I^t_{G,aux})}{G2\Delta\theta_t(I^t_{G,aux}) - L(I^t_{G,aux})} + L(I_G) \tag{4.73}$$

$$PPSP'_t(I_\theta) = PPSP_r(I_\theta - \Delta I_\theta) \tag{4.74}$$

$$PPSP'_t(I_\theta) = PPSP'_t(I_\theta) - PPSP'_t(I^t_{\theta,main}) \tag{4.75}$$

$$I^t_{\theta,aux} = argmax\left(|PPSP'_t(I_\theta)| \cdot (GESP'_t(I_\theta) - min(GESP'_t(I_\theta)))\right) \tag{4.76}$$

Stage 3

Stage 3 is the completion stage since it now has all the transformation data. Arriving at stage 3, the algorithm acquires the transformation data $T_{max,aux}$ and $T_{mid,aux}$ using the $I^t_{\theta,aux}$ calculated from stage 2.

$$T_{max,aux} = M^t_{I^t_{G,main}, I^t_{\theta,aux}} \tag{4.77}$$

$$T_{mid,aux} = M^t_{I^t_{G,aux}, I^t_{\theta,aux}} \tag{4.78}$$

Note that since the $T_{max,aux}$ is included in the targeting channel's outline data, it can be calculated as:

$$T_{max,aux} = GE_t(I^t_{\theta,aux}) \cdot e^{jPP_t(I^t_{\theta,aux})} \tag{4.79}$$

Similarly, $R_{max,aux}$ is calculated as:

$$R_{max,aux} = GE_r(I^r_{\theta,aux}) \cdot e^{jPP_r(I^r_{\theta,aux})} \tag{4.80}$$

Stage 3 proceeds as follows:

$$GESP_t(I_\theta) = GESP'_t(I_\theta) + \frac{|T_{mid,main}|}{|T_{max,main}|} - GESP'_t(I^t_{\theta,main}) \tag{4.81}$$

$$GESP_t(I_\theta) = \frac{\frac{|T_{mid,aux}|}{|T_{max,aux}|} - \frac{|T_{mid,main}|}{|T_{max,main}|}}{GESP_t(I^t_{\theta,aux}) - \frac{|T_{mid,main}|}{|T_{max,main}|}} \cdot \Big(GESP_t(I_\theta) - \frac{|T_{mid,main}|}{|T_{max,main}|}\Big) + \frac{|T_{mid,main}|}{|T_{max,main}|} \tag{4.82}$$

$$AGE_t(I_\theta) = GESP_t(I_\theta) \cdot GE_t(I_\theta) \tag{4.83}$$

$$AGP_t(I_G) = AGP_r(I_G) \cdot \frac{|T_{max,aux}|}{|R_{max,aux}|} \tag{4.84}$$

$$AGP_t(0) = extrapolate\big(AGP_r(I_G)@I_G = 0\big) \tag{4.85}$$

$$L(I_G) = \frac{AGP_t(I^t_{G,main}) - AGP_t(0)}{I^t_{G,main}} \cdot I_G + AGP_t(0) \tag{4.86}$$

$$AGP_t(I_G) = (AGP_t(I_G) - L(I_G)) \cdot \frac{|T_{mid,aux}| - L(I^t_{G,aux})}{AGP_t(I^t_{G,aux}) - L(I^t_{G,aux})} + L(I_G) \tag{4.87}$$

$$GPSP_t(I_G) = \frac{AGP_t(I_G)}{GP_t(I_G)} \cdot \frac{GE_t(I^t_{\theta,main})}{GE_t(I^t_{\theta,aux})} \tag{4.88}$$

$$AG2\Delta\theta_t(0) = extrapolate\big(AG2\Delta\theta_r(I_G)@I_G = 0\big) \tag{4.89}$$

$$L(I_G) = \frac{AG2\Delta\theta_t(I^t_{G,main}) - AG2\Delta\theta_t(0)}{I^t_{G,main}} \cdot I_G + AG2\Delta\theta_t(0) = \frac{-AG2\Delta\theta_t(0)}{I^t_{G,main}} \cdot I_G + AG2\Delta\theta_t(0) \tag{4.90}$$

$$AG2\Delta\theta_t(I_G) = (AG2\Delta\theta_t(I_G) - L(I_G)) \cdot \frac{phase(T_{mid,aux}) - phase(T_{max,aux}) - L(I^t_{G,aux})}{AG2\Delta\theta_t(I^t_{G,aux}) - L(I^t_{G,aux})} + L(I_G) \tag{4.91}$$

$$PPSP_t(I_\theta) = \frac{phase(T_{mid,aux}) - phase(T_{max,aux}) - phase(T_{mid,main}) + phase(T_{max,main})}{PPSP_t(I^t_{\theta,aux})} \cdot PPSP_t(I_\theta) \tag{4.92}$$

$$APP_t(I_\theta) = PPSP_t(I_\theta) + PP_t(I_\theta) + phase(T_{mid,main}) - phase(T_{max,main}) \tag{4.93}$$

4.3.4 Transformation Validation

To ensure the synthesized mapping functions do not significantly deviate from the true mapping functions, transformation validation tests their accuracy. Minimizing the number of measurements needed for validation, the algorithm needs to target the worst-case scenarios for the accuracy of the synthesized mapping functions for testing.

As one of the fundamental theories and as outlined in Figure 4.18, calibration is most accurate when targeting constellation regions where the gain and phase profiles intersect. Conversely, calibration performs the worst when targeting constellation regions furthest from the intersections.

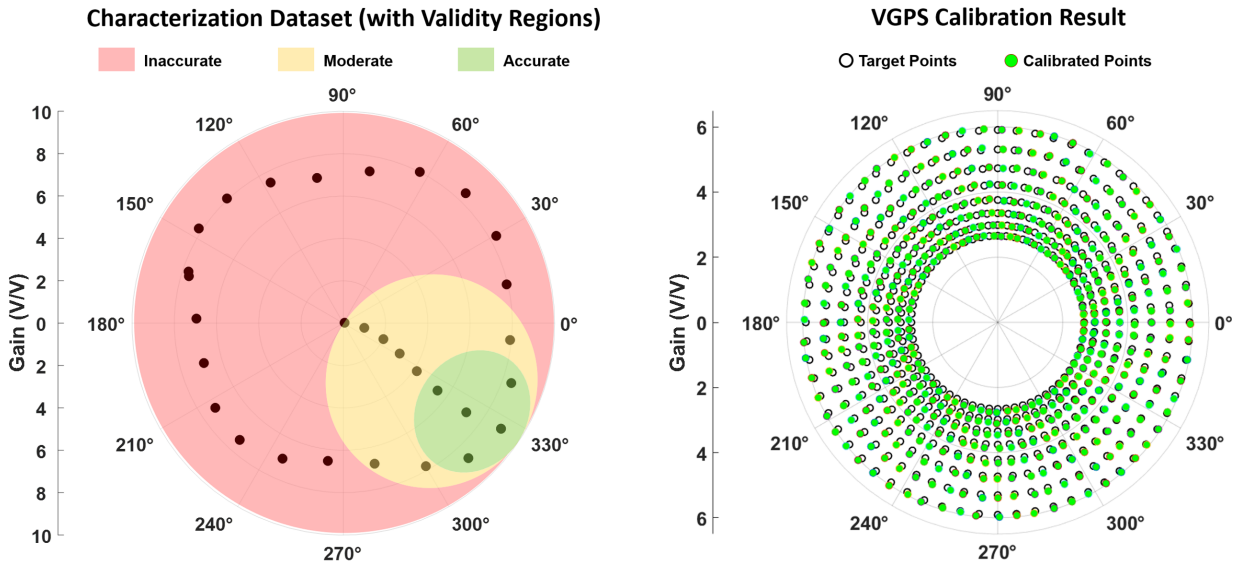


Figure 4.18: Example calibration method demonstrating the regionality of the characterization dataset. (a) Characterization dataset validity; (b) Corresponding calibration result.

From the measured transformation dataset, we identify two directions of maximum errors as the directions furthest from the directions of the acquired transformation data:

$$\theta_{max\ error} = \frac{1}{2}\big(phase(T_{mid,main}) + phase(T_{mid,aux})\big) + 0/\pi \tag{4.94}$$

Using the directions of maximum errors, along with the targeting gain of the targeting channel G_t as discussed in the tapering awareness section in 3.2.8, the two test points are

calculated as:

$$P_{test1} = G_t \cdot e^{j\frac{1}{2}\left(phase(T_{mid,main})+phase(T_{mid,aux})\right)} \tag{4.95}$$

$$P_{test2} = G_t \cdot e^{j\frac{1}{2}\left(phase(T_{mid,main})+phase(T_{mid,aux})\right)+\pi} \tag{4.96}$$

As illustrated in the figure 4.19 below, the two test points are along the two maximum error phase directions and at the targeting gain state.

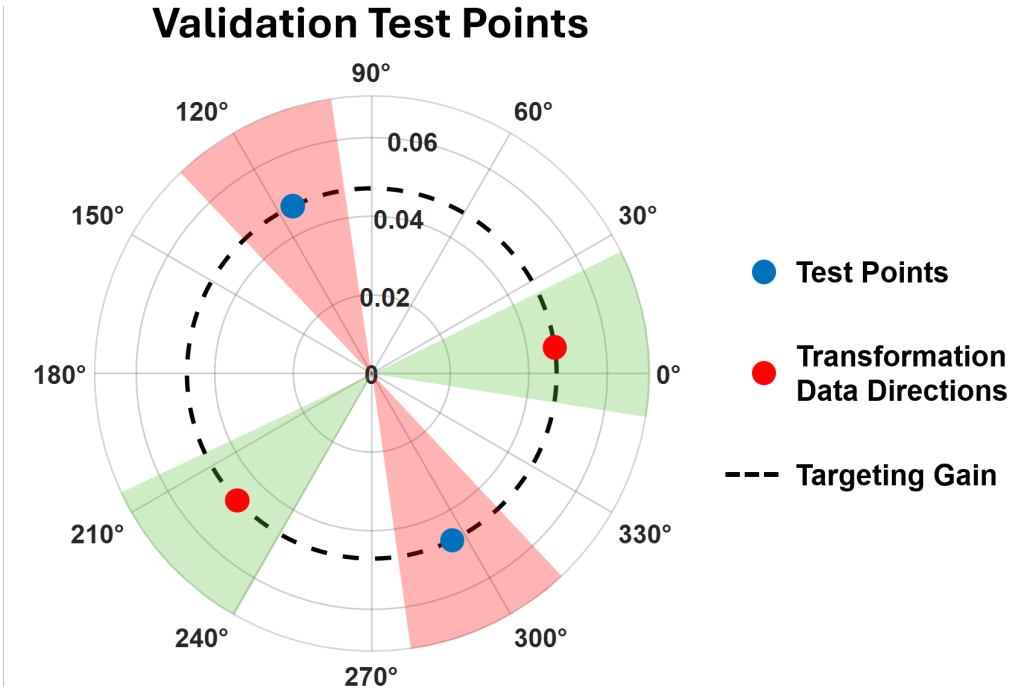


Figure 4.19: Transformation validation test points.

The measured points from these two test points are validated using the distance criterion introduced in Section 3.3.3. Since the synthesized mapping functions are less accurate than the fully characterized mapping functions, it is reasonable to assume worse performance than the fully characterized calibration. Therefore, it is recommended to loosen the validation region (lower validation tolerance coefficient) for a higher success rate.

The objective of channel transformation is to minimize the number of measurements. Repeated validation increases the number of measurements required. Thus, the algorithm acquires test points progressively to invalidate the synthesized mapping functions as early as possible. A channel needs to pass both test points to be validated, but it only needs to fail one test point to be invalidated.

4.4 Array Elements Similarity Sequencing

4.4.1 Overview

The objective of Array Elements Similarity Sequencing (AESS) is to achieve the maximum transformation success rate. By sequencing the elements so that the transformation occurs between similar channels, channel transformation becomes more deliberate and successful more often.

AESS analyzes the outline data of all channels, extracts the similarity between elements, and sequences them to ensure the transformation occurs between reference and targeting channels that have similar responses. Figure 4.20 shows the flow chart of AESS.

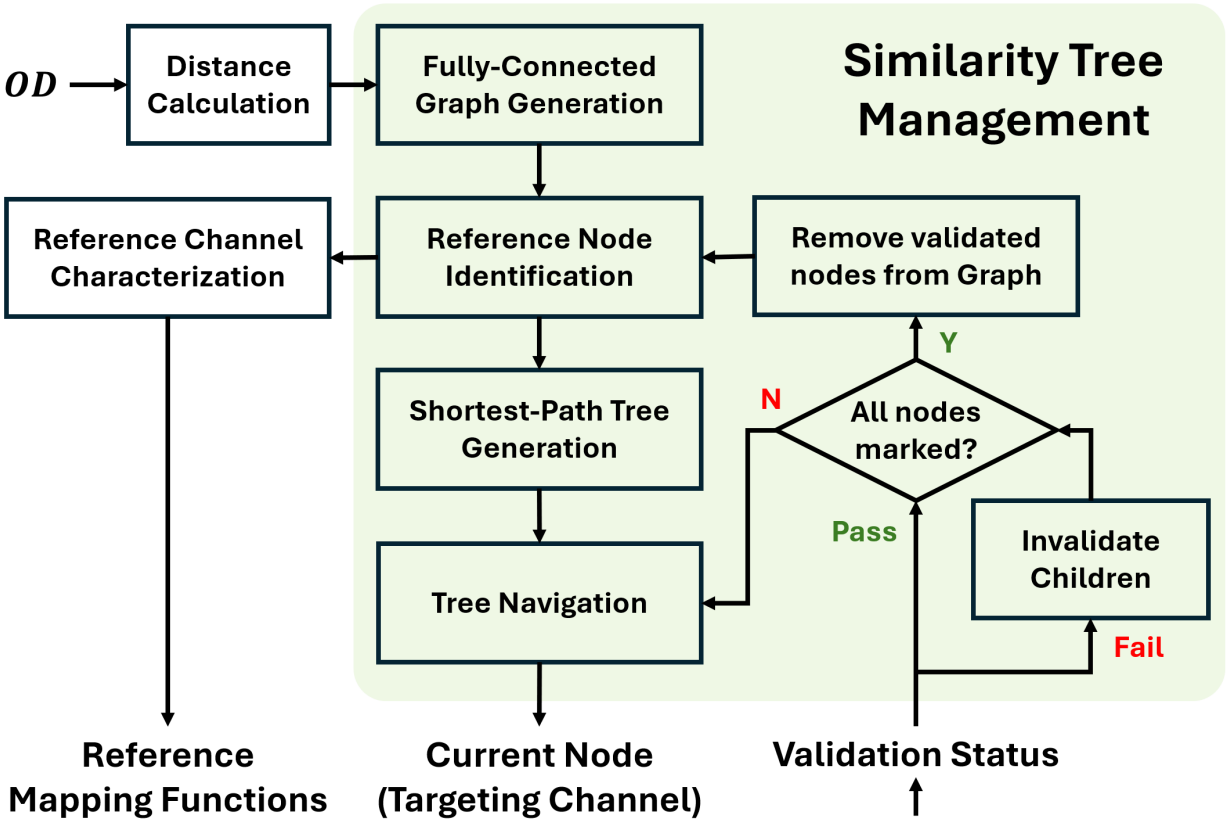


Figure 4.20: Array Elements Similarity Sequencing flow diagram.

As discussed in the introduction of channel transformation, gain envelopes (GE), magnitudes of outline data, are excellent candidates for channel identification due to their unpredictability across channels and their characteristic of enclosing the shape of the constellation.

As depicted in figure 4.20, AESS interfaces with channel transformation by providing the reference mapping functions and the targeting channel, and it receives the result of the transformation validation.

Adopting a one-to-multiple sequencing scheme, AESS uses a tree data structure for navigating from the reference node "root" to the targeting node "children." In the complete flow chart of the channel transformation routine shown in Figure 4.6, this block is referred to as "Similarity Tree Management" and acts as the control unit for channel transformation.

From the outline data of all elements, the algorithm calculates the "distance matrix," which specifies the reciprocal "distance" between the responses of different array elements. From the distance matrix, a fully connected graph is generated, with the number of nodes equal to the number of elements in the array.

To identify the optimal reference node, a minimum-spanning tree (MST) is generated from the fully connected graph. The MST is an undirected graph that connects all vertices together without any cycles and with the minimum possible total edge weight. From the MST, the center node, which has the minimum total distance to the other nodes, is selected as the reference, and the reference mapping functions are generated.

After selecting the reference node, a shortest-path tree, referred to as the "similarity tree", is generated with the reference node as the root, revealing a layered structure that shows the hierarchy of distances from the targeting channels to the reference. Exploiting the properties of a shortest-path tree, the children are always further away from the root than their parents. Thus, if the distance definition is accurate, the algorithm does not need to attempt transformation to the children if their parent fails the transformation.

After every node other than the root is either marked as "invalid" or "valid," the algorithm removes all the validated nodes and the root from the graph, and the process repeats by choosing a new reference.

In the following sections, we will discuss in detail the definition of distance, the identification of the reference channel, and the management and navigation of the similarity tree.

4.4.2 Distance Definition

AESS uses the outline data, specifically the gain envelopes, to determine the "distance" between element responses. From the section on mapping functions synthesis, minimizing the "distance" between two channels means maximizing the shape similarity in their gain envelopes. This, in turn, improves $GESP$ and $PPSP$ synthesis, thereby enhancing the transformation accuracy.

For the calculated distance to be meaningful, it must satisfy the "distance-to-success linearity rule". This rule states that, from a given channel, if the transformation fails for a closer target, it will fail for a further target; conversely, if the transformation succeeds for a further target, it will succeed for a closer target. The rule is formulated as follows:

$$if\ T_{i\to j} = 0\ and\ D_{i\to j} < D_{i\to k}, \quad then\ T_{i\to k} = 0 \tag{4.97}$$

$$if\ T_{i\to j} = 1\ and\ D_{i\to j} > D_{i\to k}, \quad then\ T_{i\to k} = 1 \tag{4.98}$$

where $T_{i\to j}$ signifies the transformation validation status from channel i to channel j and $D_{i\to j}$ signifies the distance from channel i to channel j.

To maximally adhere to this rule, the distance needs to reflect the probability of transformation success based on the gain envelopes of the reference and targeting channels. As discussed in the mapping functions synthesis section, the synthesis handles scaling as well as magnitude and phase shifting of the mapping functions across channels. Thus, the distance should be indifferent to the magnitude and phase in the gain envelopes. Since $GESP$ synthesis depends on the phase of the fundamental tone in the gain envelope, similar gain envelopes in shape should correspond to a similar fundamental tone fractional power and subsequently more accurate phase shift detection. Therefore, the correlation coefficient is used to quantify the linear dependence between the two gain envelopes, indicating their shape similarities.

Let $D_{i\to j}$ be the distance from channel i to channel j, with gain envelopes GE_i and GE_j respectively. Since there should be no difference in transforming from either channel to the other, the distance should be reciprocal. Let $D_{i,j}$ be the reciprocal distance between channel i and channel j:

$$D_{i,j} = D_{i\to j} = D_{j\to i} \tag{4.99}$$

Using the correlation coefficient ρ between the gain envelopes of the two channels, the

distance between channel i and channel j is calculated as:

$$D_{i,j} = 1 - |\rho(GE_i, GE_j)| \tag{4.100}$$

$$= 1 - \left| \frac{\sum_{k=1}^{n}(GE_{i,k} - \overline{GE_i})(GE_{j,k} - \overline{GE_j})}{\sqrt{\sum_{k=1}^{n}(GE_{i,k} - \overline{GE_i})^2}\sqrt{\sum_{k=1}^{n}(GE_{j,k} - \overline{GE_j})^2}} \right| \tag{4.101}$$

where n is the outline data sampling size (the length of GE), $GE_{i,k}$ and $GE_{j,k}$ are the k-th samples in GE_i and GE_j, respectively, and $\overline{GE_i}$ and $\overline{GE_j}$ are the means of GE_i and GE_j, respectively.

For an array of size N, the distance matrix $\boldsymbol{D}$ is of size $N \times N$ and is defined as:

$$\boldsymbol{D} = \begin{bmatrix} 0 & D_{1\to2} & \cdots & D_{1\to N} \\ D_{2\to1} & 0 & \cdots & D_{2\to N} \\ \vdots & \vdots & \ddots & \vdots \\ D_{N\to1} & D_{N\to2} & \cdots & 0 \end{bmatrix} \tag{4.102}$$

and since the distance is reciprocal:

$$\boldsymbol{D} = \begin{bmatrix} 0 & D_{1,2} & \cdots & D_{1,N} \\ D_{1,2} & 0 & \cdots & D_{2,N} \\ \vdots & \vdots & \ddots & \vdots \\ D_{1,N} & D_{2,N} & \cdots & 0 \end{bmatrix} \tag{4.103}$$

The algorithm then uses $\boldsymbol{D}$ to generate the fully-connected graph and proceeds to determine the reference node as discussed in the sections below.

4.4.3 Reference Channel Identification

As outlined in the flow chart in figure 4.20, AESS takes the $N \times N$ distance matrix $\boldsymbol{D}$ and finds the optimum reference node. First, a fully-connected graph is generated from $\boldsymbol{D}$ using each column (or row) entry as the nodes and the vector in that column (or row) as the edge costs. The generated graph, depicted in figure 4.21a, has N nodes and has weighted edges with the distances as the costs.

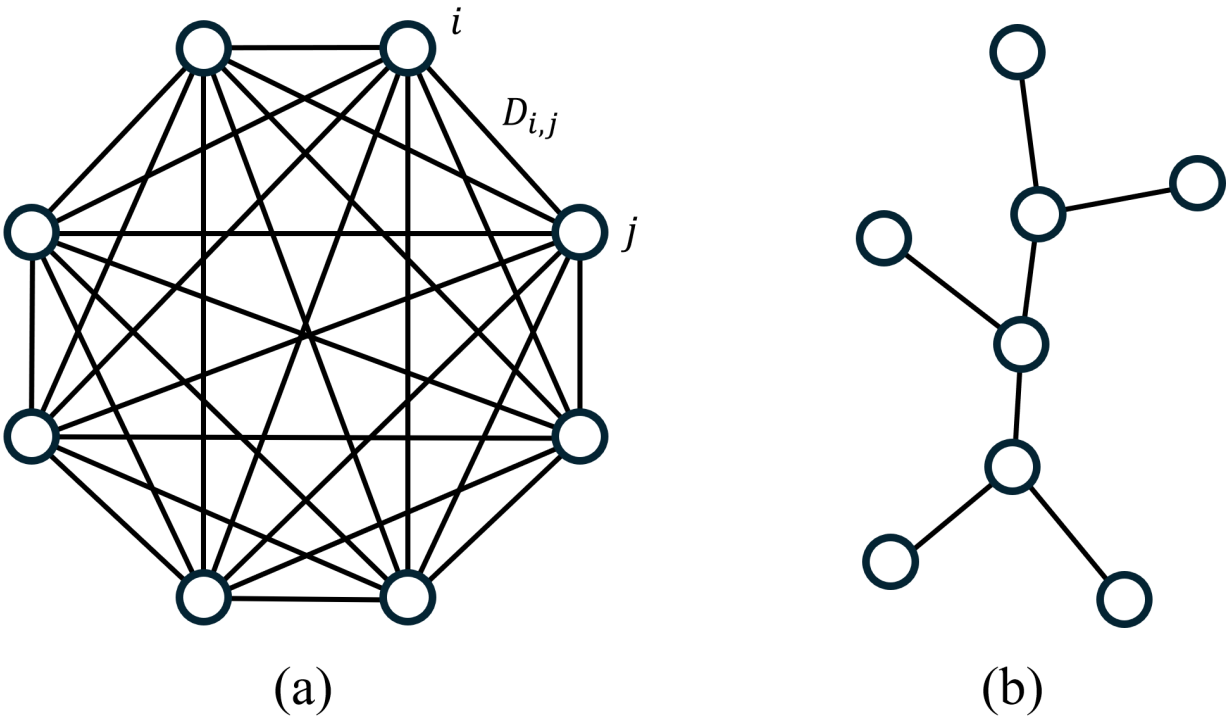


Figure 4.21: Illustration of the fully-connected graph and the generated minimum-spanning tree: (a) Fully-connected Graph; (b) Generated minimum-spanning tree (MST).

From the graph, a minimum-spanning tree (MST) is generated, connecting all the nodes together without cycles and with the minimum total cost. As illustrated in Figure 4.21, the MST provides an optimized connection for the nodes, thus maximizing the total transformation success rate. According to graph theory, the center of the MST is the node (or nodes) with the smallest maximum distance to all other nodes. By selecting the center node as the reference, we minimize the maximum path in the MST, ensuring that the reference node has relatively short paths to all other nodes and optimizing overall

transformation efficiency. Additionally, the center node is likely to be equidistant to the other nodes, reducing the risk of disproportionately long paths to some nodes. This means that the failure of any single node will have less impact on the overall transformation process. After the reference node is identified, the reference channel is fully characterized and the resulting reference mapping functions are generated.

To find the center node of the MST, the nodes with the lowest degree (number of edges connected to them) are iteratively removed from the MST until only one or two nodes remain. In the case of two nodes remaining, the reference node is selected as the one with the lowest total costs to all other nodes in the current graph. This process is illustrated in Figure 4.22.

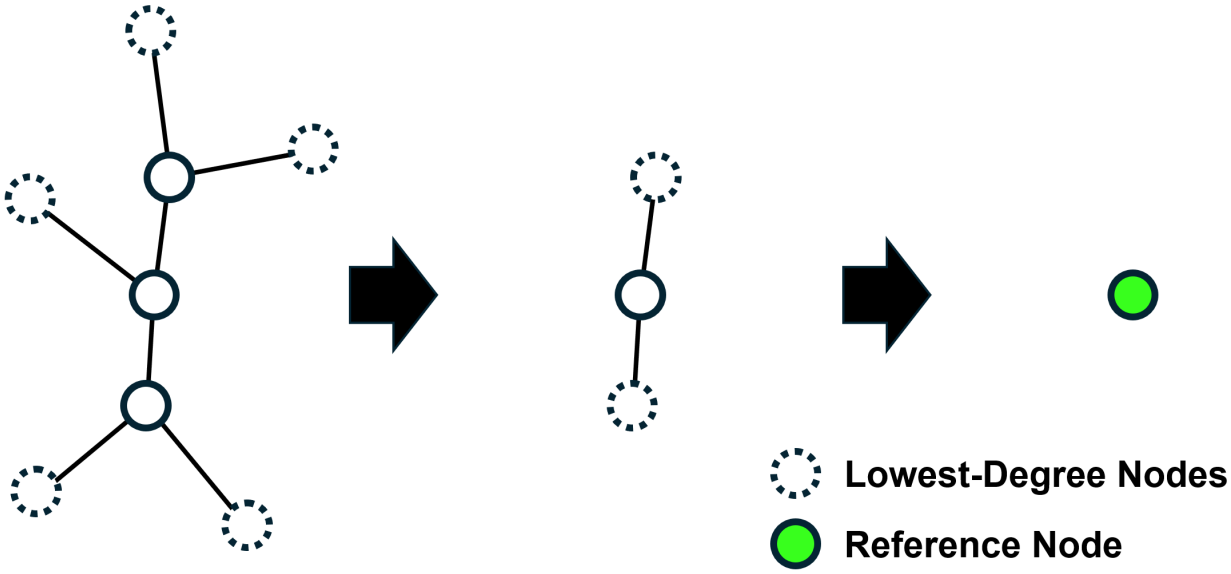


Figure 4.22: Illustration of the process of finding the reference node.

With a reference node identified, the objective of the tree shifts from minimizing the total cost to minimizing the individual path length from the other nodes to the reference. Thus, a shortest-path tree (SPT) is generated from the current graph with the reference node as the root. More details are discussed in the next section.

4.4.4 Similarity Tree Navigation and Management

With the reference node selected, a shortest-path tree (SPT) is generated to optimize the node path to the reference. As shown in Figure 4.23, the SPT illustrates the targeting channels (the rest of the nodes) connecting to the reference channel (the root node) in a hierarchical manner, showing levels of similarity. Note that the SPT is only used for displaying the similarity hierarchy of the nodes; the paths in the SPT do not represent the actual transformation paths, as the transformation occurs directly from the reference node to the targeting nodes. Therefore, for a node of level 2 or below, if the direct connection to the reference node is dropped, it does not imply that the transformation occurs through its parent node.

From the properties of an SPT, the children are always further in distance from the root than their parent node. If the "distance-to-success linearity rule" holds, then the algorithm does not need to attempt the transformation of the children if the transformation to their parent node fails.

In the full SPT demonstrated in Figure 4.23, the similarity levels of the nodes are determined by the length of the connections from them to the root. The transformation progresses for nodes at one level before progressing to the next level. As illustrated in Figure 4.23, if the transformation from node a to node e fails, the algorithm invalidates node e and its children (g and h), marking them as failing the transformation.

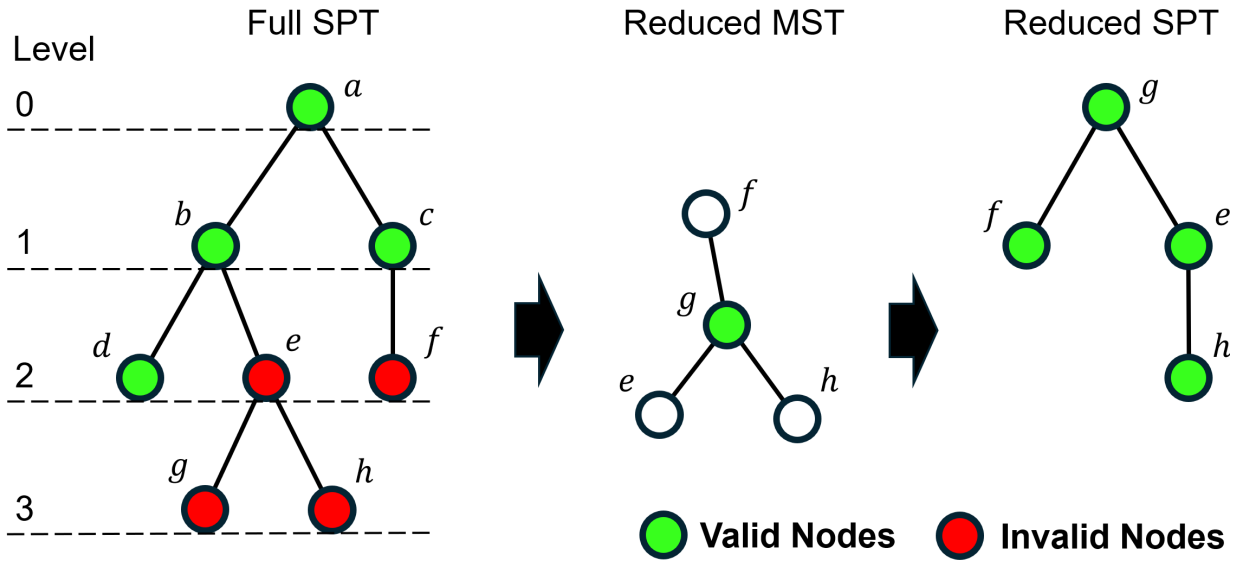


Figure 4.23: Illustration of the process of tree navigation and management.

Once all the nodes in the SPT are either marked as "valid" or "invalid," the algorithm drops all the validated nodes from the fully connected graph, leaving only the invalid nodes, as described in the flow chart in Figure 4.20. Then a reduced MST is generated from the reduced fully connected graph, and a new reference is selected among the previously invalid nodes. From the reduced MST, a reduced SPT is generated, showing the updated similarity hierarchy of the remaining nodes. The transformation then proceeds from the new reference node to the targeting nodes according to the similarity levels. This process is repeated until all the nodes are validated, at which point the channel transformation is complete.

4.5 Dynamic Outline Sampling

To ensure the Array Elements Similarity Sequencing (AESS) sequences the elements properly and to determine the targeting gains of each element for a desired gain taper, the outline data of each element is acquired as the first step in channel transformation, as depicted in Figure 4.6. Since the objective of channel transformation is to minimize the number of measurements for array calibration, fully measuring the outline data of every channel heavily increases the number of measurements. Thus, the algorithm needs to use the minimum outline data sampling size possible without disrupting the AESS and the setting of targeting gains.

Dynamic outline sampling is a process that detects the minimum outline data sampling size that still allows the proper operation of AESS and the setting of targeting gains. For the first channel, the outline data is sampled with a specified outline data sampling size N_{OD} that is sufficient to capture the frequency contents in the gain envelope (the magnitudes of the outline data). The algorithm then identifies the sampling size that captures 90% of the power in the frequency domain. Using this reduced sampling size (referred to as the dynamic sampling size N'_{OD}), the resulting gain envelope maintains the majority of its features, thus not affecting the AESS.

To allow the action of dynamic outline sampling to be transparent to the other parts of channel transformation and even the control code solver, the outline data using the original sampling size is reconstructed from the dynamically sampled outline data.

In this section, we discuss in detail the process of calculating the dynamic sampling size and reconstructing the outline data.

4.5.1 Dynamic Sampling Size

With the outline data of channel 1 sampled with the specified outline data sampling size N_{OD}, the dynamic sampling size N'_{OD} is calculated as the sampling size that captures 90% of the power present in the frequency domain of the captured gain envelope of channel 1. The dynamic sampling size is calculated as:

$$N'_{OD} = 2\left(\min\left\{k \;\middle|\; \frac{\sum_{i=1}^{k}|X_i|}{\sum_{i=1}^{N_{OD}/2+1}|X_i|} \geq 0.9\right\} - 1\right) \tag{4.104}$$

where X_i represents the i-th component of the Fourier transform of the gain envelope of channel 1.

Figure 4.24 shows an example fast Fourier transform of the gain envelope of channel 1. We see that the k in (4.104) is 8 thus the N'_{OD} is calculated to be 14.

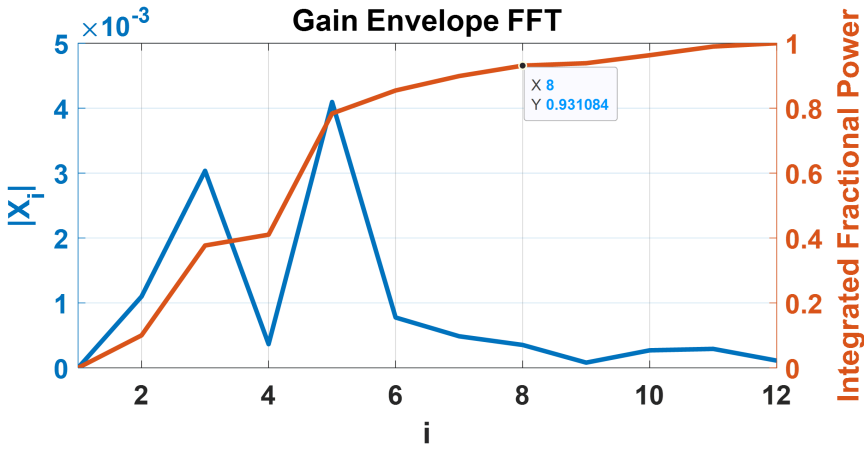


Figure 4.24: Example of the calculation of the dynamic sampling size.

4.5.2 Outline Data Reconstruction

To reconstruct the outline data OD of the original sampling size N_{OD} from the dynamically sampled outline data OD' with a dynamic sampling size N'_{OD}, the OD' is interpolated at the original sampling indexes using N_{OD}. Since the outline data is complex, the interpolation is done by individually interpolating the magnitude (gain envelope) and phase (phase profile) of the OD'.

$$OD(I_\theta) = |OD'(I_\theta)| \cdot e^{j \cdot phase(OD'(I_\theta))}, \quad for\ I_\theta \in \{I_{\theta,min}, ..., I_{\theta,max}\} \tag{4.105}$$

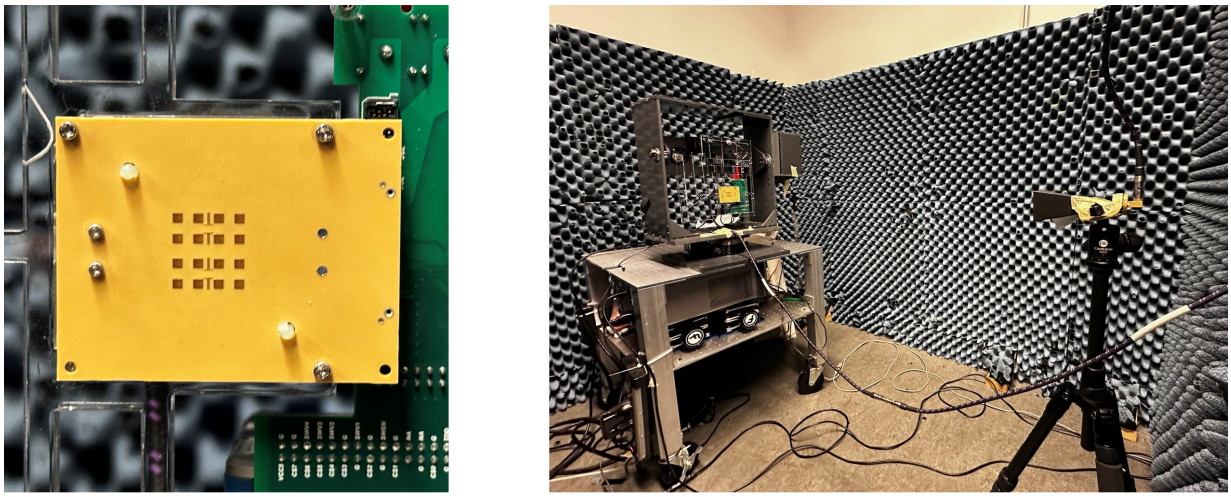
4.6 Experimental Validation

The proposed channel transformation routine is tested on the 4×4 BFIC1 array and the 4×4 BFIC2 array. The measurement is conducted at 25 degrees Celsius and at 38.5GHz which is the center frequency of the two arrays' rated frequency range.

For the array calibrations in this section, we include the measurement and calibration setup, the table showing the constellation performance and the radiation patterns. Additionally, if AESS is applied, the similarity trees are also included showing the transformation path.

4.6.1 4×4 BFIC1 Array Calibration

4×4 BFIC1 Array Measurement Setup



(a) (b)

Figure 4.25: Measurement setup for 4×4 BFIC1 array: (a) Array close up; (b) Setup picture.

Figure 4.25 below shows the array and the measurement setup. The measurement is conducted in the far-field with the array mounted on a horizontally rotating motor, pointing at a horn antenna. The algorithm runs in MATLAB on a PC, which communicates with the National Instruments controller (NI-852) to send control bits to the BFICs on the

array. The array is powered by a ROHDE & SCHWARZ NGE 100 DC power supply. The measurement instrument, a Keysight N5247B PNA-X vector network analyzer, measures the S-parameters of the link from the array to the horn antenna. During calibration, each array channel is turned on individually while the other channels are turned off. The measured S-parameters are then sent to the PC and processed by the algorithm.

4×4 BFIC1 Array Calibration Setup

In this section, the mapping functions generated by the proposed channel transformation technique are used in the unsupervised calibration routine proposed in Chapter 3 for array calibration. The results of the channel transformation are compared to the unsupervised calibration using the fully characterized mapping functions proposed in Chapter 3, as well as the exhaustive search method. Channel transformation employs the proposed taper awareness to set the targeting gains for the desired taper.

The taper used in this calibration is the Taylor window taper, targeting a side-lobe level (SLL) of -17.7 dB. The proposed characterization method uses an outline data sampling size of 23 and a gain data sampling size of 8. The transformation validation uses a validation tolerance coefficient T of 1.5, and dynamic outline sampling is enabled.

In the scenario where AESS is not used, the transformation occurs in a linear sequence from the first channel to the last channel. If a channel fails the transformation validation, it is immediately selected as the new reference for subsequent transformations.

4×4 BFIC1 Array Constellation Performance

From Table 4.1, we can see that channel transformation achieves constellation results comparable to full characterization while requiring significantly fewer measurements. Compared to the exhaustive search method, the proposed method accelerates array calibration from 1100 times with the full characterization method to approximately 3000 times with channel transformation using AESS, finishing the calibration in just over 2 minutes compared to the 7 days required by the exhaustive search method.

Comparing channel transformation with and without AESS, we observe that characterization requires fewer measurements when AESS is enabled due to the increased transformation success rate. However, this increased success rate comes with a slight decrease in calibration accuracy. This is because, without AESS, a failed transformation triggers a full characterization of the channel, which is more accurate than channel transformation.

Table 4.1: 4x4 BFIC1 array calibration results comparison. The proposed methods are using the unsupervised routine with either full characterization or channel transformation.

	Exhaustive	**Full Charac.**	**Trans. w/o AESS**	**Trans. w/ AESS**
Gain Taper Aware (Targeting one gain state for each element)				
Phase RMSE (°)	0.41	0.62	1.07	1.12
Gain RMSE (dB)	0.02	0.05	0.13	0.16
EVM (%)	0.77	1.23	2.37	2.69
# of Measurements	1048576	928	526	361
Calibration Time	7d	331.7s	190.5s	131.8s

4×4 BFIC1 Array AESS Progression

Figure 4.26 shows the shortest-path trees generated by AESS during channel transformation. Figure shows a defined hierarchy and the transformation only uses two references.

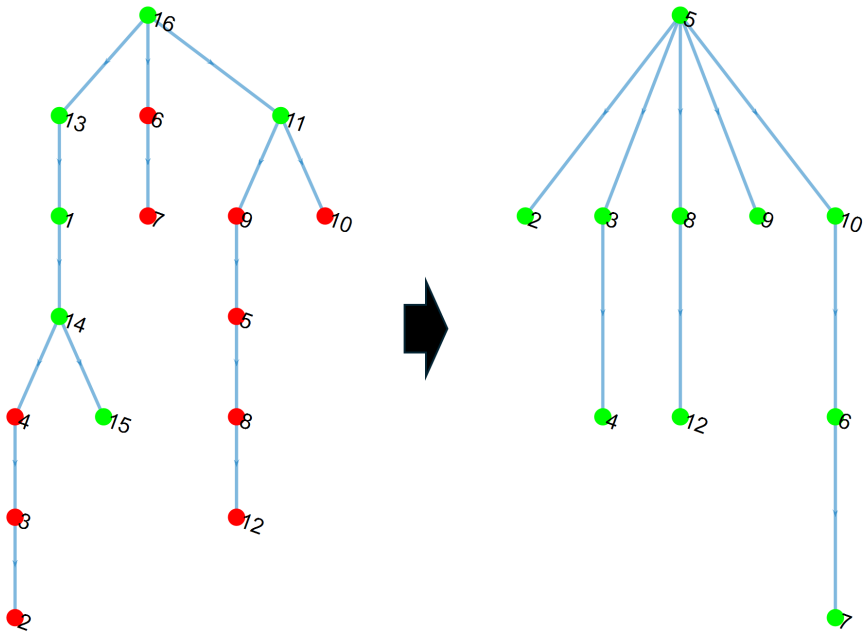


Figure 4.26: Channel transformation with AESS shortest-path trees for the 4×4 BFIC1 array showing transformation progressions.

4×4 BFIC1 Array Radiation Pattern

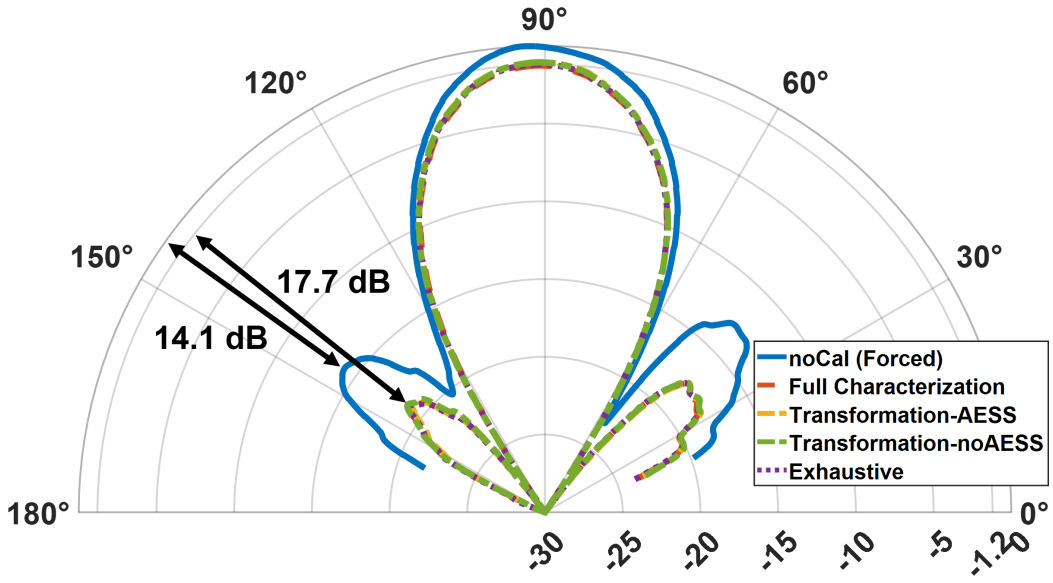
In this subsection, the effects of the proposed channel transformation techniques on the array radiation pattern are experimentally validated and compared to the proposed full characterization and the exhaustive search method. Figure 4.27 shows the measured array radiation patterns, including the "noCal" (no calibration), unsupervised calibration using fully characterized mapping functions, synthesized mapping functions from channel transformations with and without AESS, and the gold reference exhaustive search. Specifically, Figure 4.27a shows the radiation patterns at the board side, while Figure 4.27b shows the beam-steered radiation patterns pointed at -30 degrees.

To ensure the measured radiations reflect the theoretical gain tapering assumption that the array elements are isotropic, the radiations in Figure 4.27a are measured with a fixed motor position while the beam is electrically steered. The beam-steered radiation pattern in Figure 4.27b is measured using the mechanically rotating motor.

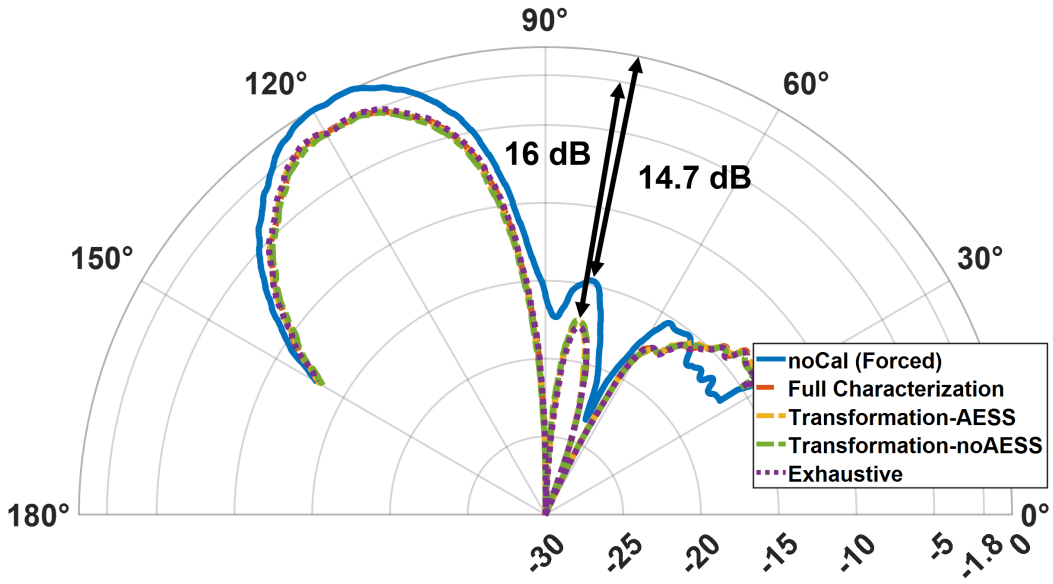
For all scenarios, the radiation patterns of channel transformation remain virtually identical to both the proposed fully characterized method and the exhaustive search method, demonstrating excellent calibration accuracy. The slight imbalance in the calibrated radiation patterns could be due to their passive calibration nature, which omits the effects of dynamic current loading and active antenna couplings. As indicated by the findings in [5], this imbalance in passive calibration can be corrected in active calibration, where the array is calibrated using the proposed methods with all elements turned "ON".

For the radiation pattern pointed at the board side shown in Figure 4.27a, all the calibrated radiations align and have a SLL of -17.7 dB, matching the theoretical value. The "noCal" method, not compatible with gain taper awareness, applies a "forced" taper on the array's gain states. The "noCal" radiation achieves an SLL of -14.1 dB, which significantly deviates from the theoretical -17.7 dB.

For demonstrating beam-steering, Figure 4.27b shows the mechanically-steered radiation of all methods with the beam steered to -30 degrees. The calibrated radiations of all methods remain consistent while steered, exhibiting excellent pointing accuracy but a deteriorated SLL compared to the radiation pointed at the board side. As expected, the "noCal" method has the worst SLL and the shallowest nulls.



(a)

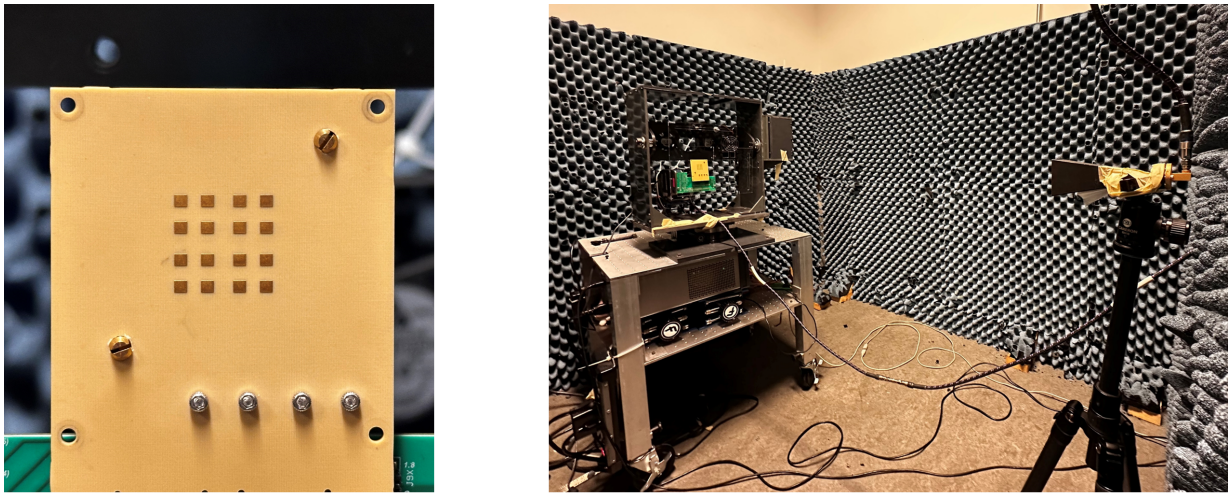


(b)

Figure 4.27: Measured radiation pattern of the 4x4 BFIC1 array. The proposed methods are using the unsupervised calibration routine: (a) Electrically-steered radiation pattern with the beam pointed at the board side; (d) Mechanically-steered radiation pattern with the beam pointed at -30 degrees.

4.6.2 4×4 BFIC2 Array Calibration

4×4 BFIC2 Array Measurement Setup



(a) (b)

Figure 4.28: Measurement setup for 4×4 BFIC2 array: (a) Array close up; (b) Setup picture.

Figure 4.28 shows the array and the measurement setup. The measurement is conducted in the far-field with the array mounted on a horizontally rotating motor, pointing at a horn antenna. The algorithm runs in MATLAB on a PC, which communicates with the National Instruments controller (NI-852) to send control bits to the BFICs on the array. The array is powered by a ROHDE & SCHWARZ NGE 100 DC power supply. The measurement instrument, a Keysight N5247B PNA-X vector network analyzer, measures the S-parameters of the link from the array to the horn antenna. During calibration, each array channel is turned on individually while the other channels are turned off. The measured S-parameters are then sent to the PC and processed by the algorithm.

4×4 BFIC2 Array Calibration Setup

In this section, the mapping functions generated by the proposed channel transformation technique are used in the unsupervised calibration routine proposed in Chapter 3 for array calibration. The results of the channel transformation are compared to the unsupervised

calibration using the fully characterized mapping functions proposed in Chapter 3, as well as the exhaustive search method. Channel transformation employs the proposed taper awareness to set the targeting gains for the desired taper.

The taper used in this calibration is the Taylor window taper, targeting a side-lobe level (SLL) of -15.8 dB. The proposed characterization method uses an outline data sampling size of 10 and a gain data sampling size of 4. The transformation validation uses a validation tolerance coefficient T of 1, and dynamic outline sampling is disabled, meaning the outline data of each element is acquired using the specified outline data sampling size.

In the scenario where AESS is not used, the transformation occurs in a linear sequence from the first channel to the last channel. If a channel fails the transformation validation, it is immediately selected as the new reference for subsequent transformations.

4×4 BFIC2 Array Constellation Performance

Table 4.2: 4x4 BFIC2 array calibration results comparison. The proposed methods are using the unsupervised routine with either full characterization or channel transformation.

	Exhaustive	**Full Charac.**	**Trans. w/o AESS**	**Trans. w/ AESS**
Gain Taper Aware (Targeting one gain state for each element)				
Phase RMSE (°)	2.02	2.69	3.01	3.02
Gain RMSE (dB)	0.17	0.39	0.47	0.54
EVM (%)	4.05	6.43	7.35	7.97
# of Measurements	16384	384	346	272
Calibration Time	1h 22m	117s	106s	82s

From Table 4.2, we can see that channel transformation achieves constellation results comparable to full characterization while requiring significantly fewer measurements. Compared to the exhaustive search method, the proposed method accelerates array calibration from 40 times with the full characterization method to 60 times with channel transformation using AESS, finishing the calibration in just over 1 minute compared to the one and a half hours required by the exhaustive search method.

Comparing channel transformation with and without AESS, we observe that characterization requires fewer measurements when AESS is enabled due to the increased transformation success rate. However, this increased success rate comes with a slight decrease

in calibration accuracy. This is because, without AESS, a failed transformation triggers a full characterization of the channel, which is more accurate than channel transformation.

4×4 BFIC2 Array AESS Progression

Figure 4.29 shows the shortest-path trees generated by AESS during channel transformation. The figure shows a defined hierarchy and the transformation only uses four references.

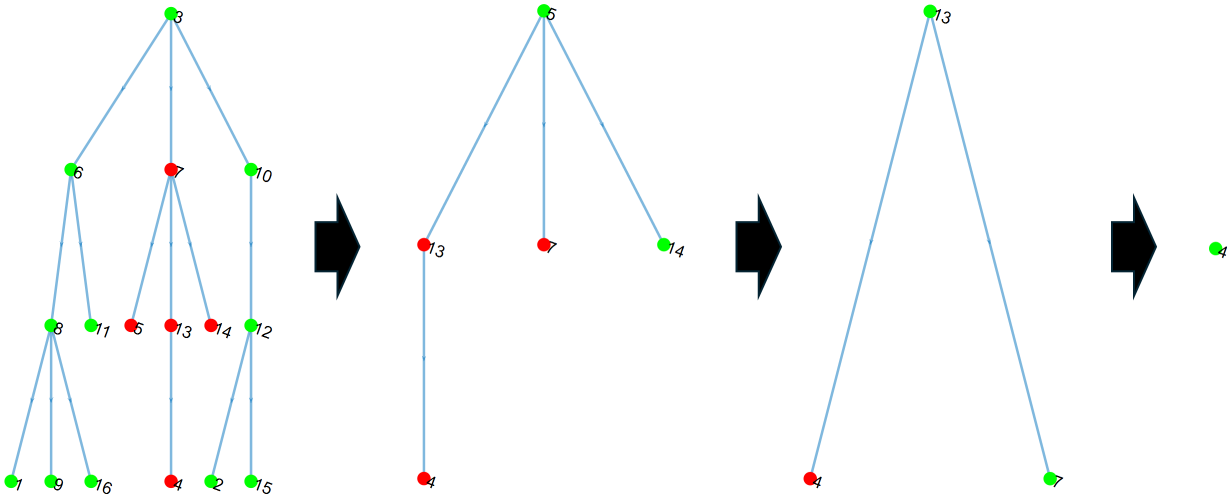


Figure 4.29: Channel transformation with AESS shortest-path trees for the 4×4 BFIC2 array showing transformation progressions.

4×4 BFIC2 Array Radiation Pattern

In this subsection, the effects of the proposed channel transformation techniques on the array radiation pattern are experimentally validated and compared to the proposed full characterization and the exhaustive search method. Figure 4.30 shows the measured array radiation patterns, including the "noCal" (no calibration), unsupervised calibration using fully characterized mapping functions, synthesized mapping functions from channel transformations with and without AESS, and the gold reference exhaustive search. Specifically, Figure 4.30a shows the radiation patterns at the board side, while Figure 4.30b shows the beam-steered radiation patterns pointed at -30 degrees.

To ensure the measured radiations reflect the theoretical gain tapering assumption that the array elements are isotropic, the radiations in Figure 4.30a are measured with a fixed motor position while the beam is electrically steered. The beam-steered radiation pattern in Figure 4.30b is measured using the mechanically rotating motor.

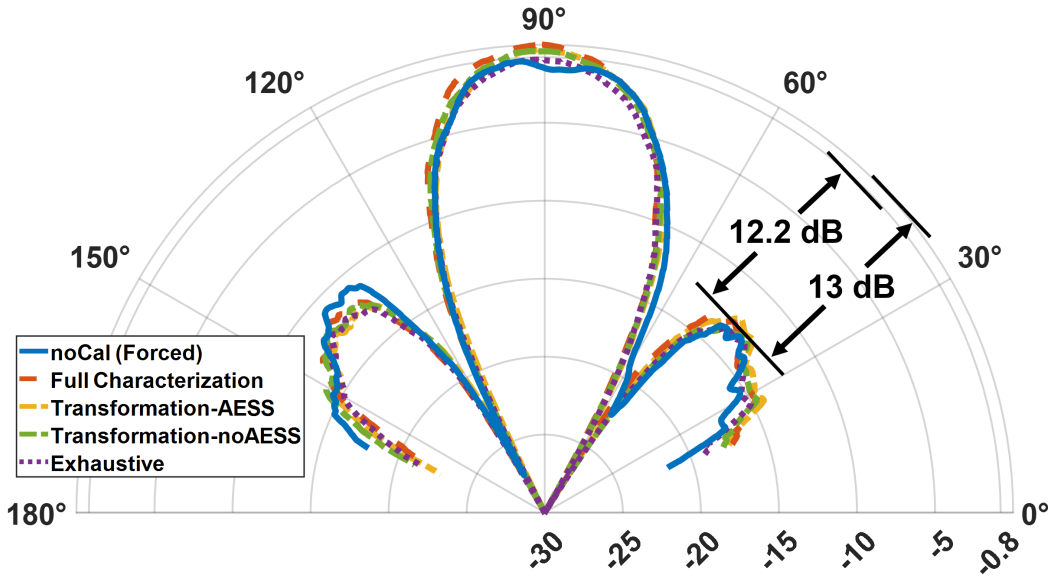
For all scenarios, the radiation patterns of channel transformation remain similar to both the proposed fully characterized method and the exhaustive search method, demonstrating excellent calibration accuracy. The slight imbalance in the calibrated radiation patterns could be due to their passive calibration nature, which omits the effects of dynamic current loading and active antenna couplings. As indicated by the findings in [5], this imbalance in passive calibration can be corrected in active calibration, where the array is calibrated using the proposed methods with all elements turned "ON".

For the radiation pattern pointed at the board side shown in Figure 4.30a, all the radiation patterns roughly align, with the radiation patterns from the full characterization and both transformations peaking slightly higher than the "noCal" and exhaustive search methods and achieving a slightly better SLL of -13 dB compared to the -12.2 dB of the other methods. Note that the achieved SLL of all methods significantly deviates from the theoretical -15.8 dB. This is due to significant power variations between elements in the BFIC2 array, and its BFIC's limited gain tuning range causes the targeted gain states to be clipped, preventing the desired taper from being produced accurately.

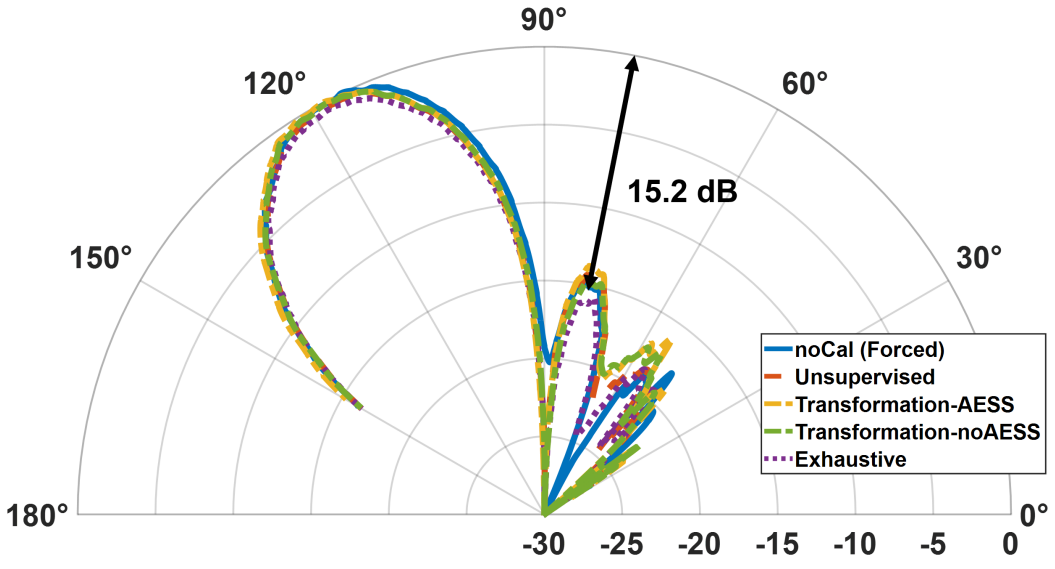
For demonstrating beam-steering, Figure 4.30b shows the mechanically-steered radiation pattern of all methods with the beam steered to -30 degrees. The calibrated radiations of all methods remain consistent while steered, exhibiting excellent pointing accuracy and a lower SLL of -15.2 dB compared to the radiation pointed at the board side. The "noCal" method has about the same SLL as the other calibrated radiation patterns but exhibits the shallowest nulls close to the main lobe.

4.7 Remarks

From the experimental results in Section 4.6, it is evident that the proposed channel transformation technique achieves calibrated constellations and array radiation patterns comparable to those obtained with the fully characterized method and the exhaustive search method, but with significantly fewer measurements, even compared to the proposed full characterization. Comparing the calibration results of the two arrays, the advantages of the proposed channel transformation are more pronounced with higher-resolution arrays and more continuous constellations. This is particularly evident in the BFIC1 array, where the transformation achieves a higher success rate.



(a)



(b)

Figure 4.30: Measured radiation pattern of the 4x4 BFIC2 array. The proposed methods are using the unsupervised calibration routine: (a) Electrically-steered radiation pattern with the beam pointed at the board side; (d) Mechanically-steered radiation pattern with the beam pointed at -30 degrees.

Chapter 5

Conclusion

This thesis introduces a novel constellation characterization method that enables the rapid calibration of beamforming integrated circuits (BFICs) and phased arrays. By measuring a strategically chosen dataset, the full two-dimensional responses of the array elements, accounting for varying control errors, are characterized and described using eleven mapping functions. These mapping functions are then utilized by a developed iterative solver to generate control codes for desired constellations.

To enhance the robustness of the proposed characterization method, a kernel search algorithm is developed for use in a closed-loop calibration routine, termed the supervised calibration routine, which actively verifies each control code solution for validated constellation calibration performance. Additionally, a taper awareness based scheme for setting targeting gains is proposed, maximizing the targeting gains of each element by accounting for the maximum power variations present in the array and the desired gain tapering profile.

When applied to two BFICs and two test arrays, our proposed calibration method demonstrates outstanding accuracy and efficiency compared to the exhaustive search method. For BFIC1 and its array, the proposed method achieves a calibration speed-up of up to 1100 times while maintaining similar constellation performance and identical radiation patterns. The efficacy is somewhat reduced when applied to BFIC2 and its array due to their reduced gain and phase tuning resolution and gain tuning range. Despite these limitations, the proposed methods still significantly reduce the number of measurements needed by up to 40 times compared to the exhaustive search method while achieving similar constellation performance and radiation patterns.

To further accelerate array calibration, a channel transformation technique is introduced

to explore the response similarities between each element in the array. By measuring the response differences between channels from the identified transformation dataset, the mapping functions can be transferred from one element to another with high accuracy, thus avoiding full characterization for each element. To increase the transformation success rate, the optimum transformation route is identified by the proposed array elements similarity sequencing technique. With the identified optimum sequence, the transformation success rate is maximized, achieving a substantial reduction in the number of measurements.

Validating the channel transformation technique, it is applied to the calibration of the two test arrays. The experimental result on the BFIC1 based test array shows an additional measurement reduction of approximately three times compared to the proposed full characterization method, resulting in an astounding 3000 times reduction compared to the exhaustive search method, while still achieving the same array radiation pattern as the full characterization and the exhaustive search method, highlighting its accuracy and efficiency. The experimental result on the BFIC2 based test array shows similar promise, achieving an additional 1.5 times measurement reduction compared to the proposed full characterization method, resulting in a 60 times reduction compared to the exhaustive search method while achieving the same array radiation pattern.

The proposed characterization and channel transformation techniques demonstrated significant advancements in phased array calibration in terms of calibration efficiency. They enable the feasibility of calibrating the varying control errors of future massive high-resolution MIMO systems and phased arrays.

References

[1] W. B. Group, "Digital Progress and Trends Report 2023," World Bank Group, Tech. Rep., 2023, https://openknowledge.worldbank.org/server/api/core/bitstreams/95fe55e9-f110-4ba8-933f-e65572e05395/content.

[2] K. Technologies, "3 Key Challenges Implementing and Testing MIMO and Beamforming in 5G Base Stations and Components," Keysight Technologies, Tech. Rep., 2020, https://www.keysight.com/us/en/assets/7018-06534/white-papers/5992-3752.pdf.

[3] A. Nafe, K. Kibaroglu, M. Sayginer, and G. M. Rebeiz, "An In-Situ Self-Test and Self-Calibration Technique Utilizing Antenna Mutual Coupling for 5G Multi-Beam TRX Phased Arrays," in *IEEE MTT-S International Microwave Symposium (IMS)*, 2019, pp. 1229–1232.

[4] T. Takahashi, Y. Konishi, S. Makino, H. Ohmine, and H. Nakaguro, "Fast Measurement Technique for Phased Array Calibration," *IEEE Transactions on Antennas and Propagation*, vol. 56, no. 7, pp. 1888–1899, 2008.

[5] A. B. Ayed, H. Jin, B. Tung, P. Mitran, and S. Boumaiza, "Array Calibration and Digital Predistortion Training Using Embedded Near-Field Feedback Probes and Orthogonal Coding for Enhancing the Performance of Millimeter-Wave Beamforming Arrays," *IEEE Microwave and Wireless Technology Letters*, vol. 33, no. 6, pp. 891–894, 2023.

[6] Cisco, "Cisco Annual Internet Report (2018–2023)," Cisco, Tech. Rep., 2020, https://www.cisco.com/c/en/us/solutions/collateral/executive-perspectives/annual-internet-report/white-paper-c11-741490.pdf.

[7] ——, "Edge-to-Enterprise IoT Analytics," 2017, https://blogs.cisco.com/datacenter/edge-to-enterprise. Accessed: 2024-06-05.

[8] S. Research, "Samsung 6G Vision," Samsung, Tech. Rep., 2020, https://cdn.codeground.org/nsr/downloads/researchareas/20201201_6G_Vision_web.pdf.

[9] Google, "Google is a Leader in The Forrester Wave™: AI Foundation Models for Language, Q2 2024," 2024, https://cloud.google.com/blog/products/ai-machine-learning/the-forrester-wave-ai-foundation-models-for-language-q2-2024. Accessed: 2024-06-05.

[10] A. Volenik, "Is Humane's Ai Pin Doomed? Company Seeks Buyer Amid Mixed Reviews," 2024, https://finance.yahoo.com/news/humanes-ai-pin-doomed-company-153016768.html. Accessed: 2024-06-05.

[11] D. Pierce, "Humane AI Pin review: not even close," 2024, https://www.theverge.com/24126502/humane-ai-pin-review. Accessed: 2024-06-05.

[12] Z. Li, J. Pang, Y. Zhang, Y. Yamazaki, Q. Wang, P. Luo, W. Chen, Y. Liao, M. Tang, Y. Wang, X. Fu, D. You, N. Oshima, S. Hori, J. Park, K. Kunihiro, A. Shirane, and K. Okada, "A 39-GHz CMOS Bidirectional Doherty Phased- Array Beamformer Using Shared-LUT DPD With Inter-Element Mismatch Compensation Technique for 5G Base Station," *IEEE Journal of Solid-State Circuits*, vol. 58, no. 4, pp. 901–914, 2023.

[13] Y. Wang, R. Wu, J. Pang, D. You, A. A. Fadila, R. Saengchan, X. Fu, D. Matsumoto, T. Nakamura, R. Kubozoe, M. Kawabuchi, B. Liu, H. Zhang, J. Qiu, H. Liu, N. Oshima, K. Motoi, S. Hori, K. Kunihiro, T. Kaneko, A. Shirane, and K. Okada, "A 39-GHz 64-Element Phased-Array Transceiver With Built-In Phase and Amplitude Calibrations for Large-Array 5G NR in 65-nm CMOS," *IEEE Journal of Solid-State Circuits*, vol. 55, no. 5, pp. 1249–1269, 2020.

[14] D. L. Yan, C. K. Sim, H. A. M. Arif, N. A. B. Kuyob, M. K. Raja, and K. T. C. Chai, "A 35mW, 2.32dB NF, 1.1° Phase Error, 18-21.2GHz Beamforming Receiver IC for Satcom on the Move (SOTM) Phased Arrays," *IEEE Transactions on Circuits and Systems II: Express Briefs*, vol. 70, no. 10, pp. 3847–3851, 2023.

[15] Y. Xiong, Y. Pu, Z. Yu, Y. Yao, X. Huang, and G. Wang, "A 2–20-GHz 360 ° Variable Gain Phase Shifter MMIC With Reverse-Slope Phase Compensation," *IEEE Transactions on Circuits and Systems I: Regular Papers*, pp. 1–14, 2023.

[16] B. Sadhu, A. Paidimarri, D. Liu, M. Yeck, C. Ozdag, Y. Tojo, W. Lee, K. X. Gu, J.-O. Plouchart, C. W. Baks, Y. Uemichi, S. Chakraborty, Y. Yamaguchi, N. Guan,

and A. Valdes-Garcia, "A 24–30-GHz 256-Element Dual-Polarized 5G Phased Array Using Fast On-Chip Beam Calculators and Magnetoelectric Dipole Antennas," *IEEE Journal of Solid-State Circuits*, vol. 57, no. 12, pp. 3599–3616, 2022.

[17] Y. Yamazaki, J. Sakamaki, J. Pang, J. Alvin, Z. Li, D. You, J. Mayeda, A. Shirane, and K. Okada, "A 37-43.5-GHz Phase and Amplitude Detection Circuit With 0.049° and 0.036-dB Accuracy for 5G Phased-Array Calibration Using Transformer-Based Injection-Enhanced ILFD," *IEEE Journal of Solid-State Circuits*, vol. 58, no. 10, pp. 2851–2860, 2023.

[18] A. Valdes-Garcia, S. T. Nicolson, J.-W. Lai, A. Natarajan, P.-Y. Chen, S. K. Reynolds, J.-H. C. Zhan, D. G. Kam, D. Liu, and B. Floyd, "A Fully Integrated 16-Element Phased-Array Transmitter in SiGe BiCMOS for 60-GHz Communications," *IEEE Journal of Solid-State Circuits*, vol. 45, no. 12, pp. 2757–2773, 2010.

[19] E.-T. Sung, S. Wang, and S. Hong, "A 60-GHz Polar Vector Modulator With Lookup Table-Based Calibration," *IEEE Microwave and Wireless Components Letters*, vol. 31, no. 6, pp. 572–574, 2021.

[20] C. So, E.-T. Sung, and S. Hong, "A 60-GHz Variable Gain Phase Shifter Based on Body Floated RF-DAC Structure," *IEEE Transactions on Circuits and Systems II: Express Briefs*, vol. 69, no. 12, pp. 4749–4753, 2022.

[21] N. Wei, N. Li, M. Li, H. Gao, S. Wang, C. Song, X. Yu, and Z. Xu, "A Calibration Scheme for 24–28-GHz Variable-Gain Phase Shifter in 65-nm CMOS," *IEEE Transactions on Circuits and Systems II: Express Briefs*, vol. 69, no. 4, pp. 1996–2000, 2022.

[22] S. Wang, J. Park, and S. Hong, "A K-Band Variable-Gain Phase Shifter Based on Gilbert-Cell Vector Synthesizer With RC–RL Poly-Phase Filter," *IEEE Microwave and Wireless Components Letters*, vol. 31, no. 4, pp. 393–396, 2021.

[23] H. Aumann, A. Fenn, and F. Willwerth, "Phased array antenna calibration and pattern prediction using mutual coupling measurements," *IEEE Transactions on Antennas and Propagation*, vol. 37, no. 7, pp. 844–850, 1989.

[24] A. Nafe, A. H. Aljuhani, K. Kibaroglu, M. Sayginer, and G. M. Rebeiz, "In-Situ Self-Test and Self-Calibration of Dual-Polarized 5G TRX Phased Arrays Leveraging Orthogonal-Polarization Antenna Couplings," in *IEEE/MTT-S International Microwave Symposium (IMS)*, 2020, pp. 1081–1084.

[25] H.-J. Yoon and B.-W. Min, "Improved Rotating-Element Electric-Field Vector Method for Fast Far-Field Phased Array Calibration," *IEEE Transactions on Antennas and Propagation*, vol. 69, no. 11, pp. 8021–8026, 2021.

[26] M. Liu and Z. Feng, "Combined Rotating-element Electric-field Vector (CREV) Method for nearfield Calibration of Phased Array Antenna," in *International Conference on Microwave and Millimeter Wave Technology*, 2007, pp. 1–4.

[27] S. Silverstein, "Application of orthogonal codes to the calibration of active phased array antennas for communication satellites," *IEEE Transactions on Signal Processing*, vol. 45, no. 1, pp. 206–218, 1997.

[28] E. Lier, M. Zemlyansky, D. Purdy, and D. Farina, "Phased array calibration and characterization based on orthogonal coding: Theory and experimental validation," in *IEEE International Symposium on Phased Array Systems and Technology*, 2010, pp. 271–278.

[29] Z. Wang, F. Zhang, H. Gao, O. Franek, G. F. Pedersen, and W. Fan, "Over-the-Air Array Calibration of mmWave Phased Array in Beam-Steering Mode Based on Measured Complex Signals," *IEEE Transactions on Antennas and Propagation*, vol. 69, no. 11, pp. 7876–7888, 2021.

[30] R. Long, J. Ouyang, F. Yang, W. Han, and L. Zhou, "Multi-Element Phased Array Calibration Method by Solving Linear Equations," *IEEE Transactions on Antennas and Propagation*, vol. 65, no. 6, pp. 2931–2939, 2017.

[31] S. Tang, Z. Wang, C. Pan, R. Su, W. Fan, and S. Gao, "A Fast and Efficient Calibration Method for Phased Array Antennas Using Fourier-Structured Excitation Matrix," *IEEE Transactions on Antennas and Propagation*, vol. 71, no. 3, pp. 2290–2299, 2023.

[32] Y. Aslan, P. Aubry, N. B. Onat, J. Janssen, M. Geurts, and A. Yarovoy, "Heuristic Over-the-Air Calibration of Beamformer ICs in Active mm-Wave Phased Arrays," in *IEEE Conference on Antenna Measurements and Applications (CAMA)*, 2023, pp. 840–845.

[33] R. X. F. Budé, K. A. P. Van Hastenberg, U. Johannsen, and A. B. Smolders, "Near-Field Calibration Methods for Integrated Analog Beamforming Arrays and Focal Plane Array Feeds," *IEEE Open Journal of Antennas and Propagation*, vol. 4, pp. 860–870, 2023.

[34] M. H. Sahlabadi, H. Yu, J. Xia, and S. Boumaiza, "A Digitally-Controlled Bidirectional 24-32 GHz Variable Gain Phase Shifter in 45 nm SOI CMOS," *IEEE Transactions on Circuits and Systems II: Express Briefs*, pp. 1–1, 2024.

[35] ——, "A Compact, High Tuning Accuracy and Enhanced Linearity 37-43 GHz Digitally-Controlled Vector Sum Phase Shifter," in *2024 IEEE 24th Topical Meeting on Silicon Monolithic Integrated Circuits in RF Systems (SiRF)*, 2024, pp. 17–20.

[36] B. Xia, W. Chen, F. M. Ghannouchi, and Z. Feng, "An 18–50-GHz – Modulated Quasi-Continuous Digital Vector-Modulation Phase Shifter With Variable Gain Control," *IEEE Microwave and Wireless Components Letters*, vol. 32, no. 1, pp. 60–63, 2022.

[37] C. Shipley and D. Woods, "Mutual coupling-based calibration of phased array antennas," in *IEEE International Conference on Phased Array Systems and Technology (Cat. No.00TH8510)*, 2000, pp. 529–532.

[38] R. Yonezawa, Y. Konishi, I. Chiba, and T. Katagi, "Beam-shape correction in deployable phased arrays," *IEEE Transactions on Antennas and Propagation*, vol. 47, no. 3, pp. 482–486, 1999.

[39] S. Choi, Y. Aoki, H.-C. Park, S.-G. Yang, and H.-J. Song, "Sequential Loopback Built-in Self-Test Algorithm for Dual-Polarization Millimeter-Wave Phased-Array Transceivers," in *IEEE Radio Frequency Integrated Circuits Symposium (RFIC)*, 2021, pp. 55–58.

[40] A. Waks, S. Bardy, O. Crand, T. Taris, and J.-B. Begueret, "Novel Built-In Test Equipment for Phase Measurement in Millimeter-Wave Phased Arrays Integrated Circuits With Absolute Phase Measurement Capabilities," *IEEE Transactions on Microwave Theory and Techniques*, vol. 70, no. 11, pp. 5234–5247, 2022.

[41] O. Inac, F. Golcuk, T. Kanar, and G. M. Rebeiz, "A 90–100-GHz Phased-Array Transmit/Receive Silicon RFIC Module With Built-In Self-Test," *IEEE Transactions on Microwave Theory and Techniques*, vol. 61, no. 10, pp. 3774–3782, 2013.

[42] T. Kanar, S. Zihir, and G. M. Rebeiz, "A 2–15-GHz Accurate Built-in-Self-Test System for Wideband Phased Arrays Using Self-Correcting Eight-State I/Q Mixers," *IEEE Transactions on Microwave Theory and Techniques*, vol. 64, no. 12, pp. 4250–4261, 2016.

[43] B. Cetindogan, E. Ozeren, B. Ustundag, M. Kaynak, and Y. Gurbuz, "A 6 Bit Vector-Sum Phase Shifter With a Decoder Based Control Circuit for X-Band Phased-Arrays," *IEEE Microwave and Wireless Components Letters*, vol. 26, no. 1, pp. 64–66, 2016.

[44] T. Wu, Y. Wu, X. Zhang, Z. Xing, C. Zhao, H. Liu, Y. Yu, and K. Kang, "A 60-GHz Variable Gain Phase Shifter With 14.8-dB Gain Tuning Range and 6-Bit Phase Resolution Across 25 °C–110 °C," *IEEE Transactions on Microwave Theory and Techniques*, vol. 69, no. 4, pp. 2371–2385, 2021.

[45] N. Li, M. Li, S. Wang, Z. Zhang, H. Gao, Y.-C. Kuan, C. Song, X. Yu, Q. J. Gu, and Z. Xu, "A Four-Element 7.5–9-GHz Phased-Array Receiver With 1–8 Simultaneously Reconfigurable Beams in 65-nm CMOS," *IEEE Transactions on Microwave Theory and Techniques*, vol. 69, no. 1, pp. 1114–1126, 2021.

[46] J. Park, G. Jeong, and S. Hong, "A Ka-Band Variable-Gain Phase Shifter With Multiple Vector Generators," *IEEE Transactions on Circuits and Systems II: Express Briefs*, vol. 68, no. 6, pp. 1798–1802, 2021.

[47] H. Gao, W. Wang, Y. Wu, Y. Liu, G. F. Pedersen, and W. Fan, "Experimental Comparison of On–Off and All-On Calibration Modes for Beam-Steering Performance of mmWave Phased Array Antenna-in-Package," *IEEE Transactions on Instrumentation and Measurement*, vol. 70, pp. 1–9, 2021.

[48] I. Kalyoncu, E. Ozeren, A. Burak, O. Ceylan, and Y. Gurbuz, "A Phase-Calibration Method for Vector-Sum Phase Shifters Using a Self-Generated LUT," *IEEE Transactions on Circuits and Systems I: Regular Papers*, vol. 66, no. 4, pp. 1632–1642, 2019.

[49] Y. Chen and S. Boumaiza, "Rapid Calibration of Variable Gain Phase Shifters: A Novel Characterization Approach with Sparse Measurements," in *IEEE/MTT-S International Microwave Symposium*, 2024.